Discriminating Mental States by Extracting Relevant Spatial Patterns under Non-Stationary and Subject-Independent Constraints

Luisa Fernanda Velásquez Martínez

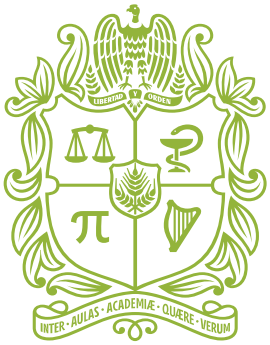

Universidad Nacional de Colombia
Facultad de Ingeniería y Arquitectura
Departamento de Ingeniería Eléctrica, Electrónica y Computación
Manizales
2023

Discriminating Mental States by Extracting Relevant Spatial Patterns under Non-Stationary and Subject-Independent Constraints

Luisa Fernanda Velásquez Martínez

Thesis for the degree of
Ph. D. in Engineering — Automatics

Advisor
Prof. César Germán Castellanos Domínguez

Universidad Nacional de Colombia
Facultad de Ingeniería y Arquitectura
Departamento de Ingeniería Eléctrica, Electrónica y Computación
Manizales
2023

Discriminación de estados mentales mediante la extracción de patrones espaciales bajo restricciones de no estacionariedad e independencia de sujeto

Luisa Fernanda Velásquez Martínez

Tesis para optar al título de
Ph. D. en Ingeniería — Automática

Director
Prof. César Germán Castellanos Domínguez

Universidad Nacional de Colombia
Facultad de Ingeniería y Arquitectura
Departamento de Ingeniería Eléctrica, Electrónica y Computación
Manizales
2023

Contents

List of Tables

List of Figures

Acknowledgments

Thanks God for all these things that You have helped me to achieve!.

I would like to thank my supervisor Cesar Germán Castellanos Domínguez, for his invaluable contributions to this thesis and his help to clarify and discuss several findings of this work.

Also, I am very thankful for the support, and advisement given by my partners at the research group *Grupo de Control y Procesamiento Digital de Señales* at Universidad Nacional de Colombia, Sede Manizales. Specially to my friends, Jorge, Anderson, Diego and Frank were always on my side to encourage and discuss academic ideas about the project helping me to resolve a lot of doubts about my research.

I would also like to thank my mother for her support throughout my entire life. A special thank goes out to my friends Maria Teresa and Laura; they always gave me their full support and confidence to keep going pursuing my dreams.

I recognize that this research would not have been possible without the financial assistance provided by Ph.D. Scholarship *Convocatoria Doctorados Nacionales* 727, funded by MINCIENCIAS.

Luisa Fernanda Velásquez Martínez
December, 2022

Abstract

Evaluation of brain dynamics elicited by motor imagery (MI) tasks can contribute to clinical and learning applications. In this work, we propose four specific improvements for brain motor intention response analysis based on EEG recordings by considering the nonstationarity, nonlinearity of brain signals, inter- and intra-subject variability, aimed to provide physiological interpretability and the distintiveness between subjects neural response. Firstly, to build up the subject-level feature framework, a common representational space, is proposed that encodes the electrode (spatial) contribution, evolving through time and frequency domains. Three feature extraction methods were compared, providing insight into the possible limitations. Secondly, we present an Entropy-based method, termed *VQEnt*, for estimation of ERD/S using quantized stochastic patterns as a symbolic space, aiming to improve their discriminability and physiological interpretability. The proposed method builds the probabilistic priors by assessing the Gaussian similarity between the input measured data and their reduced vector-quantized representation. The validating results of a bi-class imagine task database (left and right hand) prove that *VQEnt* holds symbols that encode several neighboring samples, providing similar or even better accuracy than the other baseline sample-based algorithms of Entropy estimation. Besides, the performed ERD/S time-series are close enough to the trajectories extracted by the variational percentage of EEG signal power and fulfill the physiological MI paradigm. In BCI literate individuals, the *VQEnt* estimator presents the most accurate outcomes at a lower amount of electrodes placed in the sensorimotor cortex so that reduced channel set directly involved with the MI paradigm is enough to discriminate between tasks, providing an accuracy similar to the performed by the whole electrode set. Thirdly, multi-subject analysis is to make inferences on the group/population level about the properties of MI brain activity. However, intrinsic neurophysiological variability of neural dynamics poses a challenge for devising efficient MI systems. Here, we develop a *time-frequency* model for estimating the spatial relevance of common neural activity across subjects employing an introduced statistical thresholding rule. In deriving multi-subject spatial maps, we present a comparative analysis of three feature extraction methods: *Common Spatial Patterns*, *Functional Connectivity*, and *Event-Related De/Synchronization*. In terms of interpretability, we evaluate the effectiveness in gathering MI data from collective populations by introducing two assumptions: *i*) Non-linear assessment of the similarity between multi-subject data originating the subject-level dynamics; *ii*) Assessment of time-varying brain network responses according to the ranking of individual accuracy performed in distinguishing distinct motor imagery tasks (left-hand versus right-hand). The obtained validation results indicate that the estimated collective dynamics differently reflect the

flow of sensorimotor cortex activation, providing new insights into the evolution of MI responses. Lastly, we develop a data-driven estimator, termed Deep Regression Network (DRN), which jointly extracts and performs the regression analysis in order to assess the efficiency of the individual brain networks in practicing MI tasks. The proposed double-stage estimator initially learns a pool of deep patterns, extracted from the input data, in order to feed a neural regression model, allowing for infering the distinctiveness between subject assemblies having similar variability. The results, which were obtained on real-world MI data, prove that the DRN estimator fosters pre-training neural desynchronization and initial training synchronization to predict the bi-class accuracy response, thus providing a better understanding of the Brain–Computer Interface inefficiency of subjects.

Keywords:

motor imagery, entropy, sensorimotor rhythm, event-related de/synchronization, brain-computer interface, regression networks, multi-subject analysis.

Resumen

La evaluación de la dinámica cerebral provocada por las tareas de imaginación motora (*Motor Imagery - MI*) puede contribuir al desarrollo de aplicaciones clínicas y de aprendizaje. En este trabajo, se proponen cuatro mejoras específicas para el análisis de la respuesta de la intención motora cerebral basada en registros de Electroencefalografía (EEG) al considerar la no estacionariedad, la no linealidad de las señales cerebrales y la variabilidad inter e intrasujeto, con el objetivo de proporcionar interpretabilidad fisiológica y la discriminación entre la respuesta neuronal de los sujetos. En primer lugar, para construir el marco de características a nivel de sujeto, se propone un espacio de representación común que codifica la contribución del electrodo (espacial) y como esta evoluciona a través de los dominios de tiempo y frecuencia. Tres métodos de extracción de características fueron comparados, proporcionando información sobre las posibles limitaciones. En segundo lugar, se presenta un método basado en Entropía, denominado *VQEnt*, para la estimación de la desincronización relacionada a eventos (*Event-Related De-Synchronization - ERD/S*) utilizando patrones estocásticos cuantificados en un espacio simbólico, con el objetivo de mejorar su discriminabilidad e interpretabilidad fisiolgica. El método propuesto construye los antecedentes probabilísticos mediante la evaluación de la similitud gaussiana entre los datos medidos de entrada y su representación cuantificada vectorial reducida. Los resultados de validación en una base de datos de tareas de imaginación bi-clase (mano izquierda y mano derecha) prueban que *VQEnt* contiene símbolos que codifican varias muestras vecinas, proporcionando una precisión similar o incluso mejor que los otros algoritmos basados en estimación de entropía de referencia. Además, las series temporales de ERD/S calculadas son lo suficientemente cercanas a las trayectorias extraídas por el porcentaje de variación de la potencia de la señal EEG y cumplen con el paradigma fisiológico de MI. En individuos alfabetizados en BCI, el estimador *VQEnt* presenta los resultados precisos con una menor cantidad de electrodos colocados en la corteza sensoriomotora, de modo que el conjunto reducido de canales directamente involucrados con el paradigma MI es suficiente para discriminar entre tareas. En tercer lugar, el análisis multisujeto consiste en hacer inferencias a nivel de grupo/población sobre las propiedades de la actividad cerebral de la imaginación motora. Sin embargo, la variabilidad neurofisiológica intrínseca de la dinámica neuronal plantea un desafío para el diseño de sistemas MI eficientes. En este sentido, se presenta un modelo de *tiempo-frecuencia* para estimar la relevancia espacial de la actividad neuronal común entre sujetos empleando una regla de umbral estadística que deriva en mapas espaciales de múltiples sujetos. Se presenta un análisis comparativo de tres métodos de extracción de características: *Patrones espaciales comunes*, *Conectividad funcional* y *De-sincronización relacionada con eventos*. En términos de interpretabilidad,

evaluamos la efectividad en la recopilación de datos de MI para multisujetos mediante la introducción de dos suposiciones: *i*) Evaluación no lineal de la similitud entre los datos de múltiples sujetos que originan la dinámica a nivel de sujeto; *ii*) Evaluación de las respuestas de la red cerebral que varían en el tiempo de acuerdo con la clasificación de la precisión individual realizada al distinguir distintas tareas de imaginación motora (mano izquierda versus mano derecha). Los resultados de validación obtenidos indican que la dinámica colectiva estimada refleja de manera diferente el flujo de activación de la corteza sensoriomotora, lo que proporciona nuevos conocimientos sobre la evolución de las respuestas de MI. Por último, se muestra un estimador denominado Red de regresión profunda (*Deep Regression Network - DRN*), que extrae y realiza conjuntamente un análisis de regresión para evaluar la eficiencia de las redes cerebrales individuales, de cada sujeto, en la práctica de tareas de MI. El estimador de doble etapa propuesto inicialmente aprende un conjunto de patrones profundos, extraídos de los datos de entrada, para alimentar un modelo de regresión neuronal, lo que permite inferir la distinción entre conjuntos de sujetos que tienen una variabilidad similar. Los resultados, que se obtuvieron con datos MI del mundo real, demuestran que el estimador DRN usa la desincronización neuronal previa al entrenamiento y la sincronización del entrenamiento inicial para predecir la respuesta de precisión bi-clase, proporcionando así una mejor comprensión de la ineficiencia de la respuesta de MI de los sujetos en las Interfaces Cerebro-Computador.

Palabras clave

imaginación motora, entropia, ritmos sensori-motores, sincronización relacionada a eventos, interfaz cerebro-computador, redes de regresión, analisis multi-subjeto.

Chapter 1

Preliminaries

1.1 Introduction

The brain is the complex and mysterious core of who we are as human beings; its process determines our personalities, thoughts, emotions, behaviors, and body functions. So, understanding brain functions and the neural circuits involved in their operation awake researchers of multiple science disciplines as this knowledge helps to prevent and treat brain diseases and disorders. In this regard, neural signal processing methods are crucial to determine how the brain represents or encodes information about different internal/external conditions and how to extract or decode this information from the measured neural signals [2]. Those questions are relevant to researchers developing Brain-Computer Interfaces (BCI), which aim to translate the brain response to commands to external devices. The most applied BCI principally focus on the development of personal assistance systems for people with serious motor disabilities, disorders, or degenerative neuropathologies that are unable to communicate properly, impacting significantly their quality of life and ability to live independently [3,4]. Usually, BCI systems are based on a widely used cognitive neuroscience paradigm Motor Imagery (MI), which corresponds to the brain activity patterns of the imagination of a motor action without involving muscle activities. It is believed that real movements and those performed mentally (imaginary movements) are functionally similar [5].

From the neural signal processing point of view, a BCI system comprises two fundamental stages; the acquisition of neural information and the discrimination of brain activity patterns [6]. Regarding the signal acquisition stage, the neural response can be measured using invasive and noninvasive neuroimage techniques. On the one hand, in invasive neural recordings, electrodes are implanted directly into the grey matter either cortical or subcortical areas being high-fidelity neural signals recorded with a high signal-to-noise ratio (SNR) [7]. However, these techniques suffer from usability issues such as the involvement of surgical procedures, problems regarding the stability of implants, and the risk of infection. Therefore, these methods are limited to some medical research scenarios [8]. On the other hand, non-invasive neuroimaging techniques measure neural activity out of the scalp, including functional MRI (fMRI), Magnetoencephalography (MEG), and Electroencephalographic (EEG) signals [2]. Recording cognitive tasks, with process time-scales less than 100 ms, fMRI is inadequate since it provides an adequate spatial resolution but ex-

hibits insufficient time resolution caused by its dependence on blood flow. In contrast, EEG and MEG signals, having a high-temporal resolution, measure the brain activity caused by the flow of electric currents or by magnetic fields that are measurable outside of the head, respectively. Nevertheless, MEG signals could be interfered with other magnetic signals, such as the earth's magnetic field, requiring specific equipment and laboratory configuration for recording it. EEG signal is the most employed because of its easy, non-expensive, low-risk, and portable acquisition [9]. Accordingly, EEG analysis is used for studying the brain dynamics in several applications such as testing afferent pathways, game controlling, clinical diagnosis, sleep analysis, and BCI [10, 11].

EEG recording results of the complex firing pattern of billions of neurons that communicate with each other in a highly distributed, dynamic, and complex system as is the human brain [12]. As neurons tend to work in synchrony, EEG shows primary forms of activity which are the brain rhythms commonly used for different types of tasks being categorized under six frequency bands δ band $(0.5 - 4\,Hz)$, θ band $(4 - 8\,Hz)$, α band $(8 - 12\,Hz)$, μ band $(8 - 12\,Hz)$, β band $(13 - 30\,Hz)$, and γ band $(> 25\,Hz)$ [11, 13]. For MI activity analysis, both the μ and β waveforms are widelyknown as informative due to they are associated with those cortical areas directly connected to the channels of a normal motor output [14]. Also, elicited by MI activity, Event-Related De/Synchronization (ERD/S) captures temporal dynamics related to both sensory and cognitive processes. So, ERD/S is a time-locked change of ongoing EEG signals of electrodes placed in the sensorimotor area, showing an intensified cooperation between the decreasing ipsilateral and increased contralateral motor regions for movement representations.

For the second stage, the discrimination of brain activity patterns requires the designing of methodologies able to take a broad amount of neural measures to detect event-related response patterns from an overwhelming noise recording, providing the means for characterizing task-related brain states and distinguishing them from non-interesting activity [15]. Moreover, MI-BCI systems development contains two-stages, calibration and online mode. In the calibration mode, the user performs voluntary ERD/S modulations and the BCI pipeline, containining, preprocessing, feature extraction, and classification stages, learns subject dependent MI patterns extracting its temporal, spectral, and spatial characteristics. In the online mode, learned patterns are translated into a control signal to some external application or device.

Although the primary goal of a BCI system is to classify brain signals, understanding MI fundamentals gives insights into the underpinning brain dynamic organization since a mental representation of specific movements involves cooperating (sub-)cortical networks in the brain. Thus, evaluation and interpretation of brain dynamics in the sensorimotor area may contribute to the assessment of pathological conditions, the rehabilitation of motor functions [16, 17], motor learning and performance [18], evaluation of brain activity functioning in children with developmental coordination disorders [19], improving balance and mobility outcomes in older adults [20], and education scenarios [21–23], among other applications. However, the most common limitations for decoding MI neural responses are related to the inter and intra-subject variability that leads to the non-stationary, nonlinear, and poor signal-to-noise ratio of EEG signals [24].

Nevertheless, to enhance the analysis of triggering mental activity, feature representation approaches are performed to derive distinct EEG spatial maps with varying frequency

and time characteristics [25]. To begin with, Filter-Bank Common Spatial Patterns are a popular algorithm in MI systems that discriminate multichannel EEG signals by highlighting differences while minimizing similarities, selecting frequency bands appropriately [26]. Also, Functional Connectivity (FC) networks are extracted because a better understanding of MI mechanisms requires knowledge of the way the co-activated brain regions interact with each other [27]. Acordingly, the *wPLI* metric of EEG functional connectivity can account for linear brain interactions but is also expected to be sensitive to nonlinear couplings [28]. Another approach for characterizing the imaged hand movements is to quantify frequency alterations in time-varying responses to a stimulus (event) through the so-termed ERD/S, presenting a significant correlate of localized cortical oscillatory activity [29]. When imagining one hand moving, an increase/decrease in the power of μ and β rhythms becomes more potent in the sensorimotor (electrodes C3 and C4) and premotor (Cz) areas located contralaterally to the hand involved in the task [30]. Due to the non-stationarity of EEG data, however, the effectiveness of feature extraction procedures is reduced in deriving distinct EEG spatio-spectral patterns. Several factors can affect, among others, the following: movement artifacts during recording, temporal stability of mirroring activation over several sessions differs notably between MI time intervals [31,32], low EEG signal-to-noise ratio, poor performance in small-sample settings [33], and inter-subject variability in EEG dynamics [34]. Along with variability in the signal acquisition, another circumstance that leads to low accuracy scores is that some subjects may have brain networks, not sufficiently developed for practicing MI tasks [35]. As a result, the performance of MI systems varies considerably across and within-subjects, severely degrading their reliability. Also, between 15% to 30% of users may not develop enough MI coordination skills, which defines BCI illiteracy, subjects with BCI performance lower than 70%, posing one of the biggest challenges in MI research [36–38].

In detail, ERD/S is computed to capture channel-wise temporal dynamics related to both sensory and cognitive processes. So, ERD/S is a time-locked change of ongoing EEG signals of electrodes placed in the sensorimotor area, showing an intensified cooperation between the decreasing ipsilateral and increased contralateral motor regions for movement representations. Conventionally, ERD/S is estimated by the instantaneous amplitude power that is normalized to a reference-time level and averaged over a representative amount of EEG trails in an attempt to improve the signal-to-noise ratio [39]. For decreasing the inherent inter-subject variability, the scatters of trial power must be accurately reduced, usually by a trial-and-error procedure, hindering the detection and classification of motor-related patterns in single-trial training. Correcting the baseline of each single-trial before averaging spectral estimates is an alternative method [40]. Nonetheless, the ERD/S patterns are characterized by its fairly localized topography and frequency specificity, making this approach include a priori choice of frequency bands. However, the band-passed oscillatory responses tend to depreciate a wide range of nonlinear and non-stationary dynamics, which may be interacting in response to a given stimulus by synchronization of oscillatory activities [41].

As a consequence of the nonstationarity and nonlinearity of acquired EEG data [42], the MI brain activity shows considerable variations in complexity of the physiological system with dynamics affected by motor tasks that can be perceived in the pre-stimulus activity and the elicited responses. Thus, the extracted ERS/D time-courses can be modeled as

the output of a nonlinear system. In this regard, various measures are reported to quantify the complex dynamics of elicited brain activity, like Kolmogorov complexity [43], Permutation Entropy, Sample Entropy, and its derived modification termed Fuzzy Entropy [44] that provides a fuzzy boundary for similarity measurements [45], or even the fusion of Entropy estimators to achieve the complementarity among different features, as developed in [46]. However, extraction of ERD/S dynamics using Entropy-based pattern estimation is hampered by several factors like movement artifacts during recording, temporal stability of mirroring activation over several sessions differs notably between MI time intervals [32], low EEG signal-to-noise ratio, poor performance in small-sample setting [33], and inter-subject variability in EEG patterns [34]. Hence, the reliability of Entropy-based estimators may be limited by several factors like lacking continuity, robustness to noise, and biasing derived from superimposed trends in signals.

One approach to yield more statistical stability from Sample-based estimators is to transform the time series into a symbolic space, from which the regularity of MI activity is measured like in the case of Permutation Entropy that associates each time series with a probability distribution, whose elements are the frequencies connected with feasible permutation patterns, and being computationally fast [47]. Since the irregularity indicator considers only the order of amplitude values, several variations to the initially developed permutation Entropy are proposed to tackle the problem of information discarding. Thus, Dispersion Entropy appraises the frequency of a symbolic space that is built in mapping each sample through a class pattern set across epochs [48], retaining higher sensitivity to amplitude differences and accepting adjacent instances of the same class [49]. Further improvements can be achieved by introducing information about amplitudes and distances [50, 51]. Besides entering more free parameters to tune, the sample-based estimators face additional restrictions in the extraction of ERD/S dynamics like the fact that motor imagery activity reduces the EEG signal complexity [52]. Also, there is a need for a careful choice of the time window that mostly affects the effectiveness of short-time feature extraction procedures; it must have enough length to cover the interval within a neural pattern is activated, while at the same time it should remove the unrelated sampling points [53].

To compensate for the intra-subject variability of EEG dynamics, novel approaches are being developed to integrate information across subjects within a collective framework, combining individual feature sets of neural dynamics to improve the brain representation robustness, as explained in [54]. Thus, under the assumption that temporal signatures from an evoked neural activity are similar across subjects, group models can be extracted for decoding the multi-subject mental responses to complex stimuli without explicitly representing the elicitation [55]. Several strategies for raw data aggregation can be implemented for building group inferences, including serial/parallel combinations of subject-level feature sets to form a more extensive multi-subject array [56]. Instead, data-driven approaches have also been employed to infer collective feature structures, like joint diagonalization [57], temporally constrained sparse representation [58], canonical correlation analysis [59], and versions derived from independent Component Analysis [60–62], among others.

For interpretation purposes, the topographic representation is commonly computed to display the spatial distribution of the extracted common neural patterns. Nonetheless,

the building of multi-subject models implies the accurate aggregation of time-frequency patterns extracted from EEG dynamics across the subjects by adequately selecting the domain parameters (i.e., time window length and filter bandwidth setup) [63]. Moreover, the aggregation can face a different dimensionality derived from the feature extraction methods involved. Due to the difference in captured dynamics, each engaged extraction method differently reflects the flow of sensorimotor, being one of the issues that arise in identifying group relationships confidently [64]. Besides, to evaluate computational network models, there is a need to establish the meaning of the aggregation of extracted brain-activity patterns [65]. Hence, another issue to consider is to assess the ability of multi-subject sets to preserve the main properties (i.e., the spatial distribution of brain neural activity throughout time and spectral domains) extracted from single-subject models.

One more enhancing strategy of learning is identifying the causes of variability and incorporating appropriate actions in order to compensate for the BCI inefficiency [66], for instance, by including a calibration module that works hand-in-hand with the training procedure to make learning algorithms adapt to user EEG patterns [67, 68]. In this regard, the correlation between the neural activity features that are extracted in advance (electrophysiological indicators or predictor) with the MI onset responses instructed via sensory stimuli can be assessed to prescreen participants for the ability to learn regulation of brain activity (pre-training measures) or for the improvement of learning abilities (training phase) [69]. A systematic review of the predictors of neurofeedback training outcome is given in [70, 71], concluding that the most promising predictor seems to be the (neurophysiological) baseline activity, which was derived from the parameter targeted by the training. In an attempt to anticipate the evoked MI responses, several pre-training electrophysiological indicators are reported, like functional connectivity of resting-state networks [72], α rhythm activity of eyes-open and eyes-closed resting-states [73], pre-cue EEG rhythms over different brain regions [74], and the power spectral density estimates of resting wakefulness (before the cue-onset of the conventional MI trial timing and resting state) [75, 76]. Although this last predictor is one of the most used, its curve-fitting method depends heavily on various parameters that are difficult to determine, regardless of the resting data employed [77]. Other predictors are derived from measuring the change in electrophysiological properties across the training sessions [78–80]. Thus, ERD/S is extracted in order to evaluate the (in)efficiency of MI training, which shows a distinct activation of the sensorimotor cortex region in response to imagery tasks [81]. Although visible ERD lateralization of evoked MI activity has been considered for predicting the user's control ability from neurophysiological measures [82], the characterization of its topography and frequency specificity poses a challenging task because of the difficulty in accurately quantifying the trial-to-trial variability [43, 83].

The linear correlation and regression models are used to explore or test the relationship between predictor and outcome measures, since they provide direct insight into the possible reasons for BCI control failures. However, the assumption of proportionality may be strong enough in real settings of MI tasks, resulting in scores with low values of significance. Instead, this task can be solved using linearizing models (like logistic regression [84]), which vary depending on the types and numbers of EEG indicators selected in each model [85]. Thus, related to motor evoked potential time series, nonlinear models (like random forests) can achieve significantly better prediction performance than a linear

one (or logistic regression) [86]. In particular, machine learning analysis in nonlinear regression is extensively employed under two deep learning solutions [87,88]: *i*) utilizing an ensemble of deep networks that suffer from larger computational complexity and *ii*) transforming a single nonlinear regression hypothesis to a robust loss function that is jointly optimizable with the deep network usually in terms of the mean square error. However, the generalization ability is a major concern in developing deep regression models and computational complexity and hardware consumption [89].

For all these reasons, in this work, we propose four specific improvements for brain motor intention response analysis based on EEG recordings by considering the nonstationarity, nonlinearity of brain signals, inter- and intra-subject variability, aimed to provide physiological interpretability and the distintiveness between subjects neural response.

Firstly, to build up the subject-level feature framework, a common representational space, is proposed that encodes the electrode (spatial) contribution, evolving through time and frequency domains. Three feature extraction methods were compared, providing insight into the possible limitations. To address sources of inter-subject and inter-trial variability of individuals, we extracted a feature set, for which the domain parameters (time window length and filter bandwidth setup) are selected to be the more relevant in discriminating between MI tasks, yielding a distinct dimensionality of each extracted characteristic set.

Second, considering the nonstationarity and nonlinearity of EEG signals, we proposed a feature extraction methodology based on Entropy for estimation of ERD/S using quantized stochastic patterns as a symbolic space, aiming to improve their discriminability and physiological interpretability. The proposed method builds the probabilistic priors by assessing the Gaussian similarity between the input measured data and their reduced vector-quantized representation. The performed ERD/S time-series are close enough to the trajectories extracted by the variational percentage of EEG signal power and fulfill the physiological MI paradigm. Also, the proposed estimator presents the most accurate outcomes at a lower amount of electrodes placed in the sensorimotor cortex for the inter-subjects variability.

Thirdly, we developed a methodology for building a time-frequency model for estimating the spatial relevance of common activity employing an introduced statistical thresholding rule. Additionally, we present a comparative analysis of three feature extraction methods: Common Spatial Patterns, Functional Connectivity, and Event-Related De/Synchronization. In terms of interpretability, we evaluated the effectiveness in gathering MI data from collective populations by introducing two assumptions: *i*) Non-linear assessment of the similarity between multi-subject data producing the subject-level dynamics; *ii*) Assessment of time-varying brain network responses according to the ranking of individual accuracy performed in distinguishing distinct motor imagery tasks (left-hand versus right-hand).

Lastly, we developed a data-driven estimator, which jointly extracts and performs the regression analysis to assess the efficiency of the individual brain networks in practicing MI tasks considering the inter- and intra-subject variability. The proposed estimator allows for inferring the distinctiveness between subject assemblies having similar variability.

1.2 General Objective

To develop a methodology for brain motor intention response analysis based on EEG recordings by considering the nonstationarity, nonlinearity of brain signals, and inter- and intra-subjects variability, aimed to provide physiological interpretability and the distinctiveness between subjects neural response.

1.3 Specific Objectives

- To develop a feature representation framework to decode brain evolution dynamics and motor imagery inter-subject variability preserving physiological interpretability.
- To propose a feature extraction method to estimate motor imagery response, that considers the non-stationarity and non-linearity of brain time-series, aiming to improve discriminability and physiological interpretability.
- To suggest a multi-subject feature representation methodology to capture intra-subject features, which are considered as prevalent in the group, preserving physiological interpretability.
- To propose an estimator to assess the individual brain networks efficiency in practicing MI task, deling with inter- and intra-subject variability allowing to infer the distinctiveness between subject assemblies.

1.4 Academic Discussion

Velasquez-Martinez, Luisa, Caicedo-Acosta, Julian; Alvarez-Meza Andres, Castellanos-Dominguez, German. "Regression Networks for Neurophysiological Indicator Evaluation in Practicing Motor Imagery Tasks". *Brain Sciences*, 2020, vol. 10, no 10, p. 707.

Velasquez-Martinez, Luisa; Caicedo-Acosta, Julian; Castellanos-Dominguez, German. Entropy-Based Estimation of Event-Related De/Synchronization in Motor Imagery Using Vector-Quantized Patterns". *Entropy*, 2020, vol. 22, no 6, p. 703.

Velasquez-Martinez, Luisa F.; Zapata-Castano, Frank; Castellanos-Dominguez, German. "Dynamic Modeling of Common Brain Neural Activity in Motor Imagery Tasks". *Frontiers in Neuroscience*, 2020, vol. 14.

Velasquez-Martinez, Luisa F.; Arteaga, F.; Castellanos-Dominguez, German. "Subject-Oriented Dynamic Characterization of Motor Imagery Tasks Using Complexity Analysis". *International Conference on Brain Informatics*. Springer, Cham, 2019. p. 21-28.

Velasquez-Martinez, Luisa F., et al. "Relevance of common spatial patterns ranked by kernel PCA in motor imagery classification". *International Conference on Brain Informatics*. Springer, Cham, 2019. p. 13-20.

Velasquez-Martinez, Luisa F., et al. Group differences in time-frequency relevant patterns for user-independent BCI applications". *International Work-Conference on the Interplay Between Natural and Artificial Computation*. Springer, Cham, 2019. p. 138-145.

Velasquez-Martinez, Luisa F., et al. "Detecting EEG dynamic changes using supervised temporal patterns". *International Workshop on Artificial Intelligence and Pattern Recognition*. Springer, Cham, 2018. p. 351-358.

Caicedo-Acosta, Julian, Velasquez-Martinez, Luisa F. et al. "Multiple instance learning selecting time-frequency features for Brain Computing Interfaces". *International Workshop on Artificial Intelligence and Pattern Recognition*. Springer, Cham, 2018. p. 326-333.

Velasquez-Martinez, Luisa F.; Alvarez-Meza, A.; Castellanos-Dominguez, German. "Detection of EEG Dynamic Changes Due to Stimulus-Related Activity in Motor Imagery Recordings". *International Work-Conference on the Interplay Between Natural and Artificial Computation*. Springer, Cham, 2017. p. 435-443.

Chapter 2

Materials and Methods

2.1 Subject-Level Extraction of Motor Imagery *t-f* Feature Dynamics

Using a sliding window approach, the short-time feature set is extracted from multiple frequency bands to build the labeled subject-level model of feature dynamics.

2.1.1 Estimation of Common Spatial Patterns

Given a filter-band-passed n-trial EEG recording matrix $\boldsymbol{X}^{\lambda}_{nf\tau}\in\mathbb{R}^{C\times T}$, $n\in N_{\lambda}$, $f\in N_f$, CSP finds within the time-windowed partition $\tau\in N_{\tau}$ the linear transformation vector $\boldsymbol{w}_{f\tau}\in\mathbb{R}^{C}$ that maximizes the Rayleigh Quotient (RQ) between both labels $\lambda=[l,l']$, defined as follows [90]:

$$\max_{\forall \boldsymbol{w}_{f\tau}} J = \frac{\boldsymbol{w}^{\top}_{f\tau}\boldsymbol{\Sigma}^{l}_{f\tau}\boldsymbol{w}_{f\tau}}{\boldsymbol{w}^{\top}_{f\tau}\boldsymbol{\Sigma}^{l}_{f\tau}+\boldsymbol{\Sigma}^{l'}_{f\tau}\boldsymbol{w}_{f\tau}}, \quad \text{s.t.: } \|\boldsymbol{w}\|_2 = 1 \tag{2.1}$$

where the matrix $\boldsymbol{\Sigma}^{\lambda}_{f\tau}=\mathbb{E}\left\{\boldsymbol{X}^{\lambda}_{nf\tau}\boldsymbol{X}^{\lambda\top}_{nf\tau}:\forall n\in N_{\lambda}\right\}$ is the simplest estimate of the class data variance, computed at a frequency f and sliding window τ. The notations $\|\cdot\|_p$ and $\mathbb{E}\{\cdot:\forall n\}$ stand for ℓ_p-norm and expectation operator across a variable n, respectively. Then, the sampled data $\boldsymbol{X}^{\lambda}_{nf\tau}$ is filtered through the learned spatial matrix $\boldsymbol{W}_{f\tau}\in\mathbb{R}^{\hat{K}\times C}$, holding $\hat{K}\leq C$ transformation components. Further, the projected data $\boldsymbol{Z}^{\lambda}_{nf\tau}=\boldsymbol{W}_{f\tau}\boldsymbol{X}^{\lambda}_{nf\tau}$ are obtained using only $\hat{K}=2k$ representative terms (namely, k first and k last rows), from which the feature vector $\boldsymbol{d}_{nf\tau}\in\mathbb{R}^{2k}$ is then extracted as below [91]:

$$\boldsymbol{d}_{nf\tau} = \log\left(diag(var\{\boldsymbol{Z}^{\lambda}_{nf\tau}\})\right), \quad \boldsymbol{d}_{nf\tau}\subset\boldsymbol{D}\in\mathbb{R}^{(N_l+N_{l'})\times G} \tag{2.2}$$

where $var\{\cdot\}$ denotes the variance operator. Note that the obtained feature matrix $\boldsymbol{D}=[\boldsymbol{d}_{nf\tau}:n\in N_{\lambda}]$ holds $G=N_f\times N_{\tau}\times 2k$ concatenated features, which are extracted from each MI recording trial.

Relying upon the inverse transformation matrix $\boldsymbol{W}^{-}_{f\tau}$, ultimately, we model the CSP-based dynamics of the spatial *t-f* patterns of brain activation, which are computed as below:

$$\boldsymbol{\theta}_J(f,\tau) = vec\{\boldsymbol{W}^{-}_{f\tau}\}^{\top} \tag{2.3}$$

where the vector $\boldsymbol{\theta}_J(f,\tau)\in\mathbb{R}^C$ gathers the t-f contribution from c-th EEG channel in terms of distinguishing between both labels, being learned over the whole trial set and calculated by the highest variance value (i.e., $\hat{K}=1$).

2.1.2 Computation of Functional Connectivity of Brain Networks

To investigate the pairwise inter-channel relationship, we use the *weighted Phase Locking Index* (*wPLI*) as an FC metric that quantifies the asymmetry of the phase difference distribution between two specific channels c, c' (with $\forall c, c'\in C, c\neq c'$), being each one estimated across the trial set, $\forall n\in N_\lambda$, as follows [92]:

$$\phi_{cc'}(f,\tau|\lambda)=\frac{\left|\mathbb{E}\left\{|\Delta\Phi^{(n)}_{cc'}(f,\tau;c,c'|\lambda)|\,\mathrm{sgn}\left(\Delta\Phi^{(n)}_{cc'}(f,\tau;c,c'|\lambda)\right):\forall n\right\}\right|}{\mathbb{E}\left\{|\Delta\Phi^{(n)}_{cc'}(f,\tau;c,c'|\lambda)|:\forall n\right\}},\tag{2.4}$$

where notation sgn stands for *sign* function and $\Delta\Phi^{(n)}_{c,c'}(;|)\in\mathbb{R}[0,\pi]$ is the instantaneous phase difference computed through the continuous wavelet transform coefficients $\mathcal{W}^{(n)}_{cc'}(f,\tau;c,c'|\lambda)\in\mathbb{R}^+$ by the ratio $\Delta\Phi^{(n)}_{cc'}(;|)=\mathcal{W}^{(n)}_{c}(;|)\mathcal{W}^{(n)}_{c'}(;|)/|\mathcal{W}^{(n)}_{c}(;|)||\mathcal{W}^{(n)}_{c'}(;|)|$.

The *wPLI* metric, $\phi_{cc'}(f,\tau|\lambda)\in\mathbb{R}^v$, is normalized to highlight the connectivity patterns generated by each evoked task, being each mean-value averaged over the trial set within a given baseline interval ΔT_0. Thus, we obtain the inter-channel connectivity vector through the following marginal across the node set: $\hat{\boldsymbol{\phi}}(f,\tau|\lambda)=\sum_{v\in V}\phi(f,\tau;v|\lambda)$ and the pairwise variable $v\in\{c,c'\in V, c\neq c'\}$, where $V=C(C\text{-}1)/2$ is the number of considered paired links. Therefore, we model the dynamics extracted from $\hat{\boldsymbol{\phi}}(,|)\in\mathbb{R}^C$ according to the following rule:

$$\boldsymbol{\theta}_{\hat{\phi}}(f,\tau|\lambda)=[\hat{\phi}(f,\tau;c|\lambda):c\in C]\tag{2.5}$$

2.1.3 Assessment of Event-Related De/Synchronization

This time-locked change of ongoing EEG is a somatotopical organized control mechanism that can be generated intentionally by mental imagery and has specific frequency-band interpretation. Using each c-th measured EEG recording $\boldsymbol{x}^\lambda_{nf}(c)$, the ERD/S estimation is performed, at a frequency band f and sample τ, by squaring of samples and averaging over EEG trials to compute the variational percentage (decrease or increase) in the EEG signal power regarding a reference interval as follows [93, 94]:

$$\zeta(f,\tau;c|\lambda)=\frac{(\xi(f,\tau;c|\lambda)-\bar{\xi}(f;c|\lambda))}{\bar{\xi}(f;c|\lambda)}\tag{2.6}$$

where $\xi(f,\tau;c|\lambda)=\mathbb{E}\left\{|x^\lambda_\tau(c)|^2_{nf}\in\boldsymbol{x}^\lambda_{nf}(c):\forall n\right\}$ is the power scatter averaged across the trial set and $\bar{\xi}(f;c|\lambda)=\mathbb{E}\left\{\xi(f,\tau;c|\lambda):\forall\tau\in\Delta T_0\right\}$, with $\bar{\xi}(f;c|\lambda)\in\mathbb{R}$, is the trial power scatter averaged over the reference time interval $\tau_0\subset T$, being $T\in\mathbb{R}^+$ the recording time span.

Given a label λ, therefore, we represent its corresponding ERD/S-based dynamics by computing the functional in Eq. (2.6) across all channels, that is:

$$\boldsymbol{\theta}_\zeta(f,\tau|\lambda)=[\zeta(f,\tau;c|\lambda)\in\mathbb{R}:\forall c\in C],\quad \boldsymbol{\theta}_\zeta(;|)\in\mathbb{R}^C\tag{2.7}$$

As a result, we estimate the subject-level model of *t-f* feature dynamics $\{\boldsymbol{\theta}_{\vartheta}^{(s)}(f,\tau|\lambda)$: $\forall f,\forall f\tau\}$ extracted by each method (noted by $\vartheta{=}\{J,\zeta,\phi\}$) for s-th individual. The model contains the electrode set contribution, $\boldsymbol{\theta}_{\vartheta}^{(s)}(,|){\in}\mathbb{R}^{C}[0,1]$, estimated at frequency f, time τ, and given a label λ (besides the CSP-based spatial filtering that resumes in a single model the joint influence of both labels).

2.1.4 A New Proposal for Complexity-Based Estimation of Event-Related De/Synchronization

This time-locked change of ongoing EEG is a control-mechanism of the somatotopically organized areas of the primary motor cortex, which can be generated intentionally by mental imagery. For each measured EEG recording $\boldsymbol{x}_n{\in}[x_{\Delta t,n}{\in}\mathbb{R}]$, the estimation of ERD/S is performed, at specific and sample $\Delta t{\in}T$, by squaring of samples and averaging over the EEG trial set to compute the variational percentage (decrease or increase) in EEG signal power regarding a reference interval (see Eq. (2.6)):

Instead of using the power-based estimates in Eq. (2.6) that are assessed across the trial set, the ERD/S time series can be computed in a one-trial version, for instance, by measuring the Entropy of time-series changes over time as below:

$$\zeta_{\Delta t}^{H}=\mathbb{E}\left\{\mathbb{H}\left\{X_n(\tau)\right\}:\tau{\in}T\right\},\ \tau>\Delta t \tag{2.8a}$$

$$\text{s.t.: }\left|\partial\mathbb{H}\left\{X_n(\tau)\right\}/\partial\tau\right|\text{ exists for every }\tau{\subset}T \tag{2.8b}$$

where $X_n(\cdot)$ are the state-space partition sets that can be extracted within a time window lasting $\tau{=}N_\tau\Delta t$. In terms of the Entropy metric $\mathbb{H}\{\cdot\}$, the newly-introduced restriction Eq. (2.8b) relies upon the assumption that several samples might be compared to itself when two consecutive time windows commonly consist of the same samples. So, the discrete-time space-state models can be built in the form of a following embedded representation:

$$X_n(\tau,M)=\{\tilde{\boldsymbol{x}}_n(\tau,M;q){=}[x_{m\Delta t,n}(\tau;q){:}m{\in}[q,q+M-1]]{:}q{\in}Q\},\ Q=N_\tau-M \tag{2.9}$$

where M is the embedding dimension, Q is the size of the state-space or alphabet, and $\{\tilde{\boldsymbol{x}}_n(\cdot,\cdot;q){\in}\mathbb{R}^M\}$ is the windowed representation or symbol.

Thus, the Entropy in Eq. (2.8a) can be estimated at a time window τ by a pairwise comparison between a couple of embedded versions $\pi_n(\cdot,\rho;\tau)$:

$$\mathbb{H}\left\{X_n(\tau,M);\rho\right\}=-\ln\left(\pi_n(M+1,\rho;\tau)/\pi_n(M,\rho;\tau)\right) \tag{2.10}$$

Relying on the fact that $\pi(\cdot,\cdot;\cdot)$ is the probability that two sequences are similar within M points, a direct calculation is through the mean value of pattern count that is evaluated as:

$$\pi_n(M,\rho;\tau)=\mathbb{E}\left\{\text{num}\{d\left(\tilde{\boldsymbol{x}}_n(\tau,M;q),\tilde{\boldsymbol{x}}_n(\tau,M;q')\right){<}\rho\}{:}\forall q,q'\in Q,q\neq q'\right\} \tag{2.11}$$

where $\text{num}\{d(\cdot,\cdot)\}{\in}\mathbb{N}$ is the count of distance lower than tolerance $\rho{\in}\mathbb{R}^+$, $d(\cdot,\cdot){\in}\mathbb{R}^+$ is the distance between a couple of embedded partitions. So, two widely-known distances

are used [95]:

$$\textit{SampEnt}: \quad d_S(\tilde{\boldsymbol{x}}_n(\tau, M; q), \tilde{\boldsymbol{x}}_n(\tau, M; q')) = \max_{\forall m \in M} |x_{m\Delta t,n}(\tau; q) - x_{m\Delta t,n}(\tau; q')| \tag{2.12a}$$

$$\textit{FuzzyEnt}: \quad d_F(\tilde{\boldsymbol{x}}_n(\tau, M; q), \tilde{\boldsymbol{x}}_n(\tau, M; q')) = \exp(d_S(\tilde{\boldsymbol{x}}_n(\tau, M; q), \tilde{\boldsymbol{x}}_n(\tau, M; q'))^2/\rho) \tag{2.12b}$$

where $\rho{\sim}0.1\sigma_{\tilde{\boldsymbol{x}}}$ and $\sigma_{\tilde{\boldsymbol{x}}}$ is the standard deviation of the measured EEG data.

Symbolic Spaces using Quantized Stochastic Patterns

The pattern count in Eq. (2.10) can be alternatively assessed through the conditional probability that two stochastic models, extracted from the same embedded representation in Eq. (2.9), are similar [96]. In particular, we estimate the conditional probability $p\left(\overline{\boldsymbol{x}}_n(\tau, M; \cdot)|X_n(\tau, M)\right)$ that reflects the closeness between the original expanded state-space partition set, $X_n(\cdot, \cdot)$ and every element of an equivalent stochastic representation with reduced dimension, $\overline{\boldsymbol{x}}_n(\cdot, \cdot; \cdot){\in}\mathbb{R}^M$, created from the original set. Thus, we rewrite the Entropy-based estimation, performed within τ, as below:

$$\begin{aligned}\mathbb{H}\left\{X_n(\tau, M); \rho\right\} &= \mathbb{H}\left\{(\overline{\boldsymbol{x}}_n(\tau, M; q')|X_n(\tau, M))\right\} \\ &= -\sum_{q' \in Q'} p\left(\overline{\boldsymbol{x}}_n(\tau, M; q')|X_n(\tau, M)\right) \log p\left(\overline{\boldsymbol{x}}_n(\tau, M; q')|X_n(\tau, M)\right), \end{aligned} \tag{2.13}$$

where the reduced set holds $Q'{\leq}Q$ symbols $\overline{\boldsymbol{x}}_n{\in}\overline{X}_n(\cdot, \cdot)$, which are assumed to be more distinct across the whole embedded representation.

We model the alternative embedded set, noted as $\overline{X}_n(\cdot, \cdot){\in}\mathbb{R}^{Q' \times M}$, using quantization techniques, which compress a larger dataset in Eq. (2.9) into one smaller equivalent set of code vectors. In particular, we employ the approach described in [97] that finds the closest code-vector representation.

Nevertheless, the similarity pattern count calculation in Eq. (2.11) will necessitate more statistics due to the reduced size of the newly introduced embedding stochastic set. Instead, we propose to build the probabilistic priors in Eq. (2.10) between both representations (original and VQ-reduced) by calculating the conditional probability that a sample of the unfolded EEG signal belongs to every formed VQ symbol. So, according to Bayes theorem, we have:

$$p\left(\overline{\boldsymbol{x}}_n(\tau, M; q')|X_n(\tau, M)\right){=}p\left(X_n(\tau, M)|\overline{\boldsymbol{x}}_n(\tau, M; q')\right) p\left(\overline{\boldsymbol{x}}_n(\tau, M; q')\right)$$

Assuming that the input samples follow a Gaussian distribution, we employ the similarity-based approach between sets for estimation of both probabilistic terms, as proposed in [98]:

$$p\left(X_n(\tau, M)|\overline{\boldsymbol{x}}_n(\tau, M; q')\right) \sim \mathcal{N}\left(X_n(\tau, M)|\boldsymbol{\mu}_{q'}, \boldsymbol{\sigma}^2_{q'}\right) = \mathbb{E}\left\{\gamma\left(\tilde{\boldsymbol{x}}_n(\tau, M; q)|\boldsymbol{\mu}_{q'}, \boldsymbol{\sigma}^2_{q'}\right)\right\} \tag{2.14a}$$

$$p\left(\overline{\boldsymbol{x}}_n(\tau, M; q')\right) = \mathbb{E}\left\{p\left(\tilde{\boldsymbol{x}}_n(\tau, M; q) = \overline{\boldsymbol{x}}_n(\tau, M; q')\right), \forall q\right\} \tag{2.14b}$$

where $p\left(\tilde{\boldsymbol{x}}_n(\tau, M; q) = \overline{\boldsymbol{x}}_n(\tau, M; q')\right)$ is the probability that a symbol belongs to every element of the dictionary, $p\left(\tilde{\boldsymbol{x}}_n(\tau, M; q) = \overline{\boldsymbol{x}}_n(\tau, M; q')\right) = \gamma\left(\tilde{\boldsymbol{x}}_n(\tau, M; q), \overline{\boldsymbol{x}}_n(\tau, M; q')\right)$, being $\gamma(\cdot)$ a Gaussian similarity function, and $\boldsymbol{\sigma}^2_{q'} \in \mathbb{R}, \boldsymbol{\mu}_{q'} \in \mathbb{R}^M$ the moments computed, respectively, as below:

$$\boldsymbol{\mu}_{q'} = \sum_{\forall q} \tilde{\boldsymbol{x}}_n(\tau, M; q) p\left(\tilde{\boldsymbol{x}}_n(\tau, M; q) = \overline{\boldsymbol{x}}_n(\tau, M; q')\right)$$

$$\boldsymbol{\sigma}^2_{q'} = \sum_{\forall q} \left(\tilde{\boldsymbol{x}}_n(\tau, M; q) - \boldsymbol{\mu}_{q'}\right)^\top \left(\tilde{\boldsymbol{x}}_n(\tau, M; q) - \boldsymbol{\mu}_{q'}\right) p\left(\tilde{\boldsymbol{x}}_n(\tau, M; q) = \overline{\boldsymbol{x}}_n(\tau, M; q')\right)$$

Therefore, the proposed Entropy-based estimator, termed *VQ-En*, builds the probabilistic priors by assessing the Gaussian similarity between the input and vector-quantized representations for dealing with the scarce statistics because of small code-vector sets (formed through the Euclidean distance), as detailed in Algorithm 1.

Algorithm 1 Building of VQ stochastic patterns.

procedure VECTOR QUATIZATION IN X
  Input: $\tilde{\boldsymbol{x}}_n(\tau, M; q), q \in [1, Q]$
  Initialize the reduced set $\overline{X}_n(\tau, M)$, then $\overline{\boldsymbol{x}}_n(\tau, M; 1) = \tilde{\boldsymbol{x}}_n(\tau, M; 1)$
  for $q \in [2, Q]$ **do**
    Compute the distance between $\tilde{\boldsymbol{x}}_n(\tau, M; q)$ and $\overline{X}_n(\tau, M)$. $d(\tilde{\boldsymbol{x}}_n(\tau, M; q), \overline{X}_n(\tau, M)) = ||\tilde{\boldsymbol{x}}_n(\tau, M; q) - \overline{\boldsymbol{x}}_n(\tau, M; q')||_2^2, q' \in [1, Q']$
    if $||d(\tilde{\boldsymbol{x}}_n(\tau, M; q), \overline{X}_n(\tau, M)) > \rho||_1 = Q'$ **then**
      $\overline{X}_n(\tau, M) \leftarrow \tilde{\boldsymbol{x}}_n(\tau, M; q)$
      $Q' = Q' + 1$
    end if
  end for
end procedure

2.2 Intra-subject Neural Response Variability

2.2.1 A New Proposal for Group-level Extraction of Multi-subject *t-f* Features

The goal is to capture the inter-subject *t-f* feature dynamics, which are to be considered as prevalent in the group/population level, guaranteeing that the MI responses are measured from subjects under the identical conditions of the experimental paradigm. We assume that the collected data are statistically independent between individuals. Under this assumption, the common assessments of the extracted feature sets become confident as

they are present in a higher number of subjects. In this regard, the subject-level model provides a set of confident estimates that contributes the most to discriminating between tasks using the following supervised, statistical thresholding algorithm [99]:

$$\kappa_s^f(c) = \begin{cases} 1, & \mathcal{M}\{\boldsymbol{\theta}^{cfs}(\tau)|\lambda : \forall \Delta_{T_i}\}<p \\ 0, & \text{Otherwise,} \end{cases}$$

where the rule $\mathcal{M}\{\cdot|\lambda{:}\forall\Delta_{T_i}\}$ computes the statistical discrepancy/consistency along Δ_{T_i} time window using a non-parametric Mann-Whitney test under the null hypothesis that the distribution of all channels is equal. Thus, $\kappa_s^f \in^C$ holds the p-values for all the considered channels. Besides, we apply the Kolmogorov-Smirnov and Bartlett's tests to address these issues since the estimated set can present failures related to normality and homoscedasticity. Because we know the channel's discriminant capacity of each subject, and assuming the independence of the performed validation, we accomplish a group-level analysis using the positive False Discovery Rate as a robust statistical correction in the multiple-subject comparison testing.

We also evaluate the ability of multi-subject sets to preserve the main properties obtained from the single-subject model sets. Namely, we quantify the variations in the spatial distribution of common brain neural activity raised by the heterogeneity between subjects due to the reported dependence of individual skills for adequately practicing the MI tasks. As mentioned before, we build a group-level model for the BCI-literacy group in either tested database. Thus, we appraise the inter-group topographical variability between attained multi-subject dynamics. Besides, the intra-similarity of the extracted individual dynamics is presented to estimate the influence of each subject on the performed dynamic multi-subject model. So, we compute muti-subject models over all subjects. Then, the multi-subject model is calculated by removing the subject with the worst accuracy. Next, the multi-subject model is evaluated by subtracting the tow worst subjects, and so on, desegregating each individual by the ranked accuracy. Here, we calculate the topographical similarity using a generalized inner product measured between a couple of spatial dynamics, $\boldsymbol{\eta}$ and $\boldsymbol{\eta'}$, projecting the difference of data onto a reproducing kernel Hilbert space through a Gaussian kernel as follows [100]:

$$\langle \boldsymbol{\eta}, \boldsymbol{\eta'} \rangle_\sigma = \exp\left(-\|\boldsymbol{\eta} - \boldsymbol{\eta'}\|^2/\sigma^2\right) \tag{2.15}$$

where $\sigma \in \mathbb{R}^+$ is a ruling parameter for which the estimate is obtained from the MI segment.

2.2.2 Electrophysiological Indicators in MI Tasks

Pre-training Indicator of Neural De/synchronization

For quantifying the potential for desynchronization at rest over the sensorimotor area, the spectral variability of a state of wakefulness conscious can be assessed by computing the difference between the EEG background activity (a fit of f^{-1} noise spectrum) and the spectral content of those rhythms that are directly related to MI responses (i.e., μ and β). Thus, the pre-training neural predictor, noted as $\xi_1 \in \mathbb{R}^+$, is estimated while using the

following fitting-curve based approach developed in [1]:

$$\xi_1 = \max_{\forall f \in \boldsymbol{f}} \{\boldsymbol{\delta}(f) - \varepsilon(f; \iota^*, \boldsymbol{o}^*)\} \tag{2.16a}$$

$$\iota^*, \boldsymbol{o}^* = \{\arg \min_{m_\Omega, \sigma_\Omega, \iota, k_\Omega, \boldsymbol{o}} \|\boldsymbol{\delta}(f) - \big(\sum_{\Omega=\mu,\beta} k_\Omega \mathcal{N}_\Omega(f; m_\Omega, \sigma_\Omega) + \varepsilon(f; \iota, \boldsymbol{o})\big)\|_2\} \tag{2.16b}$$

where $\boldsymbol{\delta}(f)$ is the positive semi-definite power spectral density (PSD) computed from an a priori given state of wakefulness, $\mathcal{N}(f; m_\Omega, \sigma_\Omega)$ is a Gaussian function modeling each spectral peak of either sensorimotor rhythm $\Omega{=}\{\mu, \beta\}$, widely reported for practicing MI tasks [101]; $\{k_\Omega{\in}\mathbb{R}^+\}$ are the summation rhythm weights; $\{m_\Omega{\in}\mathbb{R}^+\}$ and $\{\sigma_\Omega{\in}\mathbb{R}^+\}$ are the spectral moments ruling the offset and scale of each fitting function, respectively; $\varepsilon(f; \iota, \boldsymbol{o}){=}o_1 + (o_2/f^\iota)$ is the hyperbolic fitting of noise with parameters $\{o_1{\in}\mathbb{R}^+, o_2{\in}\mathbb{R}^+\}$, $\iota{\in}\mathbb{R}^+$. Notation $\|\cdot\|_p$ stands for ℓ_p-norm.

Initial training indicator of Event-related De/Synchronization

For a measured EEG recording, the estimation of ERD/S is performed, by squaring the samples and averaging over the EEG trial set to compute the variational percentage (decrease or increase) in EEG signal power regarding a given reference interval, as in Eq. (2.6) [102]. Intending to provide a scalar-valued assessment of the synchronization mechanism, the initial training indicator, which is noted as $\xi_2{\in}\mathbb{R}^+$, is the distance measured between both labeled ERD/ERS time-series ($\lambda{=}l, l'$, denoting left-hand and right-hand tasks, respectively). ERD/ERS are extracted within each rhythm Ω at channel c, as below:

$$\xi_2 = \max_{\Omega, c} \left\{ \frac{\|\hat{\zeta}(\Omega, c|l) - \hat{\zeta}(\Omega, c|l')\|_2^2}{\|\hat{\zeta}(\Omega, c|l)\|_2 \|\hat{\zeta}(\Omega, c|l')\|_2} \right\} \tag{2.17}$$

where $\zeta(\Omega, c|\lambda)$ is the estimated ERD/ERS at channel c and bandwidth Ω, selecting the baseline inverval as reference. The reported values of ξ_2 are computed using the maximization operator in Equation (2.17), relying on the fact that a single ERD/ERS time series may occur at different electrodes and bandwidths, being sufficient to provide an adequate neural response.

2.2.3 A New Porposal for Evaluating the BCI Efficiency using Classifier Performance and Electrophysiological Indicators

For evaluating the BCI efficiency, we employ a learning rule that estimates an unknown function $O{:}\mathbb{R}^S{\mapsto}\mathbb{R}$ from representative observations of an individual indicator (independent variable) $\boldsymbol{\xi}{\in}\mathbb{R}^S$, for which a multivariate model-free regression problem can be stated through by optimizing, across the subject set $s{\in}S$, the following framework:

$$\min_{\boldsymbol{\pi}} \mathbb{E}\left\{\|\boldsymbol{\nu} - (O\{\boldsymbol{\xi}(\boldsymbol{x}_m)|\boldsymbol{\pi}\} + \boldsymbol{\epsilon})\|_p : \forall s \in S\right\}, \tag{2.18}$$

where $\boldsymbol{\nu}{\in}\mathbb{R}^S$ is the response vector (dependent variable), $\boldsymbol{\epsilon}{\in}\mathbb{R}^S$ is the additive error term that is independent of $\boldsymbol{\xi}$, and $\boldsymbol{\pi}$ is the unknown parameter vector that allows estimation of the function $O(;)$ that fits the data most closely in terms of a given ℓ_p-norm distance.

Here, the framework in Equation (2.18) is further developed by a proposed data-driven estimator, termed Deep Regression Network (DRN), which jointly extracts and performs the regression analysis, as follows:

$$\min_{\boldsymbol{\pi}} \mathbb{E}\left\{\|\psi(V_s) - (O_3 \circ O_2 \circ O_1\{\boldsymbol{\xi}(\varphi(\boldsymbol{x}_s^c)) : s, c{\in}S, C'\}|\boldsymbol{\pi}\})\|_1 : \forall s \in S\right\} \tag{2.19}$$

where the initial hidden layer O_1 extracts through the function $\varphi(\boldsymbol{x}^c)$ as a set of salient patterns from all EEG recordings measured at every electrode $\boldsymbol{x}^c$, O_2 is the fully-connected layer that maps the first-layer inputs into a high-dimensional space, generalizing the salient patterns sets over the considered channel configuration C' in order to assess the subject indicator $\boldsymbol{\xi}^*$, O_3 is the output layer fed by the response set of individuals to perform the regression analysis by incorporating a linear activation function, $\psi(V_s)$ is a functional that maps the scalar-valued response set V_s assessed for each subject into a single value.

Figure 2.1 sketches the proposed Deep Regression Network architecture that is based on the non-sequential Wide&Deep neural network to perform learning of deep patterns (using the deep path) under simple rules (through the short path) [103], implemented as below:

- **IN**: input layer that holds the extracted relevant patterns $\{\varphi(\boldsymbol{x}_s^c){:}\forall c, m\}$.
- O_1: fully-Connected layer that is used for extracting robust and epileptic relevant patterns that are mapped into a high-dimensional latent space [104], holding $h{=}\lceil 1.5\,\text{size}\,(\{\varphi(\cdot)\})\rceil$ neurons, being $\lceil\cdot\rceil$ the ceiling operator.
- **CT**: a concatenate layer that condenses the resulting feature sets of all electrodes into a single block, sizing hC'.
- O_2: a fully-connected layer with size $\lceil 0.5hC'\rceil$ that is linked to each output-layer neuron.
- O_3: the one-neuron regression equipped with a linear activation function to predict the response.

Using the proposed Deep Regression Network framework, we extract the subject vector, which is noted as $\boldsymbol{\xi}^*$, as an indicator of MI neural activity that is further correlated with the computed bi-class accuracy as a response variable. To this end, the parameters in Equation (2.19) are adjusted, as follows:

- The set of relevant patterns $\{\varphi(\boldsymbol{x}_s^c)\}$ that holds elements extracted by the following statistical moments: mean, median, variance, minimal, and maximal values. For every subject, the moments are estimated over $\boldsymbol{x}^c$ data using a short-time window lasting 1 s with a 50% overlap. All time-varying moments are concatenated to form a single set per channel.
- Both layers, O_1 and O_2, employ a hyperbolic tangent ($tanh$) as the activation function.

- During learning, *Adam algorithm* optimizer and *loss function* are used, measuring the Mean Absolute Error and fixing the learning rate to 10^{-3}. In addition, the weight values (empirically set to 10^{-3}) are regularized while using the Elastic Net regularization.

- The backpropagation algorithm solves the parameter set optimization of $\boldsymbol{\pi}$ with auto differentiation under a Wide Deep Neural Network framework that includes two hidden layers under elastic-net regularization.

- As the function mapping $\psi(V_s)$, two operators over the response vectors are tested: (a) the mean accuracy (noted as mean) that is averaged across the extraction window lengths $\delta\tau$ and weighted by the subject variance performed at each window; (b) first PCA component of the accuracy vectors (noted as PCA_1).

- For evaluation purposes, we also contrast the DRN-based regression analysis with the case of avoiding the data-driven indicator extraction. Which is, the estimator in Equation (2.19) is directly fed by the scalar-valued neurophysiological indicators devised in Equations (2.16a) and (2.17), fixing each individual vector element of $\boldsymbol{\xi}^*$ to $\xi^*{=}\xi_{1,2}$ and removing the concatenation layer **CT**.

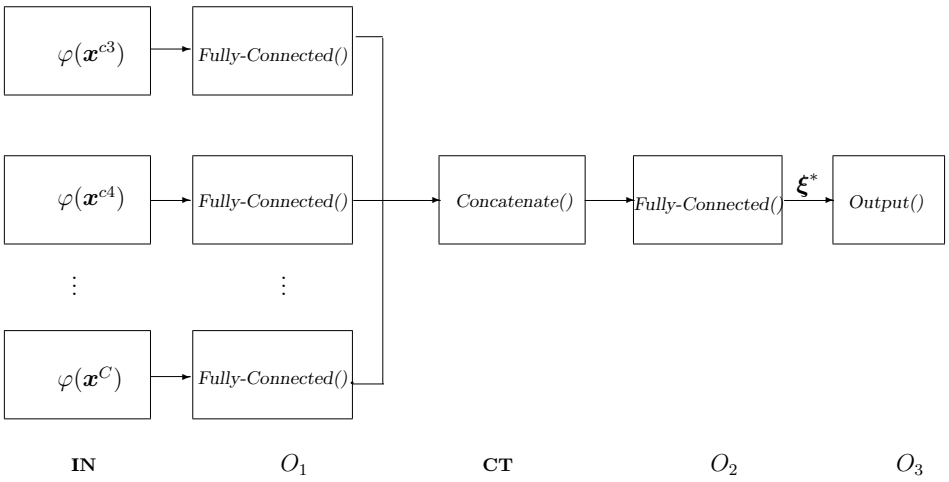

Figure 2.1: Proposed Deep Regression Network with three-layers architecture corresponding to the extraction of salient sensorimotor patterns, subject indicator computation, and the linear regression of performance responses on the assessed indicator vector.

2.3 Description Tested of Bi-task MI Databases

In this section we describe the employed BCI based MI tasks datasets for each one of our proposed approaches.

2.3.1 Dataset D-I: BCI Competition IV

We perform experimental validation in nine subjects (M=9) of Dataset 2a[1], holding EEG signals acquired from the scalp by a C-channel montage (C=22). Every raw EEG channel $\boldsymbol{x}(c)\in\mathbb{R}^T$ was sampled at 250 Hz (i.e., at the sample rate Δt=0.004 s). To perform each MI task (left and right hand with labels noted as $\lambda\in\{l, l'\}$, respectively), a short beep noticed the trial beginning, followed by a fixation cross that appeared on the black screen within the first 2 s-interval. An arrow (cue) appeared during 1.25 s, and pointed to the induced direction. Then, each subject performed a demanded MI task while the cross reappeared within the next time interval, starting from 3.25 s to the recording end. All signals were collected in six runs separated by short breaks, performing N_λ=72 trials per class and each lasting T=7 s. Of note, we only examined the labeled trials for which artifact removal had been applied.

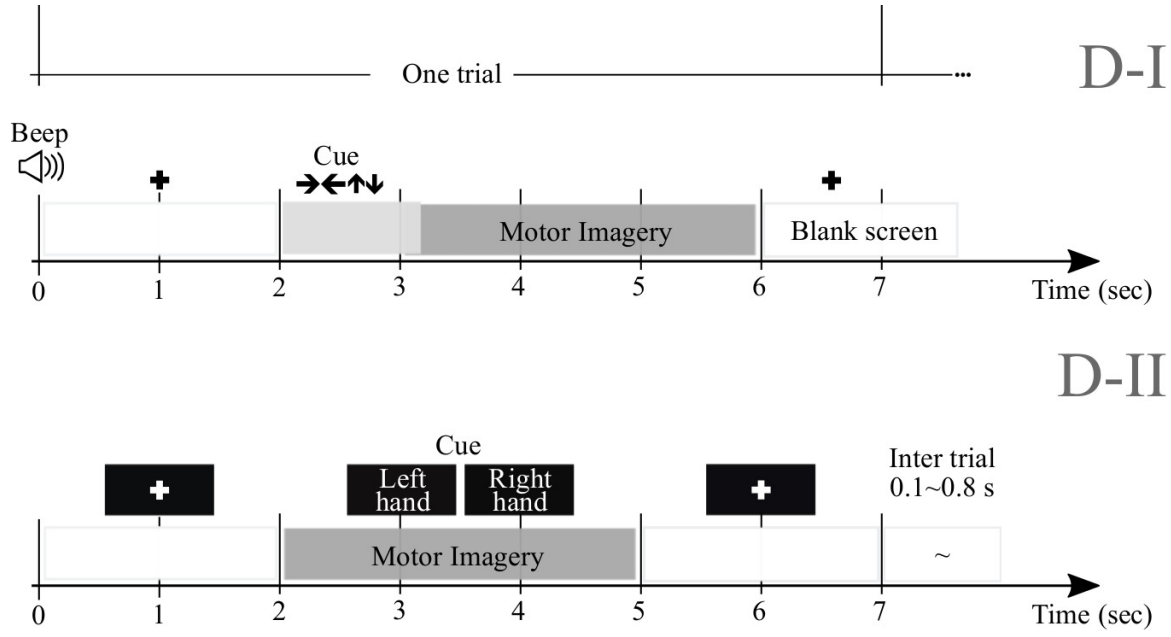

Figure 2.2: Trial timing used to implement the MI paradigm of the tested databases

2.3.2 Dataset D-II: Gigascience

We also examine this collection that holds EEG data obtained from fifty-two subjects (although only M=50 are available) using a 10-10 placement electrode system with C=64

[1] *BCI Competition IV*, publicly available at www.bbci.de/competition/iv/

channels[2]. Every channel $\boldsymbol{x}(c)$ lasted T=7 s and sampled at F_s=512 Hz. At the trial beginning, a fixation cross was presented on a black screen within a period that lasted 2 s. Then, a cue instruction (related to either label – l or l') appeared randomly on the screen for 3 s that inquired each subject to imagine moving his/her fingers, starting to form the index finger and proceeding to the little finger and touching each to their thumb. Afterward, a blank screen was shown at the beginning of a break period, lasting randomly between 4.1 and 4.8 s. For completing a single run, this procedure was repeated over 20 times and stopped at the end to fulfill a written cognitive questionnaire [105]. Every subject performed five or six runs. Additionally, a single-trial recording of resting-state lasting 60 s was collected from each subject.

Fig. 2.2 displays the trial timing used to implement the MI paradigm of the tested databases: D-I and D-II.

[2]http://gigadb.org/dataset/100295

Chapter 3

Experiments and Results of Subject-Level Extraction of *t-f* Feature Dynamics

Validation of the proposed approach includes *i*) Decomposition of input EEG time-series into a frequency-specific temporal representation; *ii*) Subject-level feature extraction of *t-f* dynamics, encoding the electrode contribution accordingly considered feature extraction approaches.

3.1 Preprocessing of EGG signals

Initialily, every raw EEG channel $\boldsymbol{x}(c)$ is band-pass filtered in the frequency range $f \in$[4-40] Hz using a filterbank of N_f=17 filters with 2 Hz bandwidth overlap. For either considered database, the bandwidths are selected to cover μ and β, widely reported for practicing MI tasks [93]. However, as suggested in [106], we split β oscillation into three bandwidths, namely, [16-20], [20-24], and [24-28] Hz. Spectral partitioning is carried out within the following time-window lengths (namely, τ_J=[0.5, 1, 1.5, 2] s with 90% overlapping). Then, to provide physiological interpretation according to the implemented experimental paradigm of MI, the dynamics are analyzed at the following representative intervals of interest: ΔT_1=[0-2] s (interval prior to cue-onset or task-negative state), ΔT_2=[0.8-2] s (cue-onset interval), ΔT_3=[2.6-4.6] s (motor imagery interval), ΔT_4=[3.8-5.8] s (decaying motor imagery interval), and ΔT_5=[4.4-6.4] s (break period). For addressing the volume conduction problem, all *t-f* patterns are computed by performing the Laplacian filter previously over the input EGG data to improve the spatial resolution of EEG recordings, avoiding the influence of noise coming from neighboring channels [107]. We implemented spatial filtering using *Biosig Toolbox*[1].

Pipeline for classification xxxx ponr ventana deslizante

[1] http://biosig.sourceforge.net

3.2 Inter-subject Varibility and its Impact on Classification Accuracy

One aspect significantly influencing the extraction of dynamics is the subject's ability to evoke high-quality and recognizable MI responses. To manage inter-subject variability, we assume the rationale by which the more developed the individual brain network, the higher the accuracy in distinguishing between MI tasks. Accordingly, depending on whether a subject has skills to master MI applications, both databases are split into two subject assemblies: BCI-literacy and BCI-illiteracy. poner que el estado del arte 80% es literate.

To manage the significant impact of inter-subject variability on the reached accuracy, BCI-literacy, or users with the ability to produce reliable and reasonably robust differences in neural activity between distinct MI tasks (e.g., left-hand vs. right-hand) [108], and BCI-illiteracy, or individuals who are not accurate enough to control the MI application.

We rank the subject set in decreasing order of the average discrimination accuracy in Fig. 3.1a (D-I) and Fig. 3.1b (D-II), where a dashed vertical line separates both assessed assemblies, displaying the individual performance estimated at different window lengths. As a result, the D-I collection holds 6 BCI-literacy subjects and 3 BCI-illiterate. In turn, D-II contains 23 BCI-literacy subjects, and the remaining 27 are BCI-illiterate.

The time-evolving accuracy reveals that the optimal value of τ_J provides the best accuracy and varies widely across subjects and ranges within the entire span of the tested window length. Table 3.1 presents the mean and standard deviation of accuracy, averaged across the subject set, indicating that the average performance tends to increase as the length τ_J shortens. However, the accuracy degrades for the smallest window. Because one more concern in choosing τ_J is the need for sufficient statistics to estimate the collective dynamics, we fix the optimal window to τ_J^*=1 s as a tradeoff between accuracy and an adequate number of samples on the interval of interest in implementing the multi-subject modeling.

Table 1. Accuracy of the extracted RQ time-series, varying τ_J. Notation *All* stands for averaging across the while group, while *Literate* and *Illiterate* represent the corresponding subject subset computation.

	D-I			**D-II**		
τ_J	***All***	***Literate***	***Illiterate***	***All***	***Literate***	***Illiterate***
0.5	83.8± 6.6	91.3±5.3	80.5±4.0	85.6±9.0	92.1±7.6	77.6±3.2
1.0	**84.1 ± 7.9**	94.1±4.1	79.8±4.5	**85.7 ± 10.9**	94.1±5.5	75.2±7.5
1.5	82.8± 9.8	93.0±5.4	78.0±7.1	87.6±11.3	96.0±4.0	77.2±10.0
2.0	82.1±11.3	95.0±5.3	76.5±8.3	87.2±11.6	95.4±3.9	77.0±11.8

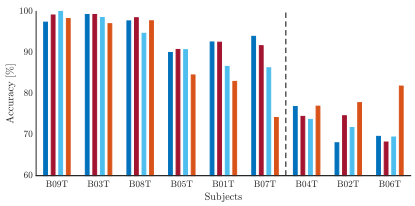

(a)

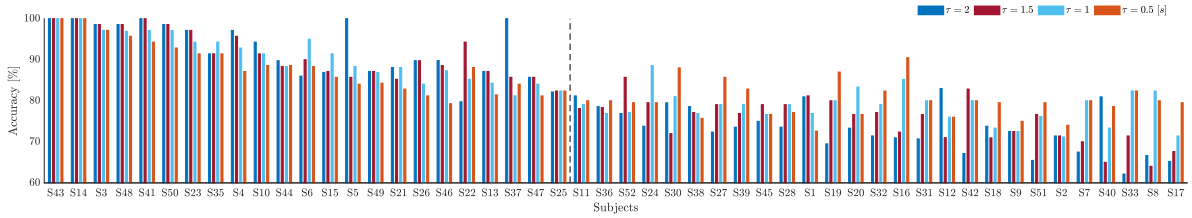

(b)

Figure 3.1: Individual classifier accuracy of MI tasks estimated for D-I (a) and D-II (b) at different window lengths (Subjects are ranked in decreasing order of performance at τ_J^*=1). c) Accuracy averaged across all subject set. The dashed line separates the BCI-literate subjects from BCI-illiterate ones.

3.3 Single-subject Dynamics Performed by Common Spatial Patterns

After selecting the bandwidth setup, the starting point to implement the short-time feature extraction of t-f CSP dynamics is the computation of RQ time-series by adequately tuning the time window length τ_J and by fixing the variance of the surrogate space to the first eigenvectors (k=3) of the matrix $\boldsymbol{W}_{f\tau}$. Therefore, using a tailored software, we extract two feature sets from each time-frequency segment: $D \in \mathbb{R}^{144\times 102}$ for D-I and $D \in \mathbb{R}^{200\times 102}$ for D-II.

For illustration purposes, we present the extracted CSP dynamics just for several representative subjects, who have been reported as having high accuracy (BO8T for database D-I, and S43, S14, S46 for D-II) and low accuracy (BO2T for D-I, and S10, S38, and S2 for D-II). Fig. 3.2 presents the t-f features performed individually, revealing a very changing behavior of the assessments. This fact becomes evident in the accuracy evolution over time displayed under each plot of CSP-based dynamics.

Also, we appraise the spectral contribution by the marginal values of CSP dynamics on each bandwidth of f, as seen on the plots depicted in Fig. 3.2. Thus, the individuals with high accuracy (yellow spots) have a few spectral components powerfully localized, showing that the more contributing waveforms are μ and β. In contrast, the low-accuracy subjects have a weak contribution that tends to spread over all bandwidths, increasing the variability of estimated CSP patterns.

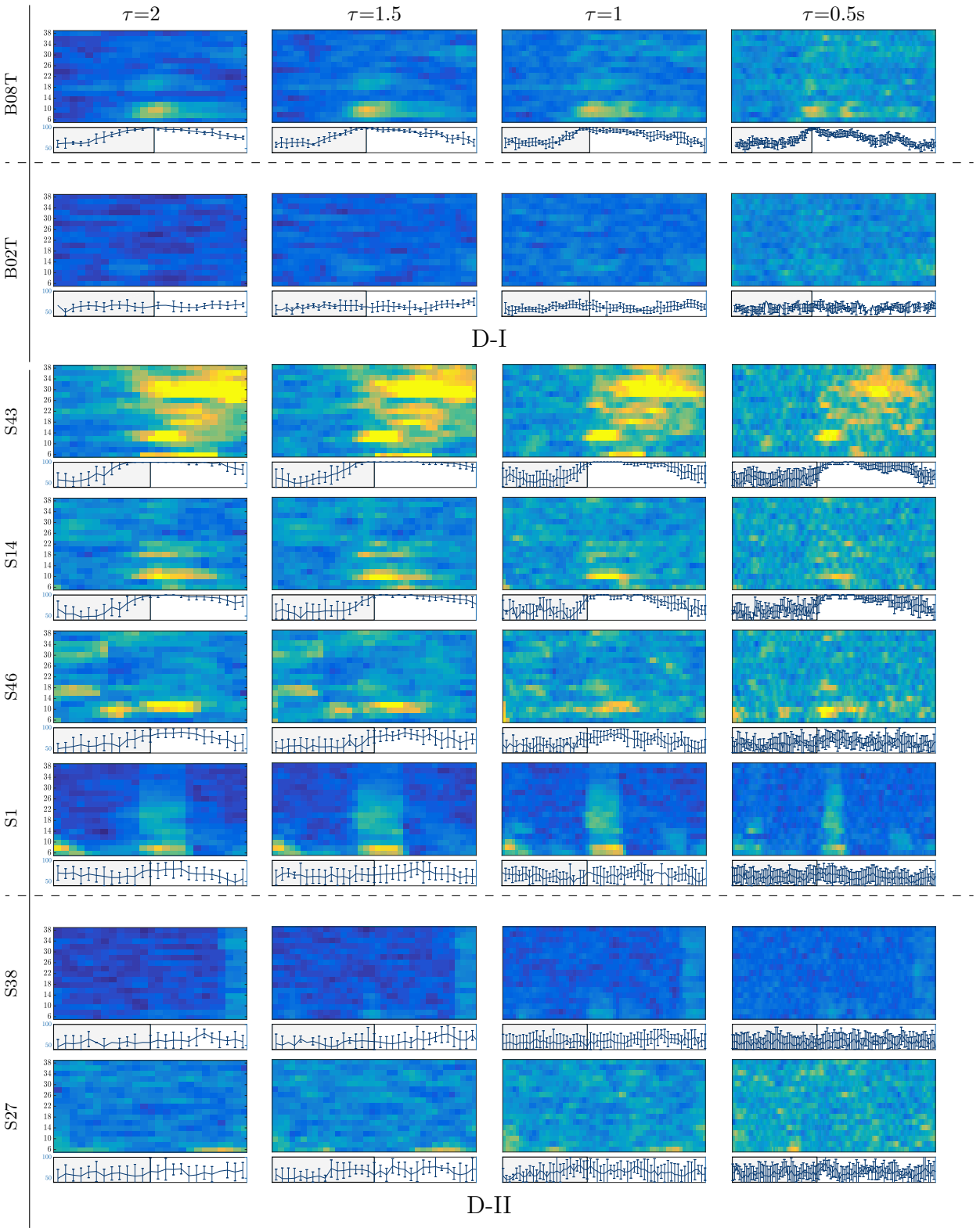

Figure 3.2: *t-f* CSP dynamics computed for representative individuals (BCI-literate and BCI-illiterate) belonging to each tested dataset (D-I and D-II). Under each plot, the accuracy evolution over the interval of neural activation T is displayed for a fixed value of window τ_J.

Another aspect to consider is the representative intervals of interest that influence the most on the MI responses. Thus, in the cases of individuals with higher performance (BCI-literacy), the best accuracy is estimated within ΔT_3, when the most increased neural activation is expected to take place according to the used trial timing. By the opposite, subjects with lower accuracy (BCI-illiteracy) deliver better estimates of performance outside the MI period ΔT_3; their high irregularity may explain this incorrect time localization of relevant MI responses in following the experimental paradigm [109]. Consequently, the more scattered over time and frequency domains the extracted CSP patterns, the lower the accuracy achieved by the subjects.

From Fig. 3.2, it may be concluded that every subject rules the RQ evolution through τ separately. This restriction poses a challenge for extracting multi-subject dynamics, for which a unique value of the time window must be determined across the entire subject set. Another critical point hindering the estimation of RQ maps is the use of CSP-based filtering that demands a long window τ, decreasing the accuracy of the performed *t-f* feature dynamics so that the variability of inter-subject dynamics increases notably due to inherent non-stationarity, artifacts, a low signal-to-noise ratio of EEG signals, individual differences in cortical activity resulting in variations of the covariance matrix and consequently estimated spatial filters [110].

Once the domain parameters (i.e., time window length and filter bandwidth setup) are selected, we compute the topographical representation of brain neural dynamics $\boldsymbol{\theta}_J(f, \tau)$ performed by CSP. For the sake of illustration, Fig. 3.3 displays the neural dynamics performed by representative subjects of both data subsets, that is, BO8T and BO2T in D-I, and S14 and S27 for Dataset D-II. As seen, the filter-bank bandwidths of BCI-literacy individuals that contribute the most fall into μ and β oscillations, involving activity in the centro-lateral primary motor area, supplementary motor area, and primary somatosensory area, as reported in [111]. On the contrary, the illiterate subjects BO2T and S27 hold the spectral contribution that is more localized over the pre-frontal to the mid-central area, being lower on μ and spreading extensively, but with a much lower contribution. Overall, the neural activation dynamics $\boldsymbol{\theta}_J(f, \tau)$ are mostly confined within the cue-onset and MI intervals but rising distinctly in the latter MI period of either subject. Note a few spurious activities within ΔT_1, which may be caused by the overlapping window of estimation.

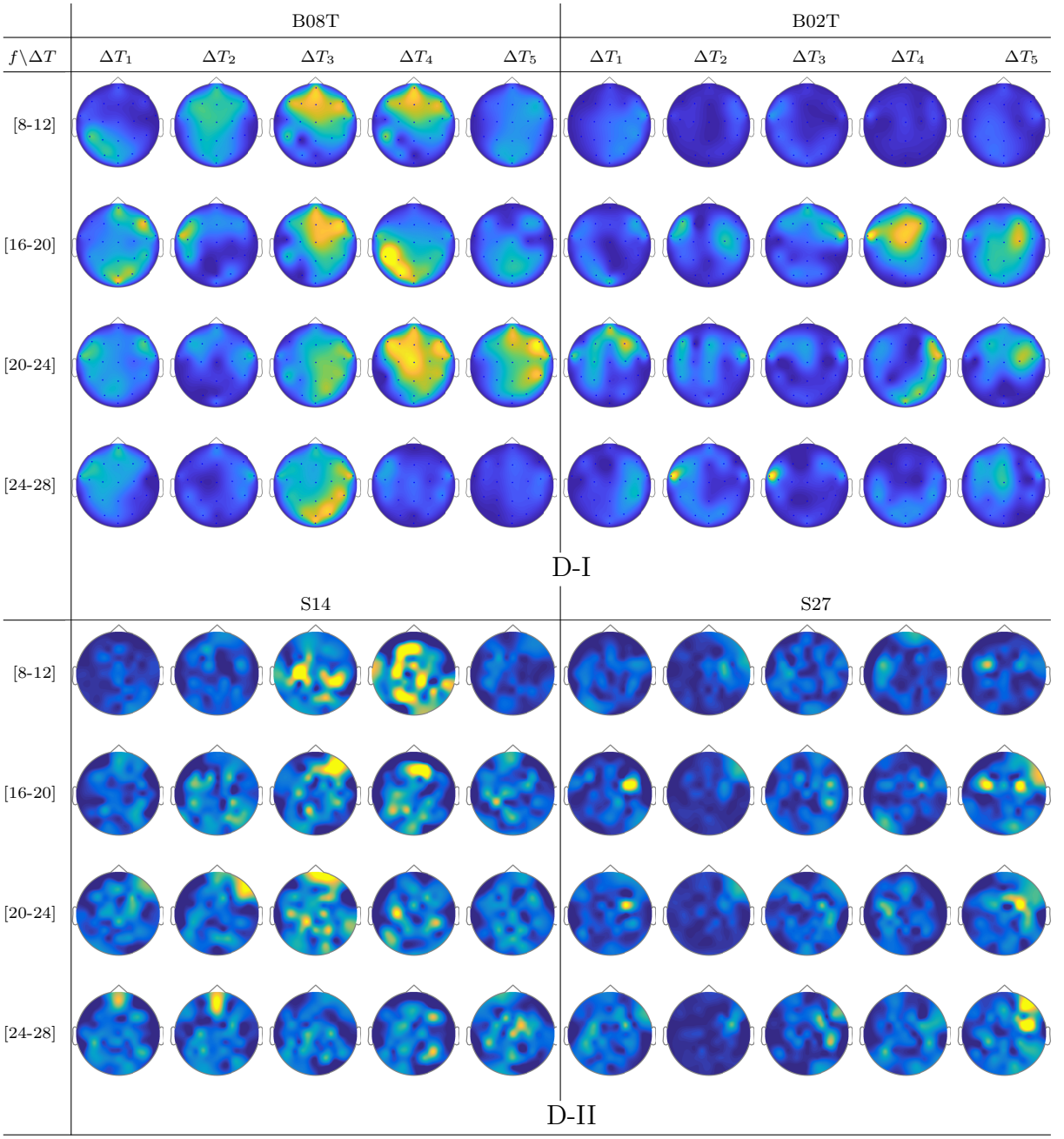

Figure 3.3: Topographical arrangement presenting the *t-f* dynamics of CSP patterns $\boldsymbol{\theta}_J(f,\tau)$ for the subjects performing the best and worst accuracy of each validated database.

3.4 Single-subject Dynamics Extracted by Functional Connectivity

Before extracting the *t-f* functional connectivity features, we perform the preprocessing stage of Laplacian filtering, fixing channel Cz as reference [112]. Nevertheless, the in-

fluential non-stationarity nature of EGG data rules a high variability between trial sets, fluctuating on multiple time-scales that range from milliseconds to seconds [113]. To meet this condition, the estimator in Eq. (2.4) is performed by adjusting the short-time window to a small length, τ_ζ=0.1 s as presented in [114]. Of note, all connectivity assessments are computed using the FielTrip toolbox [115].

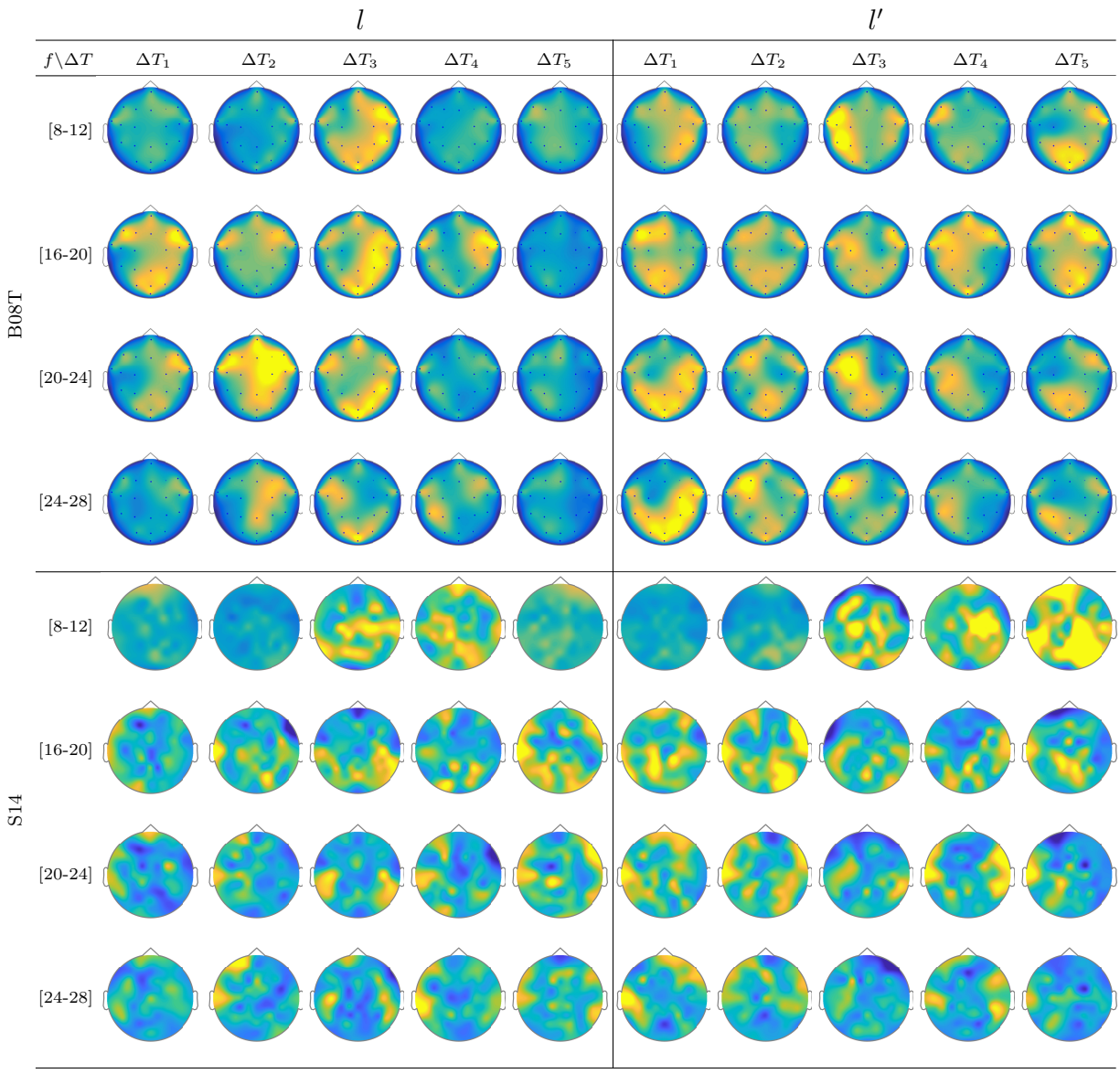

Figure 3.4: Labeled brain neural dynamics, $\boldsymbol{\theta}_\phi(f, \tau|\lambda)$, extracted by the functional connectivity method using *wPLI* and performed by the representative literate individuals: B08T (upper plots) and S14 (lower plots).

Figure 3.4 displays the dynamic of *t-f* features extracted from B08T (upper plots) and S14 (lower plots) that explain a high inter-subject variance of the performed FC patterns. Also, a considerable number of acting nodes is achieved by either individual within the segment before onset, ΔT_1. This background FC activity has been previously associated with some resting-state networks (overlapping the primary motor, visual and auditory

networks, the default mode network, and higher-order attention networks), which are distributed over the frontal, central, parietal, and occipital areas [116]. The FC activity presents a similar behavior over the neighboring interval (ΔT_3 and ΔT_4), including the ending of each MI task and the break period.

In the representative MI interval, ΔT_3, the FC patterns performed by B08T and S14 differ between both classes, covering multiple cortical regions. Thus, neural connectivity is more powerful over the corresponding contralateral hemisphere associated with the parameter-parietal network, as detailed in [117]. Specifically, as stated in [118], the Supplementary motor area, the Premotor cortex, and the posterior parietal cortex are interconnected. An additional aspect to highlight is the evenness of FC dynamics performed by individuals belonging to DB-I due to the lower number of electrodes, yielding lower resolution than the one assessed in DB-II.

3.5 Single-subject Dynamics Extracted by Event-Related De/Synchronization

Further, we extract the ERD/S dynamics from the filtered trial matrix $\boldsymbol{X}^{\lambda}_{N_f N_\tau}$ by fixing the following parameter values: τ_ζ=0.004 s (i.e., time window equals the sample rate), the reference interval ΔT_0=0.5-1.5 s, and the significance value is chosen as 1% in z-score approach (see Eq. (2.6)), as suggested by [119]. Figure 3.5 presents the t-f patterns of ERD modulation performed individually, marking with a red line the cue onset time at 2 s, and with gray dotted line the MI segment, ΔT_3.

The rhythm modulation of ERD/S patterns allows interpreting the experimental paradigm of MI tasks, as seen in Fig. 3.5 that displays the representative changes of t-f patterns estimated for several representative individuals. In the case of literate subjects (B08T, B01T , S43, S14, and S46), the modulation amplitudes are placed over the sensorimotor cortex area. The contralateral electrode power (i.e., electrode C3 for right-hand and C4 – left-hand) decreases stepwise, just before the task onset (marked with a red line) then gradually increases after the corresponding task ends. This behavior holds within the MI interval and is significant in [8-12] Hz and [16-24] Hz bandwidths. Nevertheless, the synchronization patterns are different from each other regardless of their achieved very close accuracy, confirming the widely reported inter-subject variability in practicing MI tasks [76].

For the illiterate subset (B02T, S01, S38, S27), the ERD/S dynamics have weak amplitudes clustered in irregular shape patterns so that the difference in time-locked responses between contralateral and ipsilateral tends to disappear, as it is the case for B06T and B02T for which the neural synchronization effect can be barely observed because of their high inter-subject variability.

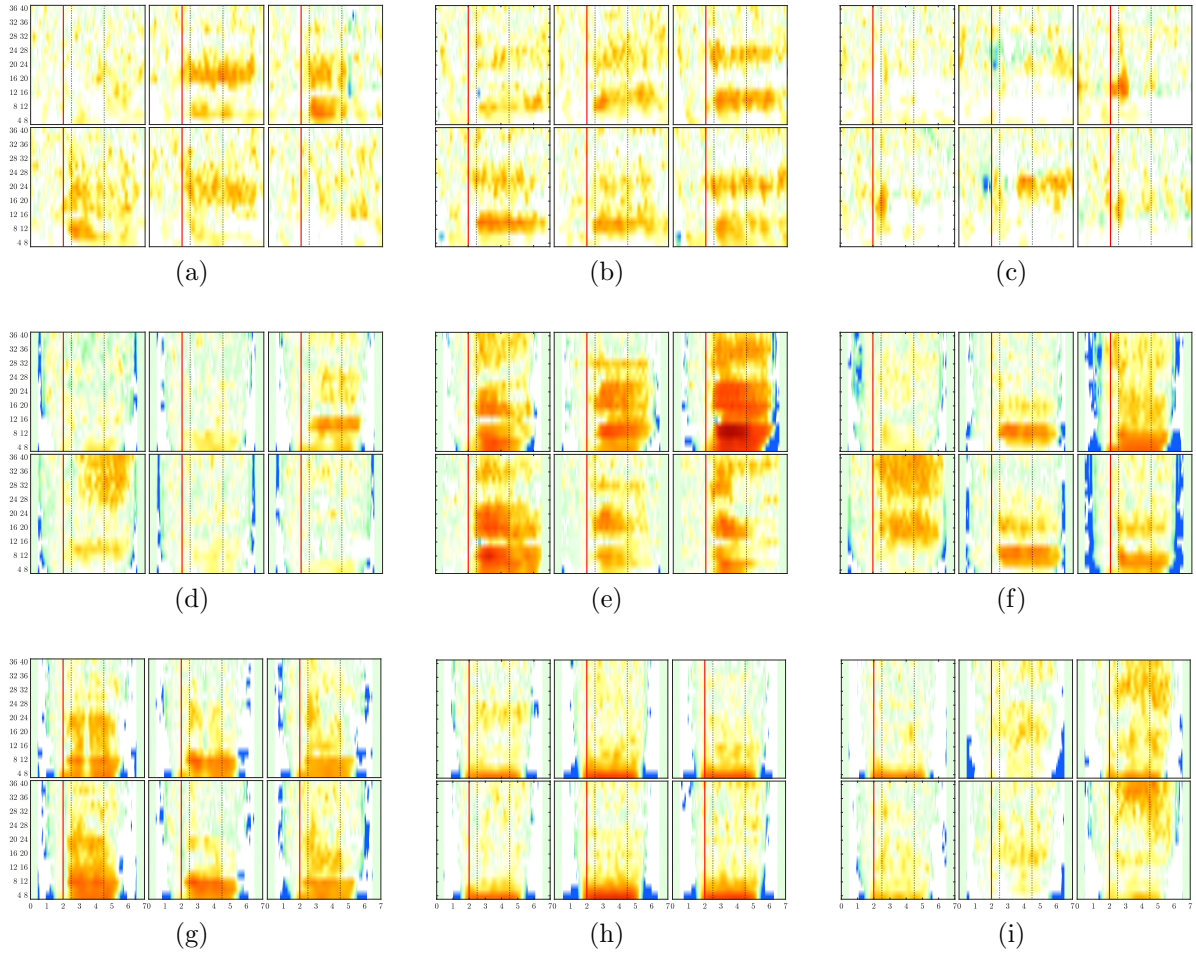

Figure 3.5: ERD/S maps of channels placed above the sensorimotor cortex areas (C3, Cz, and C4) performed by each subject. The rhythm modulation amplitudes are presented for label l – left hand (upper row) and l' – right hand (bottom row). *(a)* B08T, *(b)* B01T, *(c)* B02T, *(d)* S43, *(e)* S14, *(f)* S46, *(g)* S01, *(h)* S38, and *(i)* S27.

Another result is the variational increase in the ERD modulation that can be perceived on either electrode of the sensorimotor cortical area. As observed in Fig. 3.5, a robust right-hand modulation appears at the contralateral C3 electrode in most of the individuals. The higher the accuracy, the more intense the modulation amplitudes. This effect may be linked to left hemisphere dominance, which is commonly reported for motor sequencing tasks [120]. Alternatively, the left-hand modulation located at C4 is less evident at μ and β bands, appearing in S38 and S27. In some cases, the modulation is also presented at the ipsilateral C3 electrode, lessening the ERD/S mechanism, which probably leads to poor accuracy.

As seen in Fig. 3.6, while there is no neural activity measured before the cue ΔT_1 regardless of the frequency band and performed tasks. The main dynamics take place over the interval ΔT_3, showing a higher contribution of MI-related bands (namely, [8-12], [16-20], and [20-24] Hz), as reported for hand movement tasks [121]. Afterward, the ERDS-

based dynamics decrease over time (ΔT_4 and ΔT_5). Note the asymmetrical contribution of the contralateral electrodes for each label.

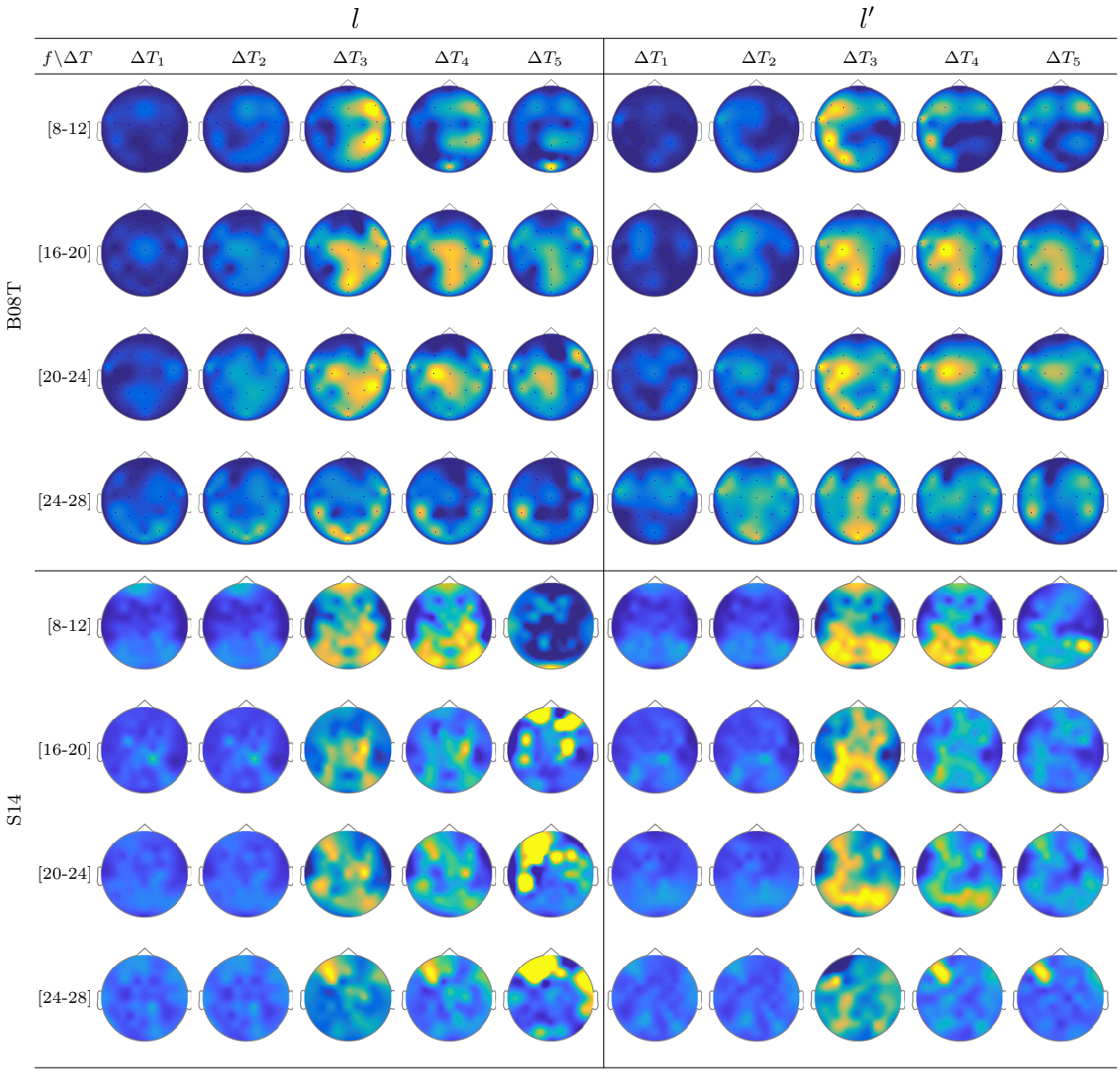

Figure 3.6: ERD/S analysis. Topoplots of the extracted dynamics $\boldsymbol{\theta}_\zeta(f, \tau; c|\lambda)$, showing the dominance to different extents, performed by B08T (class l left side) and (class l' right side)

Chapter 4

Experiments and Results of Complexity-Based Estimation of Event-Related De/Synchronization

We validate the proposed *VQEnt* approach for estimation of event-related De/Synchronization experimentally on a public collection of EEG signals recorded in a 22-electrode montage (see D-I description in Section 2.3 for details). The entropy-based approach includes the following stages: (*i*) Tuning of Entropy-based estimators: short-time window, Embedding dimension, and tolerance. (*ii*) Estimation of time-series for Event-Related De/Synchronization, aiming to explore their interpretation ability, and (*iii*) Activation of the sensorimotor area in distinguishing between MI tasks. Of note, tuning and validation are carried out within the MI interval, that is, $[2.5 - 4.5]$ s.

4.1 Preprocessing of EGG signals

The stage comprises data filtering, segmentation of MI intervals, and data referencing since we only validate the labeled trials, having removed artifacts provided by the database. Initially, for selecting the discriminant information of MI responses, each raw EEG channel $\boldsymbol{x}^c \in \mathbb{R}^T$ is sampled at 250 Hz (i.e., at sample rate Δt=0.004 s) and passed through a five-order bandpass Butterworth filter within Ω=[4, 40] Hz. Afterwards, the MI time window T_{MI}=2 s is segmented. Then, we deal with the volume conduction effect that produces a low signal-to-noise ratio of EEG data by applying the Laplacian spatial filter [122]. The preprocessing procedures are implemented using a tailor-made software in Phyton.

4.2 Parameter Tuning of Compared Entropy-based Estimators

Generally, every parameter influences the Entropy-based assessments of ERD/S, but contributing differently to two main aspects of performance: discriminability and physiological interpretability. A first decisive parameter is a short-time window that must be adjusted

to extract the EEG dynamics over time accurately [123]. Related to building the sample-based alphabets, we investigate the following values of τ reported in MI tasks [124, 125]: $\tau \in \{1, 1.5, 2\}$ s with 90% overlapping. Further, we explore the importance of the complexity parameters on building the embedded alphabets: threshold tolerance ρ, measuring the regularity of pattern similarity, and the embedding value M. In terms of distinguishing between different MI tasks, we assess the parameter contribution, employing the bi-class accuracy that is computed by the Linear Discriminant Analysis algorithm under a 10-fold validation strategy. Thus, to generate the embedded alphabets, both complexity parameters (ρ and M) are heuristically established to reach the best classification rate. To this end, we search within the interval of embedding dimension, $M = \{1, 2, 3\}$ and tolerance $\rho = \{0.05, 0.1, 0.2, 0.3, 0.4, 0.5, 0.6, 0.7, 0.8, 0.9\}$.

Table 4.1 displays the accuracy performed by every tested subject. Note that for interpretability purposes, the individuals are ranked in decreasing order of the performed accuracy to rate the BCI literacy. So, a previous MI study defined the BCI-literacy threshold at 70% [126]. In the following, this level will be marked with dashed lines on the plots. So, we rank all subjects by the accuracy achieved by *SampleEnt*, as follows: BO9T, BO8T, BO3T, BO1T, BO5T, BO6T, BO7T, BO2T, and BO4T.

Table 4.1: Influence of the short-time window on the bi-class classifier accuracy performed by each tested Entropy-based estimator. Notation * stands for the values of τ reaching the best accuracy of MI tasks. Note that individuals are ranked in decreasing order to rate the BCI literacy. The best individual scores are underlined while the best values performed between the estimators are marked in black.

#	***SampleEnt***			***FuzzyEnt***			***VQEnt***		
τ [s]	**2**	**1.5**	**1***	**2**	**1.5***	**1**	**2**	**1.5**	**1***
B09T	94.9±8.3	95.7±6.8	94.1±5.21	94.2±7.1	95.1±7.2	95.0±5.4	96.8±5.2	96.6±6.7	97.4±4.0
B08T	94.4±8.9	94.3±8.3	92.0±10.0	96.9±3.8	96.1±5.4	92.7±8.7	97.6±3.6	95.4±6.2	92.4±3.2
B03T	94.9±3.4	91.3±7.0	88.2±6.4	89.7±5.9	88.9±6.8	86.1±6.5	94.1±5.4	92.0±6.1	89.2±8.6
B01T	81.2±12.4	80.2±14.7	78.2±11.1	79.6±11.1	81.1±8.7	80.4±11.6	81.9±7.9	80.4±9.2	81.1±7.5
B05T	71.7±11.4	73.7±12.9	74.8±12.4	73.0±10.7	79.3±6.9	75.5±8.6	68.4±10.2	71.4±15.2	72.1±10.3
B06T	70.3±16.3	75.4±12.8	72.9±10.9	69.5±11.2	73.9±13.8	75.9±6.2	69.6±14.1	74.8±12.2	77.5±7.3
B07T	66.9±11.9	67.7±14.7	71.0±10.7	67.8±14.9	70.0±14.3	70.1±13.1	72.7±13.8	71.9±16.5	74±10.1
B02T	59.4±13.8	61.3±8.7	68.5±11.7	56.6±7.7	60.9±10.9	67.5±16.8	65.7±12.2	67.5±11.0	73.5±11
B04T	60.5±11.8	62.1±15.5	62.9±11.0	58.1±10.9	64.2±6.5	65.1±8.9	65.8±14.3	73.2±12.0	71.2±10.7
Mean	77.1±10.9	78.0±11.3	78.0±9.9	76.2±9.3	78.8±9.0	78.7±9.5	**79.2±9.7**	**80.4±10.6**	**80.9±8.1**

As seen, the value of τ=2 s provides the lowest accuracy regardless of the evaluated Entropy-based estimator. Though the statistical differences are not high to be significant between the small windows, the choice of the shortest window τ=1 s seems to be the best option since it gives the highest mean accuracy with lower dispersion. To strengthen this selection, we highlight the fact that five of the individuals reach the best performance in this window (see the underlined scores).

Besides, the comparison between estimators shows that *SampleEnt* and *FuzzyEnt* have similar accuracy, while *VQEnt* outperforms a bit with the benefit of supplying the lowest dispersion. Moreover, the majority of subjects perform the best result using the sample-based VQ Entropy.

Table 4.2: Tuning of complexity values, threshold tolerance ρ and embedding value M, performed at τ=1 s, fixing Q=250-M. Notation Q' stands for the reduced size of VQ alphabets.

	SampleEnt		***FuzzyEnt***		***VQEnt***		
#	***M***	***ρ***	***M***	***ρ***	***M***	***ρ***	***Q′***
B09T	2	0.9	2	0.3	2	0.3	83
B08T	1	0.9	1	0.3	3	0.6	47
B03T	3	0.9	3	0.6	2	0.1	116
B01T	1	0.8	1	0.2	2	0.2	86
B05T	1	0.8	3	0.6	2	0.1	110
B06T	3	0.9	1	0.9	2	0.6	47
B07T	1	0.5	1	0.6	3	0.9	32
B02T	2	0.8	1	0.05	2	0.3	72
B04T	2	0.6	1	0.5	3	0.9	30
Median	1	0.8	2	0.5	2	0.3	

For illustrating the parameter tuning, Table 4.2 displays the values fixed for each estimator to achieve the best individual classifier performance. In the case of quantized stochastic patterns, the value M=2 appears to be enough, while by adjusting $\rho\sim$0.3 leads to accurate estimates of accuracy. The impact of the investigated dynamics becomes evident from Figure 4.1 that illustrates the parameter variability for the proposed *VQEnt*. For better visualization, the tested subjects are split into three groups due to the differentiable behavior reported for their brain activity dynamics evoked in practicing MI tasks [127]. As widely-known, therefore, the optimal parameter setting depends on the complexity measured for each subject group.

4.3 Interpretability of Time-courses Estimated for - Event-Related De/Synchronization

To have a better understanding, Figure 4.2 presents the ERD/S time-series of the Entropy-based methods computed for the best individual of each group within the MI interval [2.5–4.5] s. All ERD/S time-courses are estimated for the representative sensorimotor channels (that is, C3 and C4) as a response to either performed MI task. For the sake of comparison, the top raw displays the corresponding ERD/S trajectories calculated by the variational percentage in EEG signal power, as described by Equation (2.6). In this case, each trajectory is averaged across the whole trial set, providing a resolution that is much bigger than the one resulted from the tested Entropy-based methods since $\Delta t \ll \tau$.

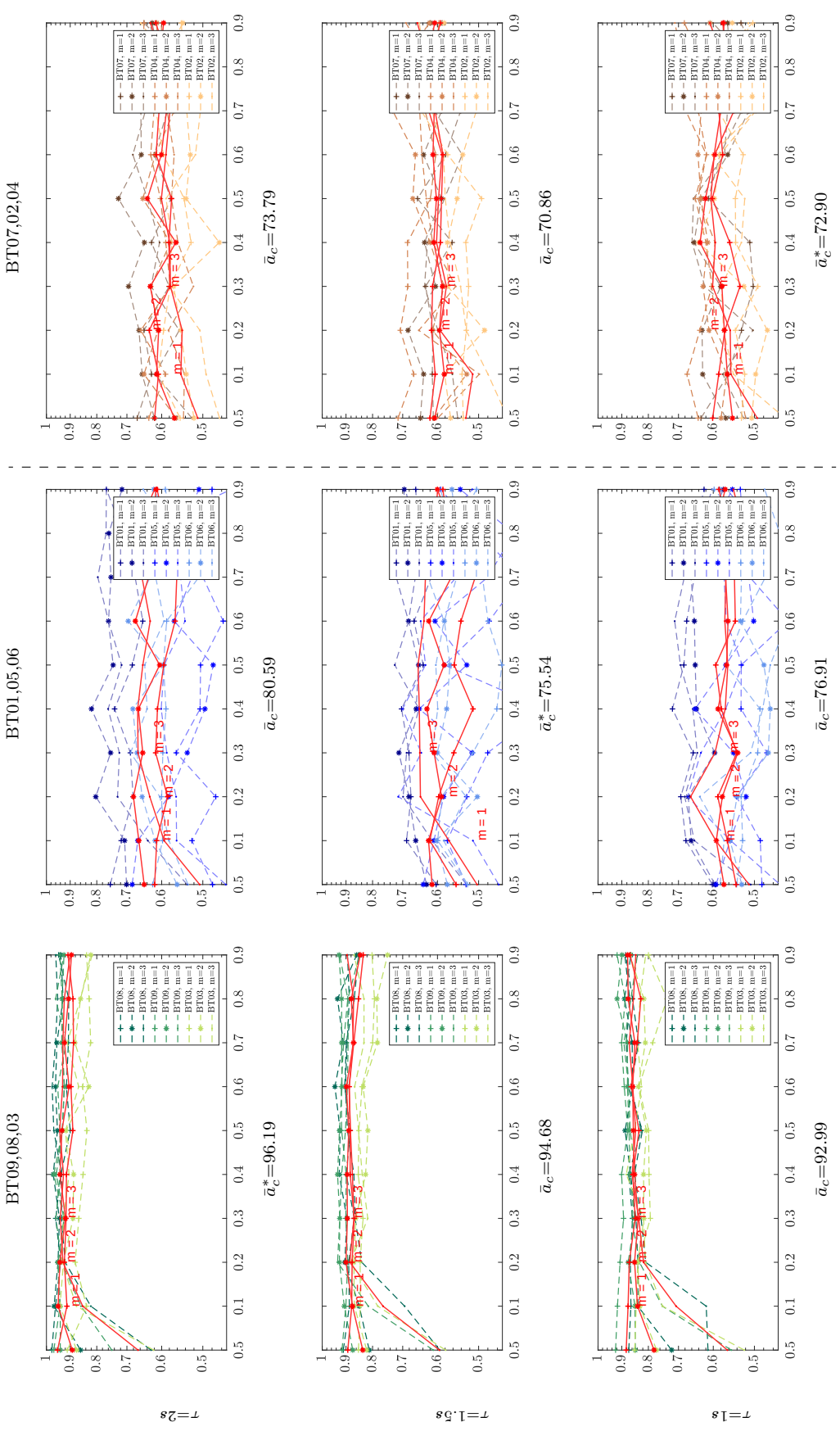

Figure 4.1: Performance variability depending on the individual parameter set-up of *VQ-En* estimator, accomplished at the examined windows τ. Presented values of accuracy $\bar{a}_c$ are averaged across the subjects belonging to each considered group.

For the right-hand task, the Entropy time-series of the contralateral electrode, C3, starts decreasing from the maximal value at a time sample close to 2s (after the cue onset) and reaches the lowest point at 3s. Further, the MI brain response begins increasing. As expected, the Entropy of electrode C4 behaves with the same pattern for the left-hand task, as detailed in [128]. At the same time, the time-courses of the ipsilateral electrode (C4 for the right hand, C3 – left-hand) holds high values over the MI interval. Therefore, the ERD/S patterns performed by each evaluated Entropy-based estimator fulfills the MI paradigm. That is, the ERD/s evolves more firmly on the electrodes located contralaterally to the hand involved in each task when a subject imagines the movement of its right/ left hand.

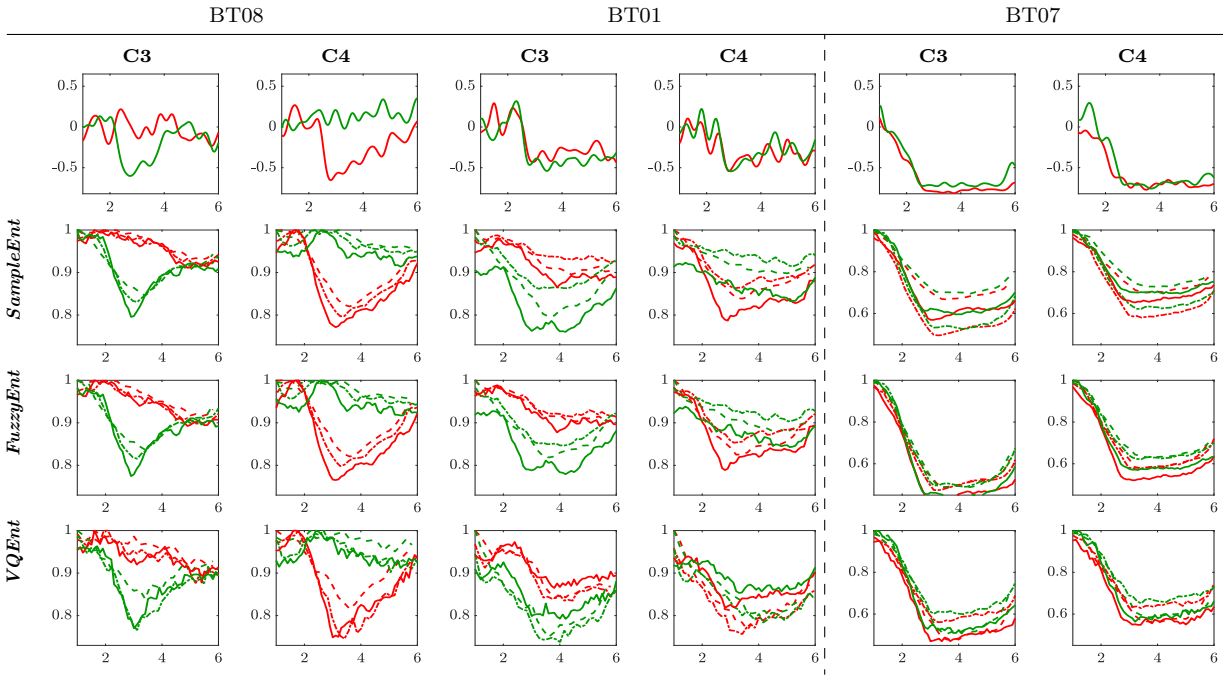

Figure 4.2: Individual ERD/S time-course of channels C3 and C4 performed by each tested Entropy-based estimator, averaging over all single trials for the right hand task (green color) and left hand (reed). Solid line τ=1 s, dash-dotted line τ=1.5 s, and dash line τ=2 s.

Nonetheless, the de/synchronization model is more evident for τ=1 (solid line), but the responses weaken and tend to be smoother as the time window elongates. Furthermore, the ability to learn MI tasks also influences: the higher the BCI literacy, the more evident the ERD/S patterns. While the subject B08T (performing the best) presents brain responses with marked differences between tasks, the time-series set of BT07 (achieving a very low classifier accuracy) is far from being a synchronization pattern within the trial timing. This finding follows some clinical studies, evidencing that BCI-illiterate subjects manifest a lack in event-related desynchronization, which is of keen importance to perform MI tasks satisfactorily [35].

On the other hand, the averaged time-courses seem to be similar at each validating set-up (i.e., by fixing the same time window and BCI literacy), and therefore, explaining the proximity of accuracy provided by the Entropy-based estimators. Still, there are subtle

differences between them. For investigating this aspect in more detail, the trial-wise relationship is calculated through the following distance of similarity [129]:

$$\mathrm{d}(n, n') = \exp\left(-||\mathbb{H}\left\{X_{nm}(\cdot,\cdot);\cdot\right\} - \mathbb{H}\left\{X_{n'm'}(\cdot,\cdot);\cdot\right\}||_2^2/\sigma_X^2\right), \forall n, n' \in N,$$

where σ_X is the variance averaged across the trial set for each validated Entropy-based estimator $m, m' \in \{SampEnt,\ FuzzyEnt,\ VQEnt\}$.

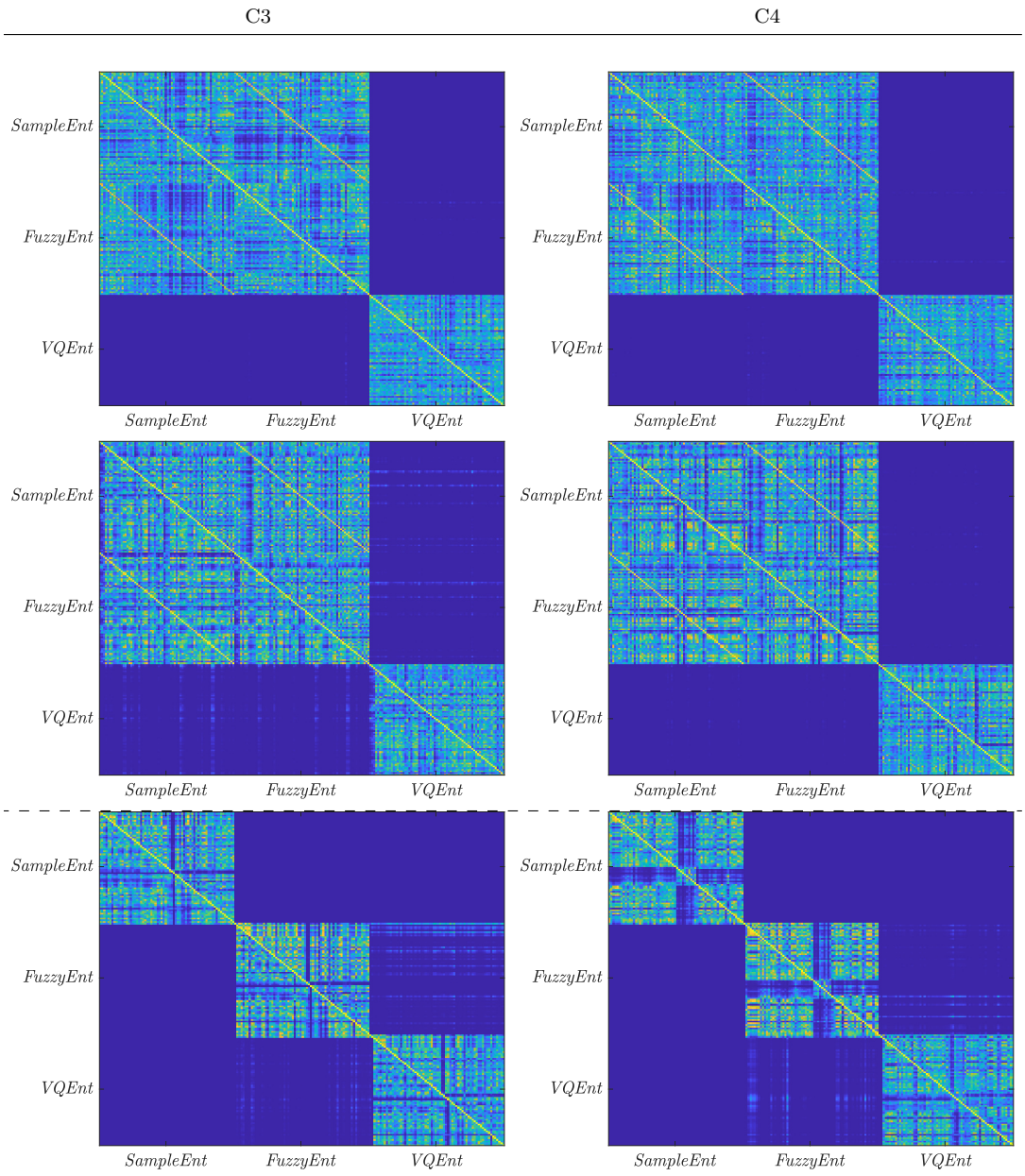

Figure 4.3: Asymmetric connection matrix of similarity between *SampEnt*, *FuzzyEnt*, and *VQEnt* performed by subjects with different rate of BCI literacy, and estimated across all trial set at τ=1 s. All entries above the main diagonal reflect the right label, while the lower triangular is for left label.

In the case of subjects with average rates of BCI literacy over 70%, the top and middle rows of Figure 4.3 display the connection matrix of similarity, calculated at τ=1 s, showing that the MI brain response of *SampEnt* and *FuzzyEnt* algorithms are very close in shape. However, the ERD/S time-courses performed by *VQEnt* differs from other estimators in all cases of τ. Otherwise, each Entropy-based method becomes more separate from others, as depicted in the button row for BT07 with BCI illiteracy. In terms of the performed MI tasks, the lower and upper triangular parts of the connectivity matrix hold very subtle distinctions in each one of representative channels (C3 and C4) and regardless of the employed Entropy-based estimator.

4.4 Statistical Analysis

Intending to evaluate the contrasted methods, we perform the non-parametric permutation test commonly used in evaluating different effect types of evoked responses in EEG applications [130]. To estimate the p-value, the Monte-Carlo permutation partitions are chosen by clustering of all adjacent time-samples that exhibit a similar difference. In each subject-based permutation, we cluster the spatial and temporal adjacency across the trial set, for a fixed value of $p < 0.02$. Figure 4.4 depicts the obtained topographical plot of two representative individuals (literate subject B08T and illiterate B01T), showing the channels that hold discriminant information in performing the MI task, which are computed within five non-overlapped time windows of interest: before task ([0.5–1.5] s), during MI task ([2.5–3.5] s and [3.5–4.5] s) and at the trial timing end ([4.5–5.5] s and [5.5–6.5] s).

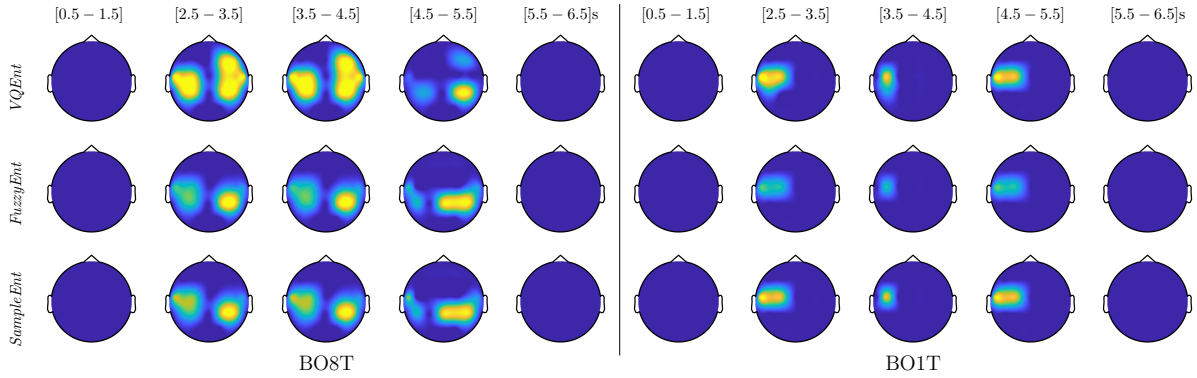

Figure 4.4: Statistical analysis of two representative individuals (literate subject B08T and illiterate B01T), showing the channels that hold discriminant information in performing the MI task.

As expected, there is no information about the MI task in the interval before the stimulus. Instead, discriminant information is mostly localized within both MI segments, but the estimates have very changing behavior in [4.5–5.5] s. Note that the discriminate information fades at the trial timing end when either subject is performing a break. In the case of B08T, the discriminating activity involves the Centro-lateral primary motor area, supplementary motor area, frontoparietal, and primary somatosensory area, that is,

the regions typical in hand MI practicing [111]. B01T shows a weak contribution in those areas also, but excluding the critical frontoparietal region [73].

4.5 Contribution of Sensorimotor Area to Distinguishing Between MI Tasks

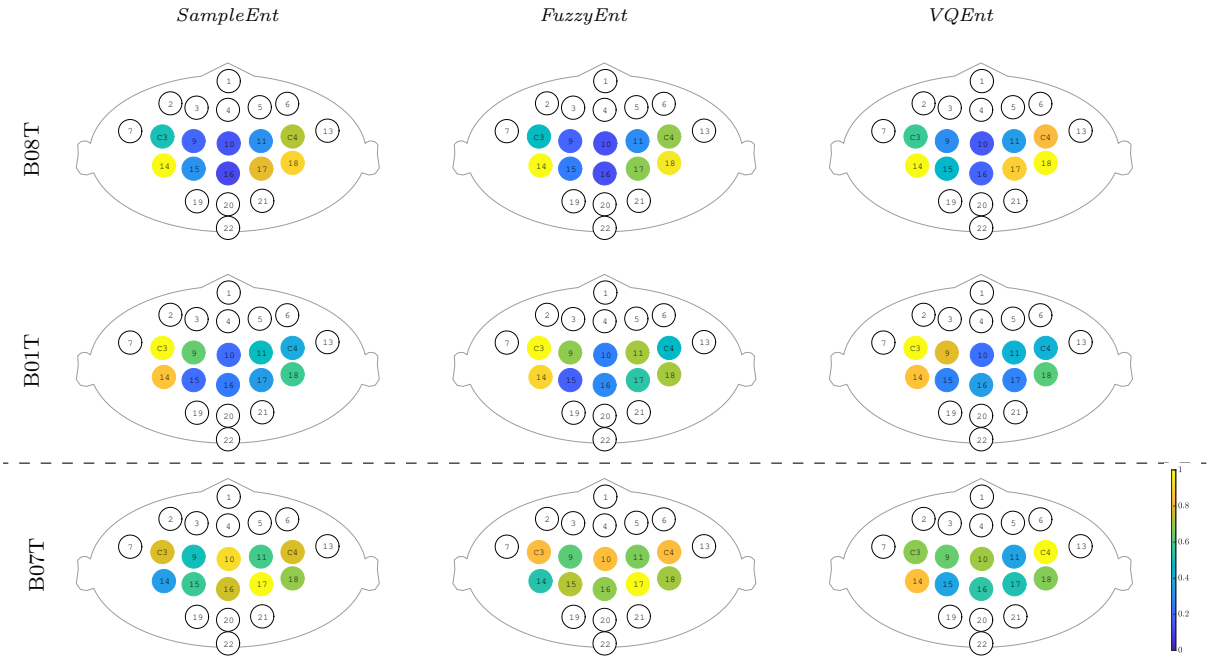

Figure 4.5: Sensorimotor electrode contribution in classifying MI tasks estimated through Entropy-based ERD/S time-series. Relevance weights of uncolored electrodes are not considered.

Figure 4.5 displays the relevance of each sensorimotor channel that is computed as the Euclidean distance between the activities of labeled trials [131]. As seen in the top row, BT08 has high values of relevance in channels C3 and 18 (left hemisphere), as well as in C3 and 14 (right hemisphere), meaning that both regions contribute alike. At the same time, either channel belonging to the longitudinal fissure area produces a little contribution. The relevance sets provided by all Entropy-based estimators are very similar and agree with the MI paradigm. Nonetheless, the C3 electrode is weaker than the 14 one (left hemisphere). Figure 4.6 displays the time-courses of *VQEnt*-based ERD/S, showing the differences in IM responses between the ipsilateral channels. As seen, electrode 14 is more potent than the representative C3, while electrode 18 is more potent than C4. This situation can be explained because of the volume conduction effect of EEG signals, which hold a low spatial resolution, and thus, lead to inaccurate measures of brain activity [132]. In the case of B01T, the assessed relevance set is comparable to those obtained by BT08, as shown in the middle row. However, the contribution from the left-hemisphere channels

(C3 and 14) is higher than provided by the right hemisphere (C4 and 18), suggesting a right-hand dominance [133].

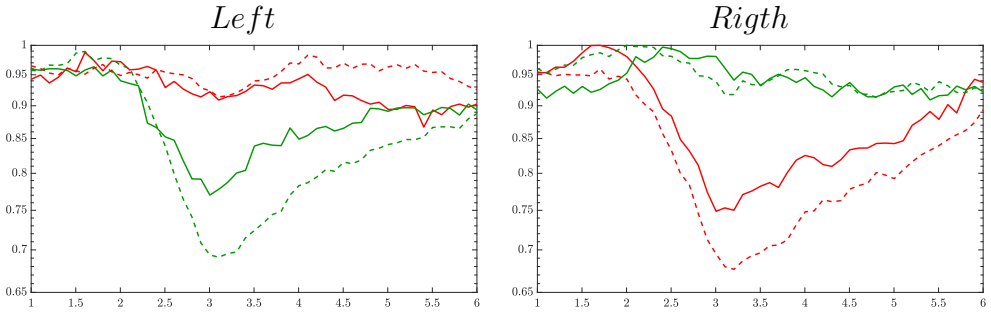

Figure 4.6: Detailed illustration of estimated ERD/S time-series: C3 vs ch14(dashed line), and C4 vs ch18(dashed line).

Using the estimated Entropy-based ERD/S time-series, we investigate the increased activity of the sensorimotor area that is related to the motor imagery paradigm, assessing the electrode contribution (or relevance) in terms of distinguishing between the labels. Namely, the following channels are considered: left hemisphere (C3, 9, 14, and 15), right hemisphere (C4, 11, 18, and 17), as well as the longitudinal fissure area (10, 16).

In the case of BT07, the relevance set redistributes across the whole sensorimotor area, increasing in value at each electrode. Moreover, the contribution of longitudinal fissure area starts growing, though these electrodes are assumed to have very modest participation in motor imagery activation. Thus, this subject with low performance shows fewer prominent features than those who perform better, as already has been reported in similar cases [108].

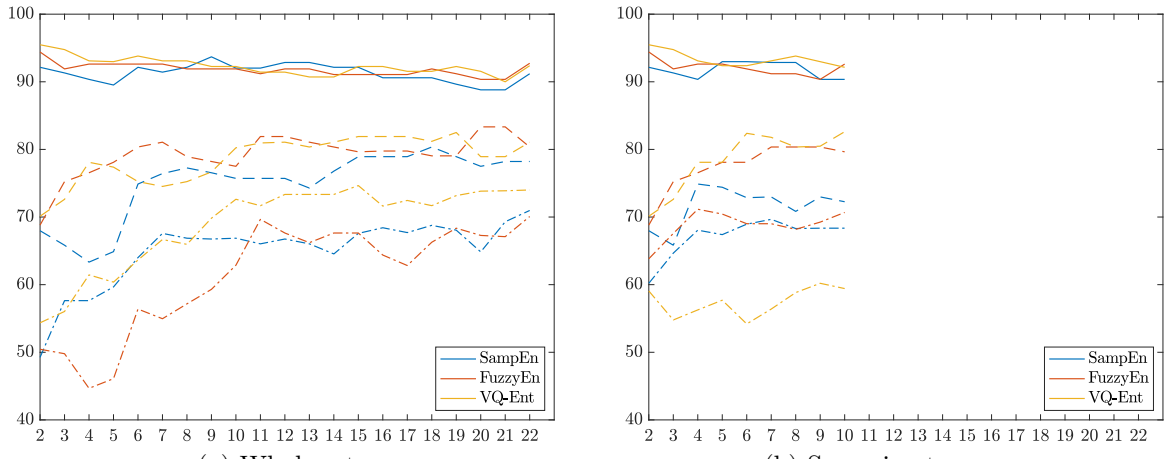

(a) Whole set (b) Sensorimotor area

Figure 4.7: Classifier performance of subjects achieved by feeding each channel ranked by relevance. (a) Entropy-based relevance computed for all electrodes. (b) Entropy-based relevance of the sensorimotor electrodes.

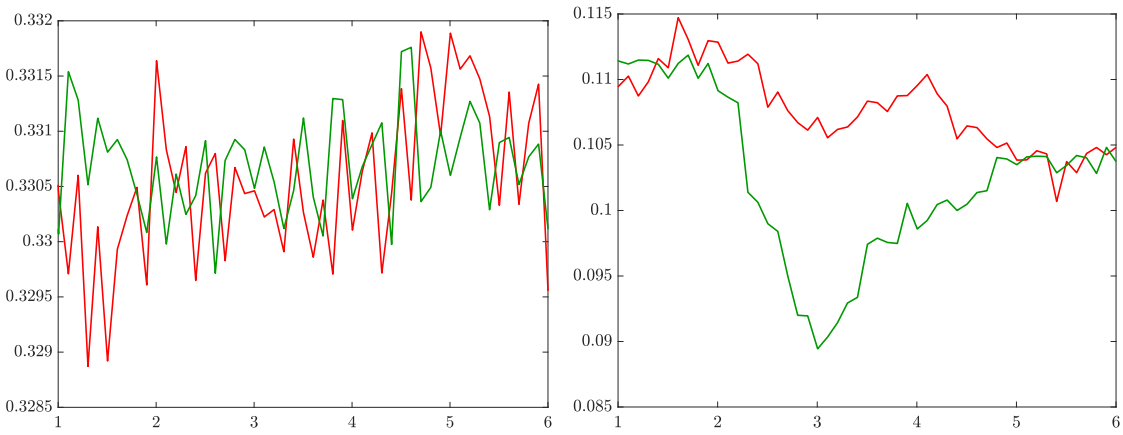

(a) Before Spatial filte (b) After Spatial filter

Figure 4.8: Example of Laplacian filtering to reduce the volume conduction effect on Entropy estimation.

One more aspect to consider is the resulting accuracy due to the assessed electrode contribution after using the estimated Entropy-based ERD/S time-courses. In this regard, two different scenarios are considered: a) Addition of the whole EEG channel set, b) Incorporation of just the sensorimotor channels. In either case, training is conducted by adding every channel ranked in decreasing order of relevance. As displayed inFigure Fig. 4.7a, the individuals B01T and B08T deliver high values of accuracy. Moreover, in both cases, the *VQEnt* estimator presents the most accurate outcomes at a lower amount of electrodes. A similar situation takes place with the individual B07T, for which our proposed method remarkably increases the accuracy in comparison to the other tested Entropy estimators. In the latter scenario, Figure Fig. 4.7b reveals that the reduced channel set directly involved with the MI paradigm is enough to discriminate between tasks, providing an accuracy similar to the performed by the whole electrode set.

Nevertheless, though the *VQEnt* estimator allows enhancing the performance of the best literate subjects, our proposal fails in the case of B07T. One factor that may account for this result is the volume conduction effect since it also may affect the Entropy-based estimators, as referred in [134]. A detailed analysis of the relevance performed in the all-channel scenario shows that this individual redistributes his values all over the excluded neighboring frontal area.

Another point to highlight is the influence of noise on the entropy calculation. Specifically, to address the volume conduction problem, we perform a Laplacian filter that improves the spatial resolution of EEG recordings, avoiding the influence of noise from neighboring channels [135]. Figure 4.8 shows the cases of the entropy computation of channel C3 with (and without) spatial filtration. As seen, the entropy calculated from the raw data (left) does not present any de/synchronization related to elicited neural responses regardless of the tasks (left hand / right hand). Instead, the Laplacian filter reduces the effect of noise coming from neighboring channels, making clear the changes related to the stimulation of motor imagination.

4.6 Discussion

The proposed method is sample-based and builds the probabilistic priors by assessing the Gaussian similarity between the input EEG measurements and their reduced vector-quantized representation. Nevertheless, the following aspects are to be considered:

Parameter tuning of Entropy estimators: A first decisive parameter is a short-time window that must be adjusted to extract the dynamics over time from MI data accurately. The value τ=1 is fixed that gives the highest mean accuracy with lower dispersion, providing similar performance for all tested Entropy-based estimators. This choice is reported to be generally appropriate for most time-series that have dynamics with rapidly decaying autocorrelation function.

Besides, we explore the influence of complexity parameters (threshold tolerance ρ and embedding value M) on building the embedded alphabets. According to the complexity values fixed to achieve the best classifier performance of each individual, *SampEnt* and *FuzzyEnt* demand symbols with more elements to encode more precise the rapid dynamics because of the relatively small value tuned for τ=1. However, for dynamic systems that have long-range correlation, the choice of different delays can have a significant impact on the calculation of Sample-based algorithms, leading to inconsistencies in the pairwise evaluation of the relative complexity between time-series, as discussed in [136]. As a result, the similarity pattern count calculation in Eq. (2.11) will necessitate more statistics, which are supplied with the trial set. Instead, to encode dynamics, *VQEnt* relies on a quantized version that yields alphabets with a high compression ratio, and therefore, requiring symbols with more extensive representations (M=2, 3). In other words, each symbol encodes not one, but several neighboring samples.

Furthermore, the fact that *VQEnt* alphabets have a high compression ratio avoids a significant impact of noise on the time-series, and it reduces in complexity the choice of ρ. In contrast, the fuzzy and sample methods tend to be more susceptible to the noise effect, resulting in larger values of ρ. Overall, the parameter tuning of Entropy estimators depends on the BCI literacy rate. Of note, we test three Entropy-based methods that have as a significant advantage that they do not need any reference power value, which is far from being easy to adjust while highly influences the ERD/S estimation.compression ratio, and therefore, requiring symbols with more extensive representations (M=2, 3). In other words, each symbol encodes not one, but several neighboring samples.

Interpretability of estimated ERD/S time-series: Generally, the ERD/S dynamics, performed by each considered Entropy-based estimators, fulfills the experimental paradigm of practiced MI tasks. However, due to inherent nonstationarity and a poor signal-to-noise ratio of EEG signals, location and amplitudes of brain activity sources have substantial variability in patterns across trials. For understanding the causes of inter- and intra-subject variability in performance, the database subjects split into groups with the differentiable behavior of brain dynamics in MI tasks. As a pivotal parameter, the short-time window is fixed to τ=1 to achieve a higher classifier accuracy. The first finding is that the complexity parameters that quantify the EEG data dynamics vary for each subject group, resulting in a differentiated optimal parameter setting. Moreover, the ability to learn MI tasks also influences, meaning that the higher the BCI literacy, the more consistent the ERD/S patterns of motor imagery. Besides, the connection matrix of similarity confirms

that the ERD/S time-series performed by *VQEnt* are different in shape from the ones build by *SampEnt* and *FuzzyEnt* algorithms.

Activation of the sensorimotor cortex during motor imagery: We assess the contribution to distinguish between MI labels and prove that the relevance sets, provided by the left and right hemispheres, are similar despite the estimated Entropy-based ERD/S time-series. However, in individuals with the illiteracy rate, the relevance set spreads and increases abnormally across the whole sensorimotor area. As a result, literate individuals deliver high values of accuracy. Moreover, the *VQEnt* estimator presents the most accurate outcomes at a lower amount of electrodes so that reduced channel set directly involved with the MI paradigm is enough to discriminate between tasks, providing an accuracy similar to the performed by the whole electrode set.

Nonetheless, some issues remain to improve the effectiveness of the developed *VQEnt* approach for the estimation of ERD/S. Firstly, the extraction of VQ alphabets should be improved, by instance, using more elaborate distances for their construction. Moreover, it would be of benefit to incorporate other types of stochastic embedding to relax the parameter tuning of the used complexity representations. However, by increasing efficiency of the extracted symbols, the computational burden must also be examined. So far, the implementing cost of *VQEnt* exceeds more than 50% other sample-based algorithms. Also, the concept of illiteracy faces several pitfalls in BCI research so that alternative criteria should be considered [137].

Parameter tuning of Entropy estimators: A first decisive parameter is a short-time window that must be adjusted to extract the dynamics over time from MI data accurately. The value τ=1 is fixed that gives the highest mean accuracy with lower dispersion, providing similar performance for all tested Entropy-based estimators. This choice is reported to be generally appropriate for most time-series that have dynamics with rapidly decaying autocorrelation function.

Besides, we explore the influence of complexity parameters (threshold tolerance ρ and embedding value M) on building the embedded alphabets. According to the complexity values fixed to achieve the best classifier performance of each individual, *SampEnt* and *FuzzyEnt* demand symbols with more elements to encode more precise the rapid dynamics because of the relatively small value tuned for τ=1. However, for dynamic systems that have long-range correlation, the choice of different delays can have a significant impact on the calculation of Sample-based algorithms, leading to inconsistencies in the pairwise evaluation of the relative complexity between time-series, as discussed in [136]. As a result, the similarity pattern count calculation in Eq. (2.11) will necessitate more statistics, which are supplied with the trial set. Instead, to encode dynamics, *VQEnt* relies on a quantized version that yields alphabets with a high compression ratio, and therefore, requiring symbols with more extensive representations (M=2, 3). In other words, each symbol encodes not one, but several neighboring samples.

Furthermore, the fact that *VQEnt* alphabets have a high compression ratio avoids a significant impact of noise on the time-series, and it reduces in complexity the choice of ρ. In contrast, the fuzzy and sample methods tend to be more susceptible to the noise effect, resulting in larger values of ρ. Overall, the parameter tuning of Entropy estimators depends on the BCI literacy rate. Of note, we test three Entropy-based methods that have as a significant advantage that they do not need any reference power value, which is

far from being easy to adjust while highly influences the ERD/S estimation.compression ratio, and therefore, requiring symbols with more extensive representations (M=2, 3). In other words, each symbol encodes not one, but several neighboring samples.

Interpretability of estimated ERD/S time-series: Generally, the ERD/S dynamics, performed by each considered Entropy-based estimators, fulfills the experimental paradigm of practiced MI tasks. However, due to inherent nonstationarity and a poor signal-to-noise ratio of EEG signals, location and amplitudes of brain activity sources have substantial variability in patterns across trials. For understanding the causes of inter- and intra-subject variability in performance, the database subjects split into groups with the differentiable behavior of brain dynamics in MI tasks. As a pivotal parameter, the short-time window is fixed to τ=1 to achieve a higher classifier accuracy. The first finding is that the complexity parameters that quantify the EEG data dynamics vary for each subject group, resulting in a differentiated optimal parameter setting. Moreover, the ability to learn MI tasks also influences, meaning that the higher the BCI literacy, the more consistent the ERD/S patterns of motor imagery. Besides, the connection matrix of similarity confirms that the ERD/S time-series performed by *VQEnt* are different in shape from the ones build by *SampEnt* and *FuzzyEnt* algorithms.

Activation of the sensorimotor cortex during motor imagery: We assess the contribution to distinguish between MI labels and prove that the relevance sets, provided by the left and right hemispheres, are similar despite the estimated Entropy-based ERD/S time-series. However, in individuals with the illiteracy rate, the relevance set spreads and increases abnormally across the whole sensorimotor area. As a result, literate individuals deliver high values of accuracy. Moreover, the *VQEnt* estimator presents the most accurate outcomes at a lower amount of electrodes so that reduced channel set directly involved with the MI paradigm is enough to discriminate between tasks, providing an accuracy similar to the performed by the whole electrode set.

Nonetheless, some issues remain to improve the effectiveness of the developed *VQEnt* approach for the estimation of ERD/S. Firstly, the extraction of VQ alphabets should be improved, by instance, using more elaborate distances for their construction. Moreover, it would be of benefit to incorporate other types of stochastic embedding to relax the parameter tuning of the used complexity representations. However, by increasing efficiency of the extracted symbols, the computational burden must also be examined. So far, the implementing cost of *VQEnt* exceeds more than 50% other sample-based algorithms. Also, the concept of illiteracy faces several pitfalls in BCI research so that alternative criteria should be considered [137].

Chapter 5

Experiments and Results of Intra-subject Neural Response Variability

5.1 Experiments and Results of Multi-subject Dynamic Models

Validation of the proposed approach for common-dynamics modeling of brain neural activity comprises three stages (see the pipeline in Fig. 5.1): *i*) Decomposition of input EEG time-series into a frequency-specific temporal representation; *ii*) Subject-level feature extraction of *t-f* dynamics, encoding the electrode contribution (explained in Section 2.1), *iii*) Extraction of multi-subject *t-f* dynamics. We performed the pairwise distance between individuals on the subject-level and group-level stages during the evaluation. Also, visual inspection of the obtained extracted *t-f* dynamics is presented, stressing on the physiological interpretability of results. All the experiments were perfomed form datasets DI and DII described in Section 2.3.

5.1.1 Parameter Set-up

We compute the collective task-related dynamics extracted from the *t-f* feature patterns $\{\boldsymbol{\theta}_{\eta}^{(m)}(f,\tau|\lambda){:}\forall f{\in}\Omega,\tau{\in}N_{\tau}\}$ with $\eta{=}\{J,\zeta,\phi\}$ using a time-window length, fixed for each extraction method differently. Namely, $\tau_{J}{=}1s$, $\tau_{\phi}{=}0.1s$, and $\tau_{\zeta}{=}0.004s$, resulting in the following volumes of time samples: $J{\rightarrow}N_{\tau}{=}60$, $\phi{\rightarrow}N_{\tau}{=}66$, $\zeta{\rightarrow}N_{\tau}{=}1751$. Then, we assess the similarity of each accomplished model of collective dynamics with the corresponding subject-level dynamics. However, for interpretability purposes, the similarity measure is computed just over the primary motor area as the most representative in motor imagery tasks [138].

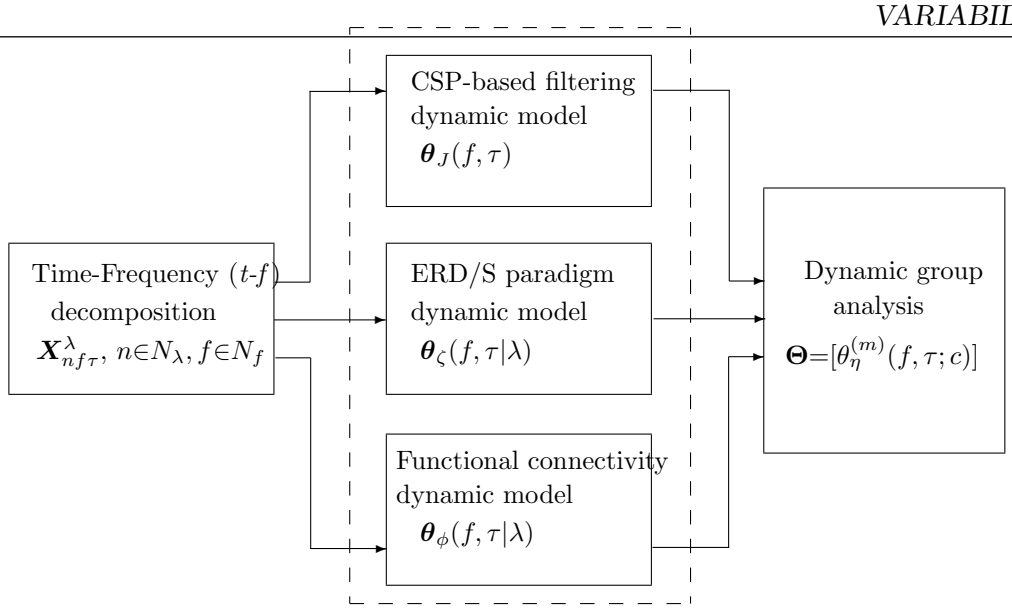

Figure 5.1: Scheme illustrating the stages of common dynamic modeling proposed for brain neural activity in motor imagery tasks. The evaluated t-f feature extraction methods are contained in the dashed box.

5.1.2 Clustering of Subject-Level Efficiency

To manage the significant impact of inter-subject variability on the reached accuracy, we employ a neurophysiological predictor of BCI performance to divide the evaluated subjects into two clustered assemblies: BCI-literacy, or users with the ability to produce reliable and reasonably robust differences in neural activity between distinct MI tasks (e.g., left-hand vs. right-hand) [108], and BCI-illiteracy, or individuals who are not accurate enough to control the MI application.

As suggested in [1], we cluster the entire subject set into two mutually exclusive assemblies by removing points of the sample that have the 10% largest Malahanobis distance to the data center. For each tested database, Fig. 5.2 presents the obtained scatter plots using the neurophysiological predictor. As input data, the average values of the mean and standard deviation are computed for each case of τ_J. To clarify the clustering results, we rank the subject set in decreasing order of the average discrimination accuracy in Fig. 3.1a (D-I) and Fig. 3.1b (D-II), where a dashed vertical line separates both assessed assemblies, displaying the individual performance estimated at different window lengths. As a result, the D-I collection holds five BCI-literacy subjects and four BCI-illiterate. In turn, D-II contains 15 BCI-literacy subjects, and the remaining 35 are BCI-illiterate.

5.1.3 Results of CSP-based Multi-subject Model

The topographic representation in Fig. 5.3 shows that the CSP-based multi-subject model does not vary remarkably along with μ and β oscillations, within the MI interval ΔT_3. Although the RQ relation resumes the influence of both labels into a single value, the neural activation is reflected over the primary motor and parietal areas, which should be strongly activated in MI tasks.

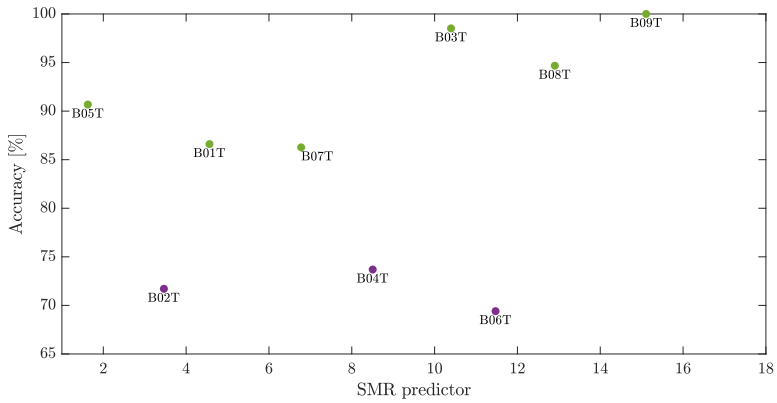

(a) D-I

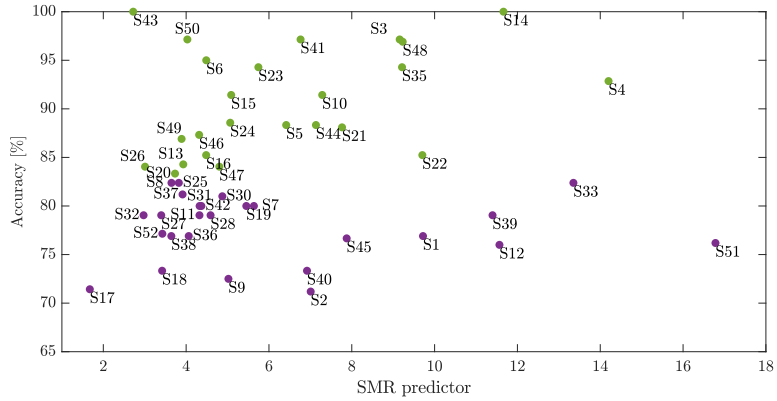

(b) D-II

Figure 5.2: Division into BCI-literacy and BCI-illiteracy. Scatter plots performed by the neurophysiological predictor for each database.

In the case of the Rayleigh Quotient, the topographic representation shows that the multi-subject model of extracted CSP dynamics for dataset D-I changes remarkably along with μ and β oscillations, within the MI interval ΔT_3, as seen in Fig. 5.5. Also, neural activation is reflected in the primary motor and parietal areas, which should be strongly activated in MI tasks. For database D-II, the contribution is placed in the sensorimotor area too, but the β oscillation influences the most.

5.1.4 Results of Functional Connectivity based Multi-subject Model

The calculated topograms of the common functional connectivity dynamics (see top row in Fig. 5.4) reveal perceptible differences between tasks. Fig. 5.4 (second row) shows the influence of stepwise removing the subjects with lower accuracy from the performed group analysis. As observed, the multi-subject model of DI (see the second row) changes significantly, meaning that the RQ time-series does not preserve enough the observed relationship between the subject-level dynamics (see the bandwidths [16-20] and β). This finding can be better understood in the third row, which displays the scatter plots of

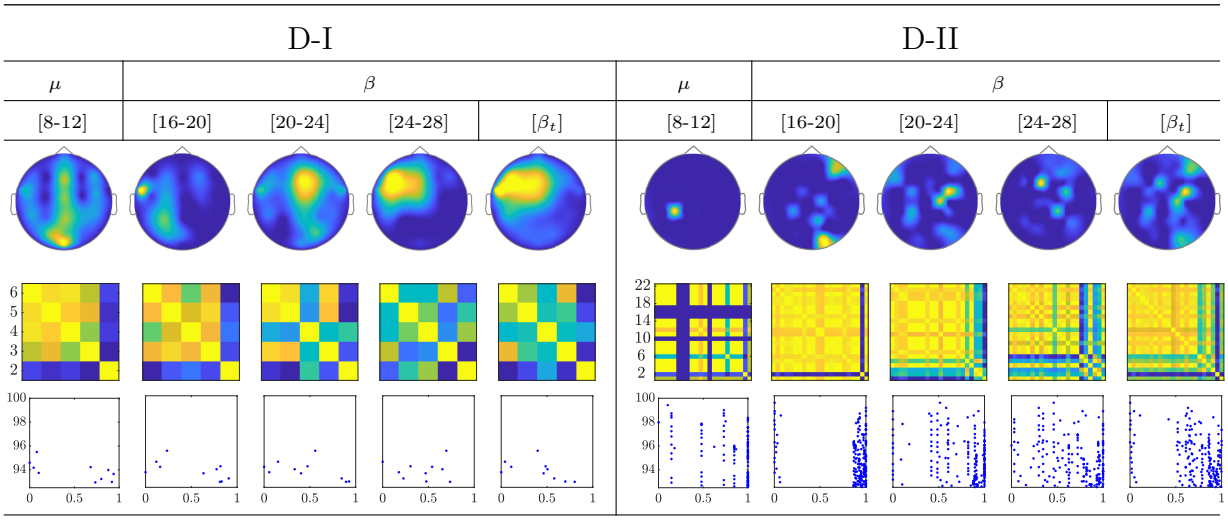

Figure 5.3: Common neural dynamics of Rayleigh Quotient, estimated over the subject set within the MI interval ΔT_3. *a*) Topographic *t-f* representation of multi-subject model. *b*) Pairwise distances estimated by desegregating individuals from the multi-subject model. *c*) scatter plot of normalied distances values of assessed group dynamics.

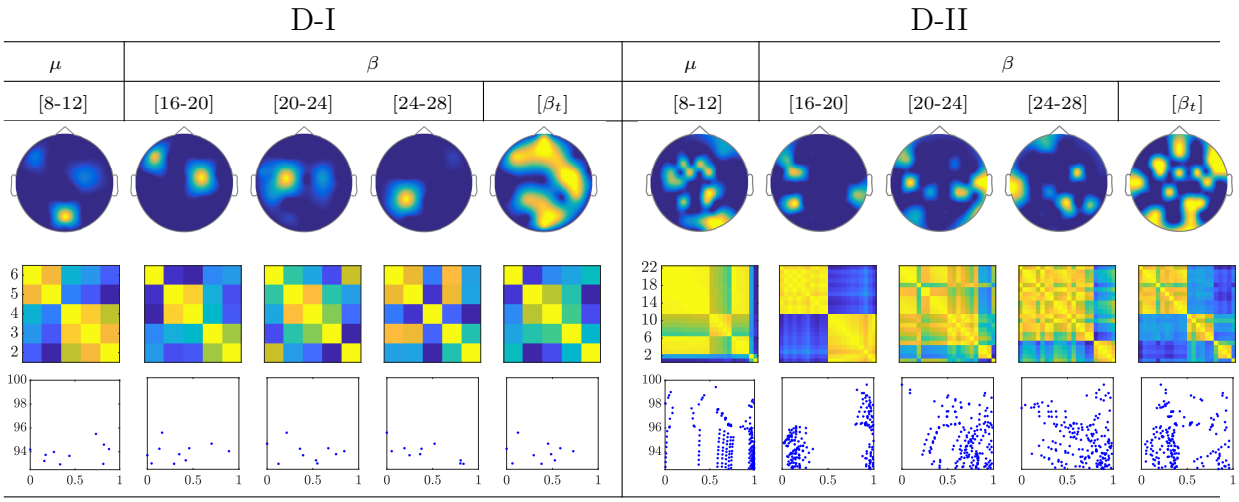

Figure 5.4: Common neural dynamics of Functional connectivity, estimated over the subject set within the MI interval ΔT_3. *a*) Topographic *t-f* representation of multi-subject model. *b*) Pairwise distances estimated by desegregating individuals from the multi-subject model. *c*) scatter plot of normalized distances values of assessed group dynamics.

the performed similarity measure estimated for the resulting groups. Several reasons may account for this result: the low number of subjects, the low resolution of EEG montage, and the high heterogeneity between their dynamics, as previously reported. In the case of DII, the procedure of the subject's removal reveals that their influence gathers into several groups depending on the spectral bandwidth.

5.1.5 Results of Event-related De/Synchronization based Multi-subject Model

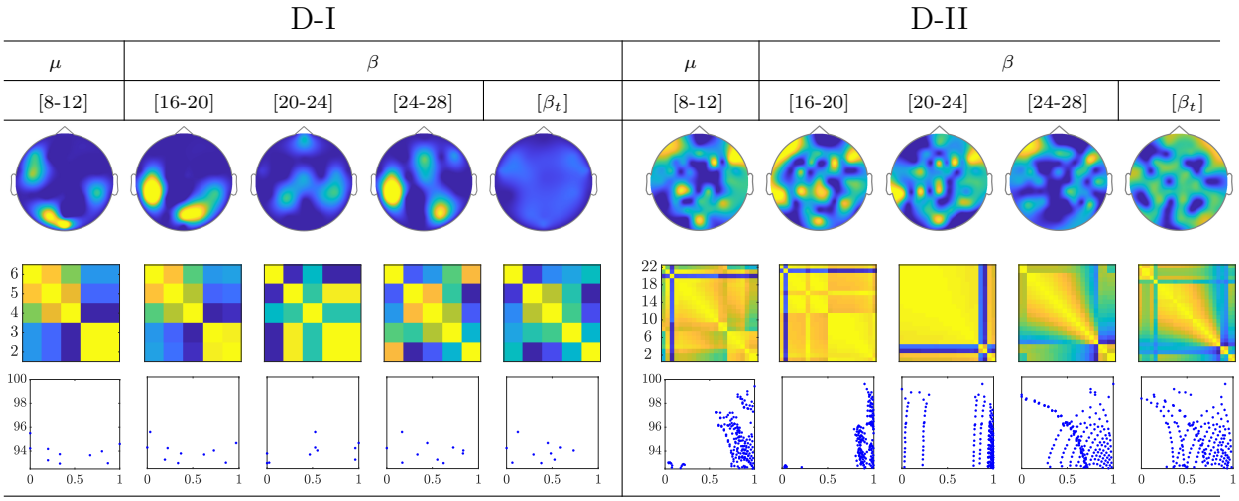

Figure 5.5: Common neural dynamics of Event-related De/Synchronization, estimated over the subject set within the MI interval ΔT_3. *a*) Topographic *t-f* representation of multi-subject model. *b*) Pairwise distances estimated by desegregating individuals from the multi-subject model. *c*) scatter plot of normalied similarities values of assessed group dynamics.

For the multi-subject models of ERD/S-based dynamics, the topograms of both datasets in Fig. 5.5 show a relevant contribution that is located in the primary motor area, supplementary motor cortex, and parietal cortex. These facts may have a physiological interpretation related to MI practice. Thus, channels present a notable neural activity through the considered frequencies, excluding the highest bandwidth [20-24] and [24-28] *Hz*.

Extracted from the ERD/S-based dynamics, the applied inter-subject similarity measure allows identifying the presence of subgroups very accurately, having a close resemblance between their produced neural connectivity patterns (see second-row of Fig. 5.5). Thus, the subjects with the highest accuracy gather the first subdivision, while those with lower accuracy are the last ones. Moreover, the scatter plots (third row) make evident of subgroups for the bandwidths [8-12], [16-20], and [20-24] *Hz* for bot datasets. Therefore, the multi-subject performed by ERD/S-based dynamics are effective in reducing subject aggregation. Thus, the group-level model preserves the main properties of similarity, even after removing subjects with lower accuracy in discriminating between MI tasks. However, the efficiency depends on the frequency bandwidth.

5.1.6 Discussion

Here, we develop a dynamic model for estimating the common neural activity across subjects to provide new insights into the evolution of collective mental imagery processes. After the preprocessing stage, the *t-f* EEG signal set is fed into a feature extraction

algorithm to improve the efficiency of triggering activity representation. Then, we employ a statistical thresholding algorithm to extract a multi-subject model that provides a set of confident estimates contributing the most to discriminating between MI tasks. We compare three feature extraction methods for making group inferences from subject-level dynamic information of neural activity. The obtained validation results indicate that the estimated collective dynamics reflect the flow in sensorimotor cortex activation differently. Therefore, the common model addresses inter-subject and inter-trial variability sources individually, depending on the engaged extraction method.

The developed group dynamic model can be considered a valid approach to infer the main properties of multi-subject datasets; however, the following remarks should be highlighted.

The multi-subject model enables inferring collective task-related dynamics from extracted subject-level feature sets. For better interpret the results, we evaluate the effectiveness of gathering data from collective sources by introducing two assumptions: *i*) a nonlinear assessment of the similarity between multi-subject data originating subject-level dynamics, instead of the widely used correlation index, as in [129]. *ii*) an assessment of brain network development though the ranking of subject accuracy in performing the MI task classification. As a result, the presented dynamic common model proves the ability to preserve the spatial distribution of brain neural activity throughout time and spectral domains, obtained from each one of the single-subject models. The attained multi-subject model allows spatial patterns that accommodate essential individual differences in sources.

However, some issues affect the ability to collect latent structures from sources. The employed collective framework extracts the latent components consistently expressed in the population, implying that they perform under the same conditions. In practice, this premise seems to be far from being right. Thus, several subjects systematically complete the MI tasks in the wrong way, misleading the group analysis. Hence, due to differences in individual MI literacy, the intra-subject heterogeneity reduces the estimated multi-subject models considerably. To illustrate, the presence of ERD/S mechanisms activated at the ipsilateral electrode in several subjects results in incorrect estimated values of hemisphere contribution. Thus, the subject triad performing the worst (probably, with modest motor imagery abilities) should be aggregated in a different group.

Besides, the employed latent component decomposition is unsupervised, and one might be interested in extracting the most discriminating dynamics to avoid the influence of some background neural activity. One more concern is the raised computational burden related to the *t-f* dynamic modeling, reducing to a small number of analyzed subjects.

5.2 Experiments and Results of Regression Analysis between Classifier Performance and Electrophysiological Indicators

Related to MI tasks, the methodology for evaluating the efficiency of neurophysiological indicators was performed using dataset D-II described in Section 2.3 and embraced the following stages: (*i*) extraction of a pre-training learning ability indicator, evaluating two

scenarios of resting data for computation: (a) baseline inverval, ΔT_1, lasting τ= 1.5 s; and (b) resting-state, lasting τ=55 s. (ii) Extraction of an initial training phase indicator from the Motor Imagery interval of the trial timing, (iii) regression and further clustering analysis between each electrophysiological indicator and the performance response of individuals. To this end, the accuracy classifier is estimated using the CSP-based features, maximizing the class variance to improve the system accuracy. Additionally, Spearman's correlation coefficient is used to assess the effectiveness of each electrophysiological indicator considered in predicting the bi-class accuracy response.

5.2.1 Preprocessing of EEG signals

Every raw EEG channel was band-pass filtered within the frequency range $\boldsymbol{f} \in$ [4-40] Hz, covering both considered sensorimotor rhythms, μ and β. With the aim of providing a physiological interpretation of the implemented experimental paradigm, the MI dynamics pictured in Figure Figure 2.2 are segmented. For purposes of evaluation, we employ the following two intervals of interest: ΔT_1=[0-2] s (termed baseline interval) and ΔT_2=[2.6-4.6] s (motor imagery interval). We only employ two intervals of interest during evaluation: ΔT_1, which contains the baseline interval, and ΔT_2, which reflects the most representative brain neural response. The length of either interval is selected to be comparable to the values that were reported for similar MI databases, like in [1]. Furthermore, for addressing the volume conduction problem, the indicators are assessed after performing the Laplacian filter over the input EGG data to improve the spatial resolution of EEG recordings [1], avoiding the influence of noise coming from neighboring channels [107]. Of note, the first five seconds are removed from resting data because of measured variations [139].

In practice, extraction from fewer sensorimotor area is achieved in order to reduce the computational complexity without affecting the BCI system performance [26]. To this end, we select the EEG recordings measured over the sensorimotor area, evaluating two configurations of scalp positions: (a) narrow electrode arrangement (noted as 2Ch) that includes two channels (C'=2): C3 (left motor cortical region) and C4 (right), (b) wide arrangement (6Ch) that holds six surrounding electrodes (C'=6): C3 and P3 (left motor cortex), Cz and Pz (middle cortex), and C4 and P4 (right cortex).

5.2.2 Bi-Class Accuracy Estimation as a Response Variable

We perform the individual accuracy in distinguishing either MI class as the performance response in order to validate the proposed data-driven estimator approach. The classifier accuracy is computed using the sliding short-time feature set extracted by the algorithm of CSP, fixing the surrogate space variance to the first three eigenvectors by class, as carried out in [140]. It is worth noting that the short-time window must be adjusted for extracting the subject EEG dynamics over time accurately. To reflect this influence, we test four different lengths of the sliding window: $\delta\tau$=$[0.5, 1.0, 1.5, 2.0]$ s, having an overlap of 50%.

[1]This filtering procedure was carried out using *Biosig Toolbox*, freely available at http://biosig.sourceforge.net

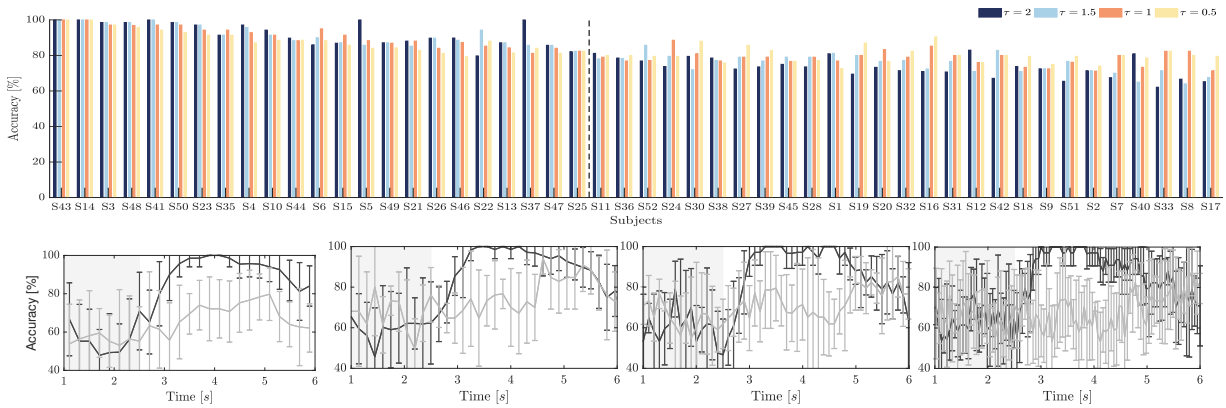

(a) $\delta\tau = 2$ (b) $\delta\tau = 1.5$ (c) $\delta\tau = 1$ (d) $\delta\tau = 0.5$

Figure 5.6: Individual accuracy in distinguishing either MI class performed by the CSP-based time-frequency feature set, using different window lengths: – $\delta\tau$=2, –$\delta\tau$=1.5, –$\delta\tau$=1, –$\delta\tau$=0.5. Bottom row: Accuracy for the trial timing using different windows S14 (marked with color –) and S17(–).

The top row in Figure 5.6 displays the classification accuracy achieved by each individual at different $\delta\tau$, employing the Linear Discriminant Analysis algorithm and applying the regularized selection strategy over the extracted CSP feature set together with a 10×10-fold cross-validation scheme, as carried out in [140]. For purposes of interpretation, all of the individuals are ranked in decreasing order according to the achieved CSP-based accuracy, showing that the less the classifier performance, the higher the dispersion between accuracy estimates extracted at different window lengths $\delta\tau$. However, the subjects performing the best have better accuracy at length $\delta\tau$=2, while the worst individuals achieve better at the shorter window $\delta\tau$=0.5, which means that the dynamics of neural responses may cluster into different groups in terms of the utilized extraction length $\delta\tau$.

As an illustration, the bottom row in Figure Figure 5.6 draws the time-varying classification accuracy achieved by two representative subjects: the individual labeled as S14 that reaches very high scores across the whole MI interval and the subject S17 that presents the lowest distinguishing ability, performing the highest accuracy unusually late (after the expected ΔT_2 interval).

5.2.3 Computation of Pre-Training Desynchronization Indicator

For extracting the PSD-fitting values in Equation (2.16a), the power spectral density $\boldsymbol{s}(f)$ of each Laplacian-filtered channel, $\{\boldsymbol{x}^c\}$, is computed through the nonparametric Welch's method. To this, we use a set of smooth-time sliding windows of length 1 s, fixing an overlap of 50% in order to overcome the non-stationary nature of EEG data. Further, we perform a single estimate of ξ_1 as the mean value averaged across the tested scalp electrode configuration.

Figure 5.7 depicts the curve-fitting model obtained, respectively, by the baseline interval (outlined in black color) and resting-state (gray color). The PSD estimate is drawn by a continuous line, the curve-fitting–by an asterisk line, and the hyperbolic fitting of noise–by a dashed line. In the case of subject # 14 reaching high accuracy, the top row

presents the performed curve-fitting with a high indicator value, showing a big match between the modeled and PSD estimated from the resting-state in each one of the six considered channels. As expected, the spatial configuration 2Ch provides the best values of ξ_1, which are large enough when compared with the remaining channels. On the contrary, the subject S17 with a very low accuracy performs a small indicator because of a poor fitting agreement (see the bottom row), also having no distinguishable activity at μ and β rhythms, regardless of the channel. The values of curve-fitting adjustment are shown beneath the plots, resulting in very close estimates for the pre-training desynchronization indicator despite the resting data extraction interval.

Figure 5.8 displays the indicator that was calculated by Equation (Equation (2.16a)) according to the achieved CSP-based accuracy that is ranked in decreasing order. As seen in the top row, the baseline inverval estimates extracted from 2Ch configuration (colored with blue squares) have a behavior that is comparable to the values that were recomputed by expanding to 6Ch the number of MI channels (green squares). A similar situation holds for the resting state indicator computed, as observed in the bottom row. It is worth noting that, although there is a high resemblance between both individual assessments (close to 50%), either calculated version of ξ_1 barely follows the ranked accuracy sequence of individuals.

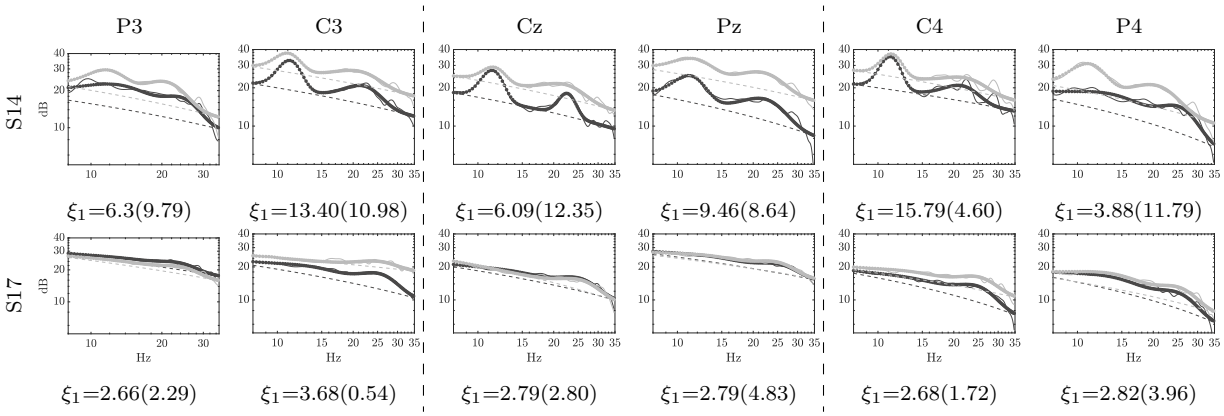

Figure 5.7: Examples of pre-training power spectral density (PSD)-fitting computed within resting data: baseline inverval (black line) and resting (gray line). Values of ξ_1 are reported for the sensorimotor area of baseline inverval and (resting) states.

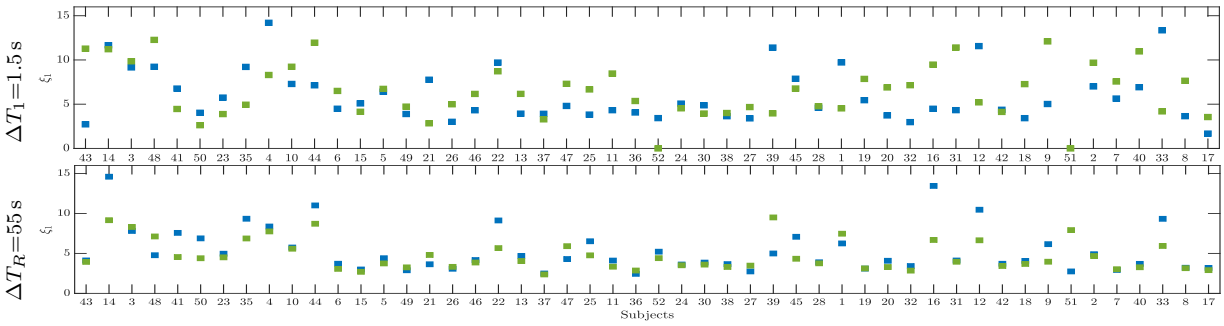

Figure 5.8: Pre-training desynchronization indicator ξ_1 computed for baseline inverval (top plot) and resting data (bottom row) while using either electrode arrangement: 2Ch (blue color) and 6Ch (green color). Individuals are ranked according with the achieved accuracy response.

5.2.4 Initial Training Synchronization Assessment

Here, we extract the ERD/ERS dynamics over the entire filtered trial matrix, fixing the time window to the sample rate (0.004 s). Additionally, the reference interval is fixed to the range 0.5–1.5 s while using the significance value of 1% in z-score approach, as performed in [119].

Figure 5.9 displays the individual pattern changes extracted from the electrode arrangement Ch6, holding the cue onset interval (shadowed area) and the MI segment ΔT_2. As seen, the induced synchronization mechanisms are represented through the increase or decrease of energy at the post-stimulus period. For illustration purposes, the corresponding time series are presented for a couple of representative subjects: S14 that performs high accuracy and S17, achieving a low accuracy. The former individual provides distinctive modulation amplitudes all over the sensorimotor area, while the latter subject presents a weak synchronization behavior, as observed in the top row.

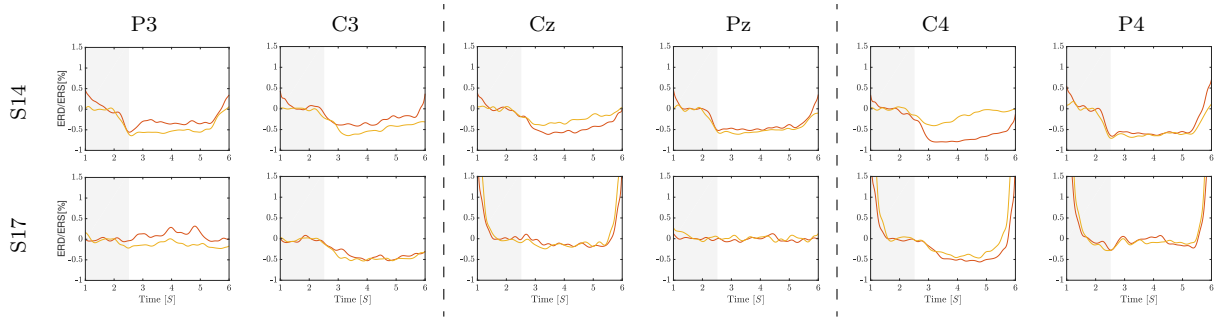

Figure 5.9: Exemplary ERD/ERS time-courses performed by subjects S17 and S14 for left-hand class (colored in red line) and right-hand class (in yellow) at the evaluated scalp electrodes, while using the back resting state (shadowed area) as the reference segment.

Further, Figure 5.10 displays the assessments of individual synchronization that are computed while using the labeled-related distance in Equation (Equation (2.17)) within the sensorimotor rhythms, for which the electrical brain activity prompted by motor tasks

is frequently associated. The computed values of initial training synchronization ξ_2 hardly follow the accuracy sequence of individuals, as observed in the previous indicator.

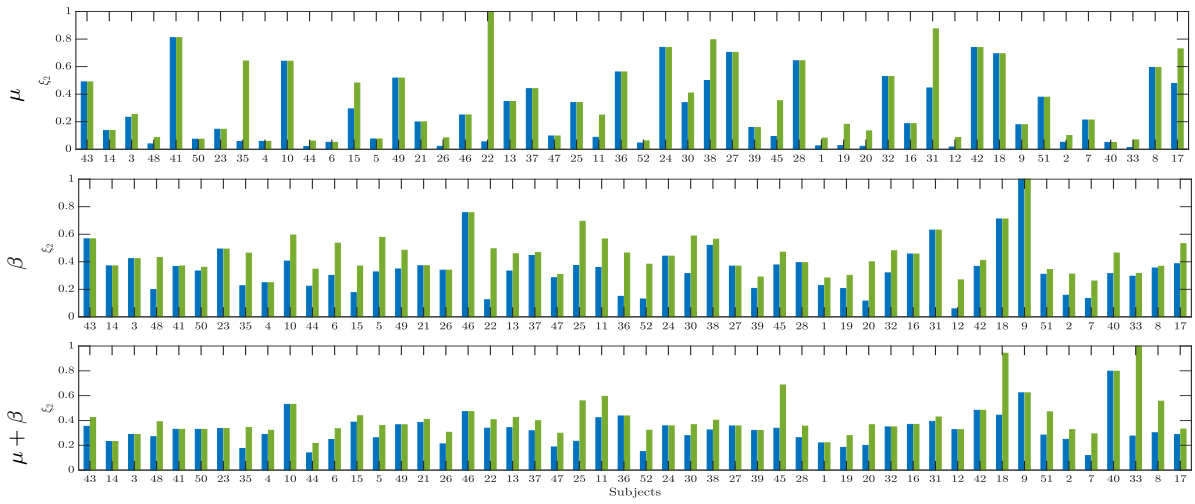

Figure 5.10: Individual values of initial training synchronization ξ_2 computed within subband combinations: $\mu, \beta, \mu+\beta$.

One more aspect to consider is the indicator's capacity to characterize the training session's synchronization mechanism. To this end, we extract ξ_2 while using a sequence of 30 trials ordered in time. Fixing a significance value of 5%, Figure 5.11 displays the results of the Wilcoxon signed-rank test, revealing that the first 30 trials are different from the second run. Likewise, the second run differs from the last one (only three runs are considered, since not all subjects have the same number of trials). Moreover, the mean value of ξ_2 decreases over the runs, which suggests that the synchronization mechanism can be evaluated as the training sessions increases in number. Overall, these outcomes in Figure Figure 5.11 agree to the results in [141], evidencing the difficulty of quantifying a significant change in ERD/ERS across the training sessions, even for either channel C3 or C4.

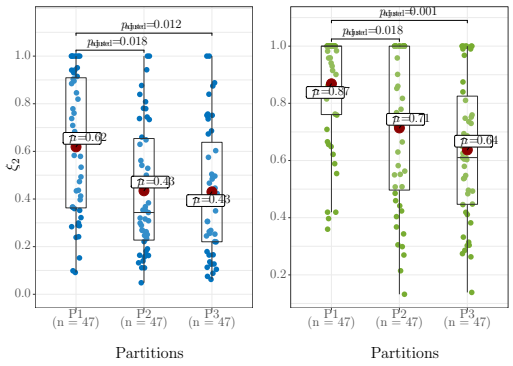

(a) 2CH (b) 6CH

Figure 5.11: Differences in initial training synchronization ξ_2 performed at each trial partition during the training sessions.

5.2.5 Drn-Based Indicator Extraction and Regression

Aiming at assessing the effectiveness of the pre-training desynchronization indicator ξ_1, Table 5.1 displays Spearman's correlation coefficient, $r \in \mathbb{R}$, which is reported under two different regression assumptions: linear (noted as LC) and linearized (DRN). In the case of extracting ξ_1 by Equation (Equation (2.16a)) from the baseline inverval, the linear correlates with the responses yield a minimal value of r, regardless of the associated accuracy response. The efficiency for predicting the subject accuracy remains not significant ($r<0.23$), even though the expanded electrode arrangement increases the Spearman coefficient a little. Further, the values of r are performed through the linearizing DRN estimator while using the same scalar-valued PSD-fitting indicator set (noted as DRN $\tilde{\xi}^*=\xi_1$), which is obtained by concatenating all of the trials before carrying out the short-time vector extraction, as implemented in [1]. As a result, the correlation with the MI performance raises to $r<0.37$, but this indicator poses still not meaningful for prediction. Lastly, the use of the DRN framework for joint indicator extraction and regression (noted as DRN $\boldsymbol{\xi}^*$) leads to a notable increase of the Spearman coefficient up to $r<0.88$, allowing for an adequate predictive interpretation of the data-driven pre-training desynchronization indicator.

When extracting ξ_1 by Equation (Equation (2.16a)) from a single resting-state record, the linear assumption increases almost by two the values of r as compared to the previous baseline inverval extraction. This result may point out that the resting-state data enable a more confident estimation of the desynchronization indicator. Nonetheless, for these scalar-valued estimates, the DRN estimator cannot further improve their predictive ability with the accuracy responses ($r < 0.40$). However, the joint model of DRN-based indicator extraction and regression leads to a definite rise in the correlation coefficient, outperforming all of the tested scenarios of resting data ($r < 0.93$).

Table 5.1: Biserial Spearman correlation coefficient quantified between the ξ_1 indicator, extracted within different scenarios of resting data, and the accuracy response, estimated at each window length of $\delta\tau$. Notations LC, DRN, and LOO stand for Linear Correlation [1], Deep Regression Network, and leave-one-out-cross validation strategy, respectively. The best value per row is marked in bold.

Resting Data	***Electrode***	$\delta\tau$ [s]				$\psi(\cdot)$	
	Configuration	**0.5**	**1.0**	**1.5**	**2.0**	***Mean***	**PCA$_1$**
Baseline inverval	2Ch(LC)	0.15	0.15	**0.17**	0.16	0.13	0.15
	6Ch(LC)	0.07	0.04	0.11	**0.13**	0.05	0.07
	2Ch(DRN ξ^*=ξ_1)	0.15	0.16	**0.18**	0.16	0.14	0.15
	6Ch(DRN ξ^*=ξ_1)	0.07	0.04	0.12	**0.14**	0.06	0.08
	2Ch(DRN $\boldsymbol{\xi}^*$)	0.86	0.85	0.96	**0.97**	0.83	0.87
	2Ch(DRN $\boldsymbol{\xi}^*$) LOO	0.76	0.79	0.82	0.80	0.78	**0.86**
	6Ch(DRN $\boldsymbol{\xi}^*$)	0.92	0.86	0.95	**0.97**	0.83	0.88
	6Ch(DRN $\boldsymbol{\xi}^*$) LOO	0.83	0.87	0.85	0.87	0.89	**0.91**
Resting-state	2Ch(LC)	0.30	0.31	0.31	0.27	0.29	**0.31**
	6Ch(LC)	0.25	0.31	0.26	0.26	**0.28**	**0.28**
	2Ch(DRN ξ^*=ξ_1)	0.31	0.31	0.31	0.28	0.30	**0.32**
	6Ch(DRN ξ^*=ξ_1)	0.25	**0.31**	0.26	0.27	0.30	0.30
	2Ch(DRN $\boldsymbol{\xi}^*$)	0.79	0.80	0.92	**0.94**	0.78	0.82
	2Ch(DRN $\boldsymbol{\xi}^*$) LOO	0.85	**0.87**	0.83	0.82	0.79	0.84
	6Ch(DRN $\boldsymbol{\xi}^*$)	0.86	0.77	0.91	**0.93**	0.75	0.80
	6Ch(DRN $\boldsymbol{\xi}^*$) LOO	0.85	0.83	**0.88**	0.86	0.80	0.77

The linear correlation values of (r<0.39) performed by the initial training synchronization ξ_2 are comparable to the ones of ξ_1, including both evaluated rhythm bandwidths μ+β and the wide electrode arrangement, as presented in Table 5.2. By feeding the DRN estimator with the scalar-valued ξ_2 (noted as DRN $\tilde{\xi}^*$=ξ_2), similar low significant correlation values are obtained, regardless of the evaluated rhythms. The fact that the proposed DRN estimator is not benefiting from a scalar-valued indicator set implies that involved Wide&Deep neural network demands a higher volume of information from predictors to perform learning of deep patterns.

On the other hand, the characterization of evoked MI activity poses a challenging task, because of the difficulty in quantifying the trial-to-trial variability accurately, increasing the complexity in assessing the distance ξ_2 between both labeled ERD/ERS time-series by Equation (Equation (2.17)). It should be noted that the indicators perform the best linear estimates of r at a distinct window length ($\delta\tau$=0.5 by ξ_1 while $\delta\tau$=0.5 by ξ_2), which means that this extraction parameter must be tuned differently for each indicator.

Once again, the DRN framework of joint indicator extraction and regression (DRN $\boldsymbol{\xi}^*$) enables an increase of the Spearman coefficient up to r<0.89, concatenating both labeled ERD/ERS time series at the estimator input. Therefore, for increasing the predictive interpretation of either considered electrophysiological indicator, the proposed DRN framework should incorporate the joint extraction and regression procedures, intending to extract more distinguishing information between subjects from the indicators.

Table 5.2: Computed values of r for the indicator of initial training synchronization within the evaluated rhythm bandwidths: $\mu, \beta, \mu{+}\beta$. Notations LC, DRN, and LOO stand for Linear Correlation [1], Deep Regression Network, and leave-one-out-cross validation strategy, respectively. The best value per row is marked in bold.

Rhythm	***Electrode***	$\tau\,[s]$				$\psi(\cdot)$	
Subband	***Configuration***	**0.5**	**1.0**	**1.5**	**2.0**	***Mean***	$\mathbf{PCA_1}$
μ	2Ch(LC)	**0.12**	0.064	0.04	0.003	0.6	0.05
	6Ch(LC)	**0.23**	0.08	0.10	0.04	0.11	0.11
	2Ch(DRN $\xi^*{=}\xi_2$)	0.13	0.064	0.13	**0.17**	0.06	0.17
	6Ch(DRN $\xi^*{=}\xi_2$)	**0.23**	0.12	0.10	0.04	0.11	0.11
β	2Ch(LC)	**0.11**	0.06	0.08	0.02	0.07	0.06
	6Ch(LC)	**0.14**	0.04	0.006	0.016	0.11	0.07
	2Ch(DRN $\xi^*{=}\xi_2$)	0.16	0.15	0.20	**0.23**	0.16	0.20
	6Ch(DRN $\xi^*{=}\xi_2$)	0.19	0.05	0.23	**0.25**	0.21	0.20
$\mu + \beta$	2Ch(LC)	**0.06**	0.05	0.05	0.01	0.04	0.04
	6Ch(LC)	**0.11**	0.07	0.03	0.04	**0.11**	0.08
	2Ch(DRN $\xi^*{=}\xi_2$)	0.08	0.06	0.10	**0.18**	0.11	0.09
	6Ch(DRN $\xi^*{=}\xi_2$)	0.11	0.11	0.19	**0.21**	0.15	**0.21**
	2Ch(DRN $\boldsymbol{\xi}^*$)	0.84	0.80	**0.94**	0.91	0.78	0.83
	2Ch(DRN $\boldsymbol{\xi}^*$) LOO	0.15	0.17	**0.24**	0.19	0.18	0.21
	6Ch(DRN $\boldsymbol{\xi}^*$)	0.87	0.77	0.93	**0.95**	0.82	0.82
	6Ch(DRN $\boldsymbol{\xi}^*$) LOO	0.20	**0.44**	0.40	0.28	0.26	0.40

5.2.6 Clustering of Subject-Level Efficiency

Here, we assume the rationale by which the higher the accuracy in distinguishing between MI tasks, the more efficient the individual brain network. Therefore, the sets of the extracted indicator values, together with the accuracy series, are employed to infer the distinctiveness between the subject assemblies, each having a similar variability level.

In the beginning, we determine the number of partitions considering the intra and inter-subject variability of responses as an important factor affecting the regression analysis that was conducted by Equation (2.19). Thus, an adequate group number is found to be three, which we estimate through the k-means algorithm fed by the four accuracy sets accounting for the performance variability, because of the extraction window length, $\delta\tau$ (see Figure 5.6), and introducing the cluster inertia and the Silhouette score to minimize the objective function.

The top row in Figure 5.12 displays the maximal accuracy that was performed by each subject within the extraction window set and his assigned group (left plot). The corresponding right plot depicts the resulting cluster by the colored dots into the following three partitions of individuals:

(i) A group that holds the individuals performing the best accuracy with very low variability (yellow color).

(ii) A group that contains the subjects that reach important values of accuracy, but performing with some fluctuations.

(*iii*) A group with modest accuracy performed with high unevenness.

In the following, each group is assumed to have distinguishable skills in practicing Motor Imagery tasks.

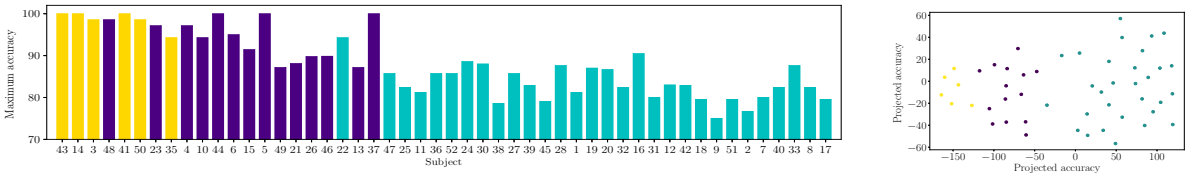

(a) Estimation of the partion number

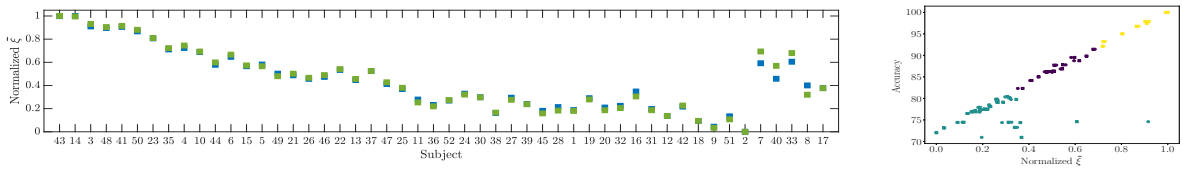

(b) DRN-based pre-training desynchroniation indicator $\xi^*=\xi_1$ extracted within resting data ΔT_1

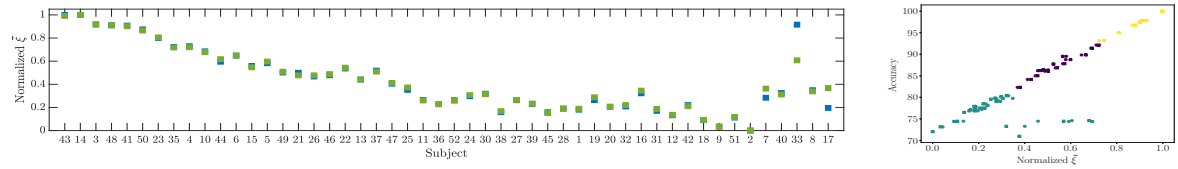

(c) DRN-based pre-training desynchroniation indicator $\xi^*=\xi_1$ extracted within resting data ΔT_R

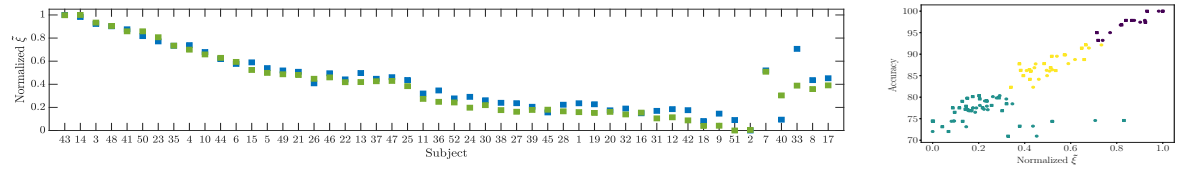

(d) DRN-based pre-training desynchroniation indicator $\xi^*=\xi_1$ extracted from $(\mu+\beta)$ rhythms

Figure 5.12: Extracted assessments using the proposed DRN estimator (left-side column) and performed clustering of subjects (right-side column).

The rows (b)–(d) in Figure 5.12 present the indicators that were extracted by the proposed DRN in Equation (2.19) that perform the best Spearman correlation r, meaning that they provide a high ability to predict the bi-class accuracy response. It is worth noting the high linearity between each indicator and the performance response set ranked in decreasing order, as displayed in the left column. The right column depicts the three subject partitions that were accomplished by the DRN extracted indicators, which are evidently separated, regardless of the involved indicator. Furthermore, the similarities between 2Ch (colored with blue squares) and 6Ch (green squares) arrangements are not noticeable, meaning that the clustering is scarcely affected by the fluctuations of neural activity coming from neighboring electrodes.

Nonetheless, as seen at the end of the left-side plots, several subjects (namely, #7, #40, #33, #8, and #17) do not follow the trend, and they are out of the regression (right plots), which implies that the DNR framework is not able to linearize the indicators extracted from this group of subjects. Besides their lowest performed bi-class accuracy, the main reason accounting for this discrepancy is the implied variability in their response that exceeds the performed values by the remaining subject set, as explained before in Figure 5.6a. In fact, the outlier subject set's classification performance increases atypically at the end of the MI interval, so that some subjects do not provide distinguishable activity between μ and β rhythms. This issue seems to be relevant, since it proves that, along with the measured indicator variability, the response behavior also changes influence the resulting data-driven regression analysis. Consequently, the number of subject partitions is increased by one, and the appearing fourth group contains the outlier subject set for which the DRN estimator cannot infer any predictive ability because of their intra-subject variability.

Another concern is how few subjects can exchange the assigned clusters when accounting for each extracted indicator's influence. To illustrate this fact, in Figure 5.13 we display the matrix that spans the cells colored according to the individual group assigned by the DRN-based estimator. The top row shows that the just a couple of subjects downgrades from the group I to II, when utilizing the extracted by DRN-based indicator assessments (see the pictured sets of (b)–(d) in Figure 5.12). It is worth noting that either electrode arrangement performs the same clustering if it involves the entire trail set of EEG data.

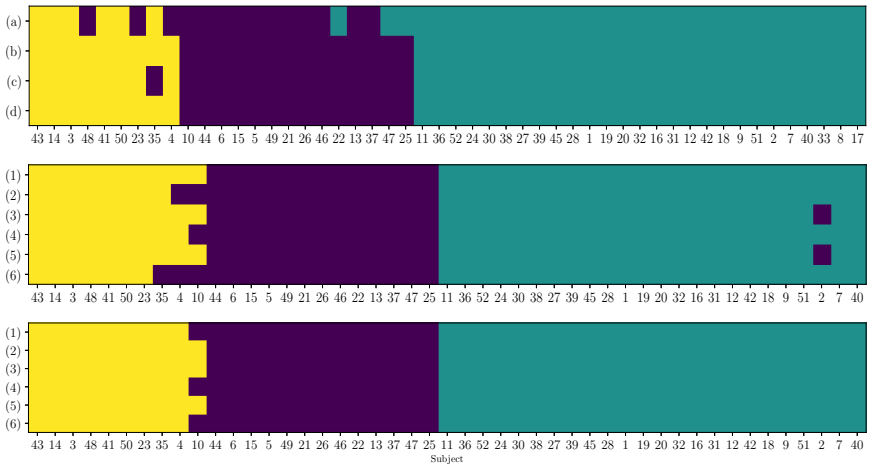

Figure 5.13: Clustering of individuals according to the DRN-based indicator extraction and regression. In first row, notations a),b), c), and d) stand for the corresponding items in Figure 5.12. The last two rows show the cluster of the DRN-based indicator $\xi^*=\xi_2$ extracted from $(\mu+\beta)$ rhythms, removing 10 trials consecutively in six runs with 2CH and 6CH electrode configuration, respectively.

5.2.7 Discussion

To provide a better understanding of the BCI-inefficiency, we develop a data-driven estimator, termed Deep Regression Network (DRN), which jointly extracts and performs the regression analysis to assess the efficiency the individual brain networks in practicing MI

tasks. To deal with the high inter- and intra-subject variability of elicited neural activity, the estimator performs learning of deep patterns, allowing to infer the distinctiveness between subject assemblies having similar variability. The results, which were obtained on real-world MI data, prove that the DRN estimator fosters the ability of the pre-training neural desynchronization and initial training synchronization to predict the bi-class accuracy response and, thus, providing a better understanding of the user's intent of action upon imagination tasks. The regression-based evaluation of the tested neurophysiological indicators for predicting the subject's ability to practice motor imagery tasks implies the following aspects:

Electrophysiological indicators in evaluation efficiency. We appraise the ability of pre-training neural desynchronization to predict the system response, showing that the computation by the baseline PSD-fitting may result in low significant correlates to the bi-classification accuracy ($r < 0.23$), at least, if performing extraction from the back-resting state. By extracting from resting-state data, the correlation with the MI performance raises to $r < 0.37$, remaining still not meaningful for prediction. Besides, the initial training synchronization indicator is assessed while using a proposed distance between both labeled Event-related De/Synchronization time-series that hardly follows the accuracy, sequence of individuals, resulting in low significant correlation values, regardless of the evaluated rhythms. However, other approaches of ERD/ERS calculation are to be evaluated, like event-related spectral perturbation technique [142].

Classifier accuracy as a response variable. In order to assess the efficiency of individual brain networks, the accuracy in distinguishing between MI tasks is widely employed, which is frequently computed while using the sliding short-time feature set extracted by the algorithm of Common Spatial Patterns. However, to deal with the intra inter-subject variability, the short-time length must be adjusted for each subject properly (see Figure 5.6). Furthermore, the individuals performing the worst are more susceptible to this choice, degrading the regression analysis highly. As a result, either indicator's predictive ability depends differently on this extracting parameter, at least, using linear regression (see Tables 5.1 and 5.2). This result may lead to a restriction when gathering several electrophysiological indicators into a common regression framework to improve efficiency evaluation of subjects.

Joint model of indicator extraction and regression analysis. For increasing the predictive interpretation of either considered electrophysiological indicator, we develop a Deep Regression Network framework that, first, extracts from neural activity indicators the most salient patterns that allow evaluating the BCI inefficiency, and then performs linearization of the indicator assessments towards the accuracy response. As a result, there is high linearity between the extracted sets for either indicator and the ranked performance response values of subjects. To include the accuracy variability because of window extraction, we test the mean accuracy weighted across the subject variance and the first PCA eigenvalue of the accuracy vectors, both performing similarly and outperforming notably the results that were obtained by each particular window length. Nonetheless, the proposed DRN estimator does not benefit from scalar-valued indicator sets, since the included Wide&Deep neural network demands a larger amount of information from predictors to perform learning of deep patterns.

One more aspect to remark is that the developed prediction model is subject-dependent

and has to be validated with trial sets acquired under similar conditions from a representative number of individuals. As a rule, publicly available motor imagery databases are small, unusually exceeding several dozens because of their associated cost of implementation. We also need to validate the resting-state data that are less present in MI collections, since their capture demands a different paradigm, increasing the acquisition complexity. Here, we use the leave-one-out-cross validation strategy (LOO) to reduce the variability derived by splitting into two groups the validating data (training and test), enhancing the generalizing ability of the developed predictor and the model reproducibility, even under such an amount of examined individuals, aiming to understand why some subject groups show different performances in the same system.

Cluster of subject efficiency. The extracted indicator assessments, together with the accuracy series, are employed to infer the distinctiveness between the subject groups with a comparable variability level, that is, having similar skills in practicing MI tasks. As a result, the DRN estimator provides three subject partitions with the predictive ability regardless of the involved indicator and barely affected by the fluctuations of neural activity coming from neighboring electrodes. One more group with nonpredictive ability is obtained that holds the subjects with the lowest and most variable estimates of accuracy. The DNR framework is not able to linearize this group, which confirms that the changes in the response behavior also influence the resulting data-driven regression analysis.

Nonetheless, some issues remain to enhance the BCI-inefficiency evaluation through the developed data-drive DRN estimator. Firstly, the extraction of indicators should be improved; for instance, the assessment of the initial training synchronization must be performed using more elaborate labeled-based distances. Generally, the ℓ_2 loss function tends to limit the generalization ability due to its susceptibility to outliers. Instead, using the combined $\ell_{2,1}$-norm concept loss (or even ℓ_∞-norm), the curve-fitting indicator in Equation (2.16a) can be improved. Further, the DRN framework should be enhanced in order to include the joint extraction of several indicators, taking into account the differences in the de/synchronization mechanism between both brain hemispheres. Additionally, there is a need to develop a more powerful mapping function to include the system response's stochastic behavior. Another aspect of improving is the Deep Network architecture to enhance the interpretation of spatial brain neural patterns that mainly contribute to evaluating indicators' efficiency in practicing MI tasks.

Chapter 6

Conclusions

This work presents four main contributions. Firstly, to build up the subject-level feature sets, a common representation space is proposed that encodes the electrode (spatial) contribution, evolving through time and frequency domains. To address sources of inter-subject variability of individuals, a *t-f* feature set is extracted, for which the domain parameters (time window length and filter bandwidth setup) are selected to be the more relevant in discriminating between MI tasks, yielding a distinct dimensionality of each extracted characteristic set. Because of the difference in the captured dynamics, each engaged extraction method differently reflects the flow of sensorimotor cortex activation during the analyzed representative MI intervals.

Secondly, we present the Entropy-based method, termed *VQEnt*, for estimation of Event-Related De/Synchronization using a dynamic description through quantized stochastic patterns, aiming to improve discriminability and physiological interpretability of motor imagery tasks. The validating results, obtained on the widely used database, show that *VQEnt* outperforms others sample-based approaches while providing adequate interpretability in Motor Imagery tasks. The proposed method is sample-based and builds the probabilistic priors by assessing the Gaussian similarity between the input EEG measurements and their reduced vector-quantized representation. As a concluding remark, we propose to enhance the entropy-based estimation by extracting more information about amplitudes of time-courses that show more differences in distinguishing between MI tasks. We hypothesize that by extracting a more reliable representation of the stochastic patterns, the discriminability of labeled tasks can be increased while preserving elicited brain neural activity's physiological interpretation.

Thirdly, we develop a dynamic model for estimating the common neural activity across subjects to provide new insights into the evolution of collective mental imagery processes. After the preprocessing stage, the *t-f* EEG signal set is fed into a feature extraction algorithm to improve the efficiency of triggering activity representation. Then, we employ a statistical thresholding algorithm to extract a multi-subject model that provides a set of confident estimates contributing the most to discriminating between MI tasks. We compare three feature extraction methods for making group inferences from subject-level dynamic information of neural activity. The obtained validation results indicate that the estimated collective dynamics reflect the flow in sensorimotor cortex activation differently. Therefore, the common model addresses inter-subject and inter-trial variability sources

individually, depending on the engaged extraction method.

Lastly, to provide a better understanding of the BCI-inefficiency, we develop a data-driven estimator, termed Deep Regression Network (DRN), which jointly extracts and performs the regression analysis to assess the efficiency the individual brain networks in practicing MI tasks. To deal with the high inter- and intra-subject variability of elicited neural activity, the estimator performs learning of deep patterns, allowing to infer the distinctiveness between subject assemblies having similar variability. The results, which were obtained on real-world MI data, prove that the DRN estimator fosters the ability of the pre-training neural desynchronization and initial training synchronization to predict the bi-class accuracy response and, thus, providing a better understanding of the user's intent of action upon imagination tasks.

Bibliography

[1] B. Blankertz, C. Sannelli, S. Halder, E. M. Hammer, A. Kübler, K.-R. Müller, G. Curio, and T. Dickhaus, "Neurophysiological predictor of smr-based bci performance," *Neuroimage*, vol. 51, no. 4, pp. 1303–1309, 2010.

[2] B. Babadi, "Neural encoding and decoding," *Handbook of Neuroengineering*, pp. 1–24, 2020.

[3] A. Singh, A. A. Hussain, S. Lal, and H. W. Guesgen, "A comprehensive review on critical issues and possible solutions of motor imagery based electroencephalography brain-computer interface," *Sensors*, vol. 21, no. 6, p. 2173, 2021.

[4] A. M. Álvarez-Meza, L. F. Velásquez-Martínez, and G. Castellanos-Dominguez, "Time-series discrimination using feature relevance analysis in motor imagery classification," *Neurocomputing*, vol. 151, pp. 122–129, 2015.

[5] Y. K. Stolbkov, T. R. Moshonkina, I. V. Orlov, E. S. Tomilovskaya, I. B. Kozlovskaya, and Y. P. Gerasimenko, "The neurophysiological correlates of real and imaginary locomotion," *Human Physiology*, vol. 45, no. 1, pp. 104–114, 2019.

[6] B. Fadlallah, S. Seth, A. Keil, and J. Principe, "Quantifying cognitive state from eeg using dependence measures," *IEEE Transactions on Biomedical Engineering*, vol. 59, no. 10, pp. 2773–2781, 2012.

[7] Z. Chen, "A primer on neural signal processing," *IEEE Circuits and Systems Magazine*, vol. 17, no. 1, pp. 33–50, 2017.

[8] S. N. Abdulkader, A. Atia, and M.-S. M. Mostafa, "Brain computer interfacing: Applications and challenges," *Egyptian Informatics Journal*, vol. 16, no. 2, pp. 213–230, 2015.

[9] M. W. Woolrich, A. Baker, H. Luckhoo, H. Mohseni, G. Barnes, M. Brookes, and I. Rezek, "Dynamic state allocation for meg source reconstruction," *Neuroimage*, vol. 77, pp. 77–92, 2013.

[10] C. Guerrero-Mosquera and A. Navia-Vázquez, "Automatic removal of ocular artefacts using adaptive filtering and independent component analysis for electroencephalogram data," *IET signal processing*, vol. 6, no. 2, pp. 99–106, 2012.

[11] M. Saeidi, W. Karwowski, F. V. Farahani, K. Fiok, R. Taiar, P. Hancock, and A. Al-Juaid, "Neural decoding of eeg signals with machine learning: a systematic review," *Brain Sciences*, vol. 11, no. 11, p. 1525, 2021.

[12] D. R. Ripoll, "Introducción a la organización del sistema nervioso," in *Neurociencia cognitiva*. Editorial Médica Panamericana, 2013, pp. 67–110.

[13] Y.-H. Liu, L.-F. Lin, C.-W. Chou, Y. Chang, Y.-T. Hsiao, and W.-C. Hsu, "Analysis of electroencephalography event-related desynchronisation and synchronisation induced by lower-limb stepping motor imagery," *Journal of Medical and Biological Engineering*, vol. 39, no. 1, pp. 54–69, 2019.

[14] G. Rodríguez-Bermúdez and P. J. García-Laencina, "Automatic and adaptive classification of electroencephalographic signals for brain computer interfaces," *Journal of medical systems*, vol. 36, no. 1, pp. 51–63, 2012.

[15] S. Lemm, B. Blankertz, T. Dickhaus, and K.-R. Müller, "Introduction to machine learning for brain imaging," *Neuroimage*, vol. 56, no. 2, pp. 387–399, 2011.

[16] E. Opsommer, O. Chevalley, and N. Korogod, "Motor imagery for pain and motor function after spinal cord injury: a systematic review," *Spinal Cord*, vol. 58, pp. 262–274, 2019.

[17] T. Machado, A. Carregosa, M. Santos, N. da Silva, and M. Melo, "Efficacy of motor imagery additional to motor-based therapy in the recovery of motor function of the upper limb in post-stroke individuals: a systematic review," *Topics in Stroke Rehabilitation*, vol. 26, no. 7, pp. 548–553, 2019.

[18] G. Aymeric and D. Ursula, "Benefits of motor imagery for human space flight: A brief review of current knowledge and future applications," *Frontiers in Physiology*, no. 10, p. 396, 2019.

[19] P. Barhoun, I. Fuelscher, E. Kothe, J. He, G. Youssef, P. Enticott, J. Williams, and C. Hyde, "Motor imagery in children with dcd: A systematic and meta-analytic review of hand-rotation task performance," *Neuroscience & Biobehavioral Reviews*, vol. 99, pp. 282 – 297, 2019.

[20] V. Nicholson, N. Watts, Y. Chani, and J. Keogh, "Motor imagery training improves balance and mobility outcomes in older adults: a systematic review," *Journal of Physiotherapy*, vol. 65, no. 4, pp. 200 – 207, 2019.

[21] T. MacIntyre, C. Madan, C. Collet, and A. Guillot, "Motor imagery, performance and motor rehabilitation," vol. 240, pp. 141–159, 2018.

[22] S. G. Boe and S. N. Kraeutner, "Assessing motor imagery ability through imagery-based learning: An overview and introduction to miscreen, a mobile app for imagery assessment," *Imagination, Cognition and Personality*, vol. 37, no. 4, pp. 430–447, 2018.

[23] Z. Suica, P. Platteau-Waldmeier, S. Koppel, A. Schmidt-Trucksaess, T. Ettlin, and C. Schuster-Amft, "Motor imagery ability assessments in four disciplines: protocol for a systematic review," *BMJ Open*, vol. 8, no. 12, 2018.

[24] L. Power, H. F. Neyedli, S. G. Boe, and T. Bardouille, "Efficacy of low-cost wireless neurofeedback to modulate brain activity during motor imagery," *Biomedical Physics & Engineering Express*, vol. 6, no. 3, p. 035024, 2020.

[25] N. Tiwari, D. R. Edla, S. Dodia, and A. Bablani, "Brain computer interface: A comprehensive survey," *Biologically Inspired Cognitive Architectures*, vol. 26, pp. 118–129, 2018.

[26] M. Z. Baig, N. Aslam, and H. P. H. Shum, "Filtering techniques for channel selection in motor imagery EEG applications: a survey," *Artificial Intelligence Review*, pp. 1–26, 2019.

[27] M. L. Stavrinou, L. Moraru, L. Cimponeriu, S. Della Penna, and A. Bezerianos, "Evaluation of cortical connectivity during real and imagined rhythmic finger tapping," *Brain Topography*, vol. 19, no. 3, pp. 137–145, 2007.

[28] L. S. Imperatori, M. Betta, L. Cecchetti, A. Canales-Johnson, E. Ricciardi, F. Siclari, P. Pietrini, S. Chennu, and G. Bernardi, "Eeg functional connectivity metrics wpli and wsmi account for distinct types of brain functional interactions," *Scientific reports*, vol. 9, no. 1, pp. 1–15, 2019.

[29] B. Juan, E. Santiago, B.-M. Arturo, N. Marius, B. Javier, F. Eduardo, S. Surjo, and G.-A. Nicolas, "Synchronization of slow cortical rhythms during motor imagery-based brain-machine interface control," *International journal of neural systems*, vol. 29, no. 5, p. 1850045, 2019.

[30] P. Wierzgała, D. Zapała, G. M. Wojcik, and J. Masiak, "Most popular signal processing methods in motor-imagery bci: a review and meta-analysis," *Frontiers in neuroinformatics*, vol. 12, p. 78, 2018.

[31] E. Friedrich, R. Scherer, and C. Neuper, "Stability of event-related (de-) synchronization during brain-computer interface-relevant mental tasks," *Clinical Neurophysiology*, vol. 124, no. 1, pp. 61–69, 2013.

[32] P. K. Pattnaik and J. Sarraf, "Brain computer interface issues on hand movement," *Computer and Information Sciences*, vol. 30, no. 1, pp. 18–24, 2018.

[33] Y. Park and W. Chung, "Frequency-optimized local region common spatial pattern approach for motor imagery classification," *IEEE Transactions on Neural Systems and Rehabilitation Engineering*, vol. 27, no. 7, pp. 1378–1388, 2019.

[34] S. Saha, K. Ahmed, R. Mostafa, L. Hadjileontiadis, and A. Khandoker, "Evidence of variabilities in EEG dynamics during motor imagery-based multiclass brain-computer interface," *IEEE Transactions on Neural Systems and Rehabilitation Engineering*, vol. 26, no. 2, pp. 371–382, 2018.

[35] M. Ahn and S. C. Jun, "Performance variation in motor imagery brain–computer interface: a brief review," *Journal of neuroscience methods*, vol. 243, pp. 103–110, 2015.

[36] C. Jeunet, S. Debener, F. Lotte, J. Mattout, R. Scherer, and C. Zich, "Mind the traps! design guidelines for rigorous BCI experiments," in *Brain–Computer Interfaces Handbook*. CRC Press, 2018, pp. 639–660.

[37] M. C. Thompson, "Critiquing the concept of bci illiteracy," *Science and engineering ethics*, vol. 25, no. 4, pp. 1217–1233, 2019.

[38] T. Liu, G. Huang, N. Jiang, L. Yao, and Z. Zhang, "Reduce brain computer interface inefficiency by combining sensory motor rhythm and movement-related cortical potential features," *Journal of neural engineering*, vol. 17, no. 3, p. 035003, 2020.

[39] P. Durka, D. Ircha, C. Neuper, and G. Pfurtscheller, "Time-frequency microstructure of event-related electro-encephalogram desynchronisation and synchronisation," *Medical & biological engineering & computing*, vol. 39, pp. 315–321, 2001.

[40] R. Grandchamp and A. Delorme, "Single-trial normalization for event-related spectral decomposition reduces sensitivity to noisy trials," *Frontiers in Psychology*, vol. 2, p. 236, 2011.

[41] H. Yuan and B. He, "Brain–computer interfaces using sensorimotor rhythms: current state and future perspectives," *IEEE Transactions on Biomedical Engineering*, vol. 61, no. 5, pp. 1425–1435, 2014.

[42] X. Tang, W. Li, X. Li, W. Ma, and X. Dang, "Motor imagery eeg recognition based on conditional optimization empirical mode decomposition and multi-scale convolutional neural network," *Expert Systems with Applications*, vol. 149, p. 113285, 2020.

[43] L. Gao, J. Wang, and L. Chen, "Event-related desynchronization and synchronization quantification in motor-related eeg by kolmogorov entropy," *Journal of neural engineering*, vol. 10, no. 3, p. 036023, 2013.

[44] H. Azami, P. Li, S. Arnold, J. Escudero, and A. Humeau-Heurtier, "Fuzzy entropy metrics for the analysis of biomedical signals: Assessment and comparison," *IEEE Access*, vol. 7, pp. 104 833–104 847, 2019.

[45] H. Wei-Yen, "Assembling a multi-feature eeg classifier for left-right motor imagery data using wavelet-based fuzzy approximate entropy for improved accuracy," *International journal of neural systems*, vol. 25-8, p. 1550037, 2015.

[46] C. Shunfei, L. Zhizeng, and G. Haitao, "An entropy fusion method for feature extraction of EEG," *Neural Computing and Applications*, vol. 29, pp. 857–863, 2016.

[47] P. Sri, K. Yashasvi, A. Anjum, A. Bhattacharyya, and R. Pachori, *Development of an Effective Computing Framework for Classification of Motor Imagery EEG Signals for Brain–Computer Interface*. Singapore: Springer Singapore, 2020, pp. 17–35.

[48] M. Rostaghi and H. Azami, "Dispersion entropy: A measure for time-series analysis," *IEEE Signal Processing Letters*, vol. 23, pp. 610–614, 2016.

[49] K. Kuntzelman, L. Rhodes, L. Harrington, and V. Miskovic, "A practical comparison of algorithms for the measurement of multiscale entropy in neural time series data," *Brain and Cognition*, vol. 123, pp. 126–135, 2018.

[50] Y. Li, X. Gao, and Wang.L, "Reverse dispersion entropy: A new complexity measure for sensor signal," *Sensors (Basel, Switzerland)*, vol. 19, 2019.

[51] E. Kafantaris, I. Piper, M. Lo, and J. Escudero, "Augmentation of dispersion entropy for handling missing and outlier samples in physiological signal monitoring," *Entropy*, no. 319, pp. 1–26, 2020.

[52] E. Pitsik, N. Frolov, K. Hauke, V. Grubov, V. Maksimenko, J. Kurths, and A. Hramov, "Motor execution reduces eeg signals complexity: Recurrence quantification analysis study¡? a3b2 show [feature]?¿," *Chaos: An Interdisciplinary Journal of Nonlinear Science*, vol. 30, no. 2, p. 023111, 2020.

[53] M. Miao, H. Zeng, A. Wang, C. Zhao, and F. Liu, "Discriminative spatial-frequency-temporal feature extraction and classification of motor imagery EEG: An sparse regression and weighted naïve bayesian classifier-based approach," *Journal of neuroscience methods*, vol. 278, pp. 13–24, 2017.

[54] N. Bigdely-Shamlo, G. Ibagon, C. Kothe, and T. Mullen, "Finding the optimal cross-subject EEG data alignment method for analysis and BCI," in *2018 IEEE International Conference on Systems, Man, and Cybernetics (SMC)*, 2018, pp. 1110–1115.

[55] S. Fazli, S. DÃ¤hne, W. Samek, F. BieÃŸmann, and K. MÃ¼ller, "Learning from more than one data source: Data fusion techniques for sensorimotor rhythm-based brain-computer interfaces," *Proceedings of the IEEE*, vol. 103, no. 6, pp. 891–906, 2015.

[56] G. Lio and P. Boulinguez, "How does sensor-space group blind source separation face inter-individual neuroanatomical variability? insights from a simulation study based on the PALS-B12 atlas," *Brain Topography*, vol. 31, pp. 62–75, 2016.

[57] X. Gong, L. Mao, Y. Liu, and Q. Lin, "A jacobi generalized orthogonal joint diagonalization algorithm for joint blind source separation," *IEEE Access*, vol. 6, pp. 38 464–38 474, 2018.

[58] Y. Zhang, C. S. Nam, G. Zhou, J. Jin, X. Wang, and A. Cichocki, "Temporally constrained sparse group spatial patterns for motor imagery BCI," *IEEE Transactions on Cybernetics*, vol. 49, no. 9, pp. 3322–3332, 2019.

[59] A. de CheveignÃ©, G. M. D. Liberto, D. Arzounian, D. D. Wong, J. HjortkjÃ¦r, S. Fuglsang, and L. C. Parra, "Multiway canonical correlation analysis of brain data," *NeuroImage*, vol. 186, pp. 728 – 740, 2019.

[60] R. J. Huster and L. Raud, "A tutorial review on multi-subject decomposition of eeg," *Brain topography*, vol. 31, no. 1, pp. 3–16, 2018.

[61] D. K. Emge, F.-B. Vialatte, G. Dreyfus, and T. Adalı, "Independent vector analysis for SSVEP signal enhancement, detection, and topographical mapping," *Brain Topography*, vol. 31, no. 1, pp. 117–124, 2018.

[62] S. Bhinge, R. Mowakeaa, V. D. Calhoun, and T. Adalı, "Extraction of time-varying spatiotemporal networks using parameter-tuned constrained iva," *IEEE transactions on medical imaging*, vol. 38, no. 7, pp. 1715–1725, 2019.

[63] R. J. Huster and L. Raud, "A tutorial review on multi-subject decomposition of EEG," *Brain Topography*, vol. 31, no. 1, pp. 3–16, 2018.

[64] D. A. Bridwell, J. F. Cavanagh, A. G. E. Collins, M. D. Nunez, R. Srinivasan, S. Stober, and V. D. Calhoun, "Moving beyond ERP components: A selective review of approaches to integrate EEG and behavior," *Frontiers in Human Neuroscience*, vol. 12, p. 106, 2018.

[65] N. Kriegeskorte, M. Mur, and P. Bandettini, "Representational similarity analysis - connecting the branches of systems neuroscience," *Frontiers in Systems Neuroscience*, vol. 2, p. 4, 2008.

[66] J. S. Müller, C. Vidaurre, M. Schreuder, F. C. Meinecke, P. Von Bünau, and K.-R. Müller, "A mathematical model for the two-learners problem," *Journal of neural engineering*, vol. 14, no. 3, p. 036005, 2017.

[67] A. Singh, S. Lal, and H. W. Guesgen, "Architectural review of co-adaptive brain computer interface," in *2017 4th Asia-Pacific World Congress on Computer Science and Engineering (APWC on CSE)*. IEEE, 2017, pp. 200–207.

[68] A. Abu-Rmileh, E. Zakkay, L. Shmuelof, and O. Shriki, "Co-adaptive training improves efficacy of a multi-day eeg-based motor imagery bci training," *Frontiers in Human Neuroscience*, vol. 13, p. 362, 2019.

[69] L. M. Alonso-Valerdi, "Python executable script for estimating two effective parameters to individualize brain-computer interfaces: Individual alpha frequency and neurophysiological predictor," *Frontiers in neuroinformatics*, vol. 10, p. 22, 2016.

[70] N. S. E. M. Noor and H. Ibrahim, "Machine learning algorithms and quantitative electroencephalography predictors for outcome prediction in traumatic brain injury: A systematic review," *IEEE Access*, vol. 8, pp. 102 075–102 092, 2020.

[71] L. A. Weber, T. Ethofer, and A.-C. Ehlis, "Predictors of neurofeedback training outcome: A systematic review," *NeuroImage: Clinical*, vol. 27, p. 102301, 2020.

[72] M. Vukelić and A. Gharabaghi, "Self-regulation of circumscribed brain activity modulates spatially selective and frequency specific connectivity of distributed resting state networks," *Frontiers in behavioral neuroscience*, vol. 9, p. 181, 2015.

[73] M. Ahn, H. Cho, S. Ahn, and S. C. Jun, "High theta and low alpha powers may be indicative of BCI-illiteracy in motor imagery," *PloS one*, vol. 8, no. 11, p. e80886, 2013.

[74] A. Bamdadian, C. Guan, K. K. Ang, and J. Xu, "The predictive role of pre-cue eeg rhythms on mi-based bci classification performance," *Journal of neuroscience methods*, vol. 235, pp. 138–144, 2014.

[75] L. Acqualagna, L. Botrel, C. Vidaurre, A. Kübler, and B. Blankertz, "Large-scale assessment of a fully automatic co-adaptive motor imagery-based brain computer interface," *PloS one*, vol. 11, no. 2, p. e0148886, 2016.

[76] W. Samek, C. Vidaurre, K.-R. Müller, and M. Kawanabe, "Stationary common spatial patterns for brain–computer interfacing," *Journal of neural engineering*, vol. 9, no. 2, p. 026013, 2012.

[77] M. Kwon, H. Cho, K. Won, M. Ahn, and S. C. Jun, "Use of both eyes-open and eyes-closed resting states may yield a more robust predictor of motor imagery bci performance," *Electronics*, vol. 9, no. 4, p. 690, 2020.

[78] F. Wan, W. Nan, M. I. Vai, and A. Rosa, "Resting alpha activity predicts learning ability in alpha neurofeedback," *Frontiers in human neuroscience*, vol. 8, p. 500, 2014.

[79] E. Solesio-Jofre, I. A. Beets, D. G. Woolley, L. Pauwels, S. Chalavi, D. Mantini, and S. P. Swinnen, "Age-dependent modulations of resting state connectivity following motor practice," *Frontiers in Aging Neuroscience*, vol. 10, p. 25, 2018.

[80] M.-C. Corsi, M. Chavez, D. Schwartz, N. George, L. Hugueville, A. E. Kahn, S. Dupont, D. S. Bassett, and F. D. V. Fallani, "Functional disconnection of associative cortical areas predicts performance during bci training," *NeuroImage*, vol. 209, p. 116500, 2020.

[81] C. A. Stefano Filho, T. B. d. S. Costa, L. Uribe, P. Rodrigues, D. Soriano, R. Attux, and G. Castellano, "On the (in) efficacy of motor imagery training without feedback and event-related desynchronizations considerations," *Biomedical Physics & Engineering Express*, vol. 6, no. 3, p. 035030, 2020.

[82] M. Daeglau, F. Wallhoff, S. Debener, I. S. Condro, C. Kranczioch, and C. Zich, "Challenge accepted? individual performance gains for motor imagery practice with humanoid robotic eeg neurofeedback," *Sensors*, vol. 20, no. 6, p. 1620, 2020.

[83] L. Velasquez-Martinez, J. Caicedo-Acosta, and G. Castellanos-Dominguez, "Entropy-based estimation of event-related de/synchronization in motor imagery using vector-quantized patterns," *Entropy*, vol. 22, no. 6, p. 703, 2020.

[84] P. Chholak, A. N. Pisarchik, S. A. Kurkin, V. A. Maksimenko, and A. E. Hramov, "Phase-amplitude coupling between mu-and gamma-waves to carry motor commands," in *2019 3rd School on Dynamics of Complex Networks and their Application in Intellectual Robotics (DCNAIR)*. IEEE, 2019, pp. 39–45.

[85] B. Kim and C. Winstein, "Can neurological biomarkers of brain impairment be used to predict poststroke motor recovery? a systematic review," *Neurorehabilitation and neural repair*, vol. 31, no. 1, pp. 3–24, 2017.

[86] J. Yperman, T. Becker, D. Valkenborg, V. Popescu, N. Hellings, B. V. Wijmeersch, and L. M. Peeters, "Machine learning analysis of motor evoked potential time series to predict disability progression in multiple sclerosis," *BMC neurology*, vol. 20, no. 1, pp. 1–15, 2020.

[87] L. D. Fiederer, M. Völker, R. T. Schirrmeister, W. Burgard, J. Boedecker, and T. Ball, "Hybrid brain-computer-interfacing for human-compliant robots: inferring continuous subjective ratings with deep regression," *Frontiers in Neurorobotics*, vol. 13, p. 76, 2019.

[88] A. H. Shahid and M. P. Singh, "A deep learning approach for prediction of parkinsonâ€™s disease progression," *Biomedical Engineering Letters*, vol. 10, no. 2, pp. 227–239, 2020.

[89] S. K. Pandey and R. R. Janghel, "Recent deep learning techniques, challenges and its applications for medical healthcare system: a review," *Neural Processing Letters*, vol. 50, pp. 1907–1935, 2019.

[90] A. S. Aghaei, M. S. Mahanta, and K. N. Plataniotis, "Separable common spatio-spectral patterns for motor imagery BCI systems," *IEEE Transactions on Biomedical Engineering*, vol. 63, no. 1, pp. 15–29, 2016.

[91] S. Brandl, K. Muller, and W. Samek, "Alternative CSP approaches for multimodal distributed BCI data," in *2016 IEEE International Conference on Systems, Man, and Cybernetics (SMC)*, 2016, pp. 003 742–003 747.

[92] A. M. Bastos and J.-M. Schoffelen, "A tutorial review of functional connectivity analysis methods and their interpretational pitfalls," *Frontiers in Systems Neuroscience*, vol. 9, p. 175, 2016.

[93] S. Dai and Q. Wei, "Electrode channel selection based on backtracking search optimization in motor imagery brain–computer interfaces," *Journal of integrative neuroscience*, vol. 16, no. 3, pp. 241–254, 2017.

[94] C. Sannelli, C. Vidaurre, K. Müller, and B. Blankertz, "Common spatial pattern patches-an optimized filter ensemble for adaptive brain-computer interfaces," in *2010 Annual International Conference of the IEEE Engineering in Medicine and Biology*. IEEE, 2010, pp. 4351–4354.

[95] A. Delgado-Bonal and A. Marshak, "Approximate entropy and sample entropy: A comprehensive tutorial," *Entropy*, vol. 21, p. 541, 2019.

[96] T. Nguyen and T. Nguyen, "Entropy-constrained maximizing mutual information quantization," *ArXiv*, 2020.

[97] S. Zhao, B. Chen, P. Zhu, and J. PrÃncipe, "Fixed budget quantized kernel least-mean-square algorithm," *Signal Processing*, vol. 93, no. 9, pp. 2759–2770, 2013.

[98] D. Cardenas-Pena, A. Tobar-Rodriguez, and G. Castellanos-Dominguez, "Adaptive Bayesian label fusion using kernel-based similarity metrics in hippocampus segmentation," *Journal of Medical Imaging*, vol. 6, no. 1, pp. 1 – 8, 2019.

[99] J. I. Padilla-Buritica, J. M. Ferrandez-Vicente, G. A. Castaño, and C. D. Acosta-Medina, "Non-stationary group-level connectivity analysis for enhanced interpretability of oddball tasks," *Frontiers in Neuroscience*, 2020.

[100] K. Ø. Mikalsen, F. M. Bianchi, C. Soguero-Ruiz, and R. Jenssen, "Time series cluster kernel for learning similarities between multivariate time series with missing data," *Pattern Recognition*, vol. 76, pp. 569–581, 2018.

[101] M. K. I. Molla, A. Al Shiam, M. R. Islam, and T. Tanaka, "Discriminative feature selection-based motor imagery classification using eeg signal," *IEEE Access*, vol. 8, pp. 98 255–98 265, 2020.

[102] G. Pfurtscheller and F. L. Da Silva, "Event-related eeg/meg synchronization and desynchronization: basic principles," *Clinical neurophysiology*, vol. 110, no. 11, pp. 1842–1857, 1999.

[103] H.-T. Cheng, L. Koc, J. Harmsen, T. Shaked, T. Chandra, H. Aradhye, G. Anderson, G. Corrado, W. Chai, M. Ispir *et al.*, "Wide & deep learning for recommender systems," in *Proceedings of the 1st workshop on deep learning for recommender systems*, 2016, pp. 7–10.

[104] P. Nagabushanam, S. Thomas George, and S. Radha, "Eeg signal classification using lstm and improved neural network algorithms," *Soft Computing*, vol. 24, no. 13, pp. 9981–10 003, 2020.

[105] H. Cho, M. Ahn, S. Ahn, M. Kwon, and S. C. Jun, "Eeg datasets for motor imagery brain computer interface," *Gigascience*, 2017.

[106] B. Graimann, J. E. Huggins, S. P. Levine, and G. Pfurtscheller, "Visualization of significant ERD/ERS patterns in multichannel EEG and ECoG data," *Clinical neurophysiology*, vol. 113, no. 1, pp. 43–47, 2002.

[107] V. Carmen, S. T. H, and S. Alois, "BioSig: the free and open source software library for biomedical signal processing," *Computational intelligence and neuroscience*, vol. 2011, 2011.

[108] B. Z. Allison and C. Neuper, "Could anyone use a bci?" in *Brain-computer interfaces*, D. S. Tan and A. Nijholt, Eds. Springer, 2010, pp. 35–54.

[109] A. J. Brockmeier, "Learning and exploiting recurrent patterns in neural data," Ph.D. dissertation, Citeseer, 2014.

[110] H. Ghaheri and A. Ahmadyfard, "Extracting common spatial patterns from eeg time segments for classifying motor imagery classes in a brain computer interface (bci)," *scientiairanica*, vol. 20, no. 6, pp. 2061–2072, 2013.

[111] Z. Catharina, D. Stefan, K. Cornelia, B. Martin, G. Ingmar, and D. V. Maarten, "Real-time EEG feedback during simultaneous EEG–fMRI identifies the cortical signature of motor imagery," *Neuroimage*, vol. 114, pp. 438–447, 2015.

[112] I. Daly, S. J. Nasuto, and K. Warwick, "Brain computer interface control via functional connectivity dynamics," *Pattern recognition*, vol. 45, no. 6, pp. 2123–2136, 2012.

[113] E. W. Lang, A. M. Tomé, I. R. Keck, J. Górriz-Sáez, and C. G. Puntonet, "Brain connectivity analysis: a short survey," *Computational intelligence and neuroscience*, vol. 2012, p. 8, 2012.

[114] J. Padilla-Buritica, J. Hurtado, and G. Castellanos-Dominguez, "Supervised piecewise network connectivity analysis for enhanced confidence of auditory oddball tasks," *Biomedical Signal Processing and Control*, vol. 52, pp. 341–346, 2019.

[115] R. Oostenveld, P. Fries, E. Maris, and J.-M. Schoffelen, "Fieldtrip: open source software for advanced analysis of meg, eeg, and invasive electrophysiological data," *Computational intelligence and neuroscience*, vol. 2011, 2011.

[116] M. P. Van Den Heuvel and H. E. H. Pol, "Exploring the brain network: a review on resting-state fMRI functional connectivity," *European neuropsychopharmacology*, vol. 20, no. 8, pp. 519–534, 2010.

[117] T. Hanakawa, M. A. Dimyan, and M. Hallett, "Motor planning, imagery, and execution in the distributed motor network: a time-course study with functional MRI," *Cerebral cortex*, vol. 18, no. 12, pp. 2775–2788, 2008.

[118] K. Kasahara, C. S. DaSalla, M. Honda, and T. Hanakawa, "Neuroanatomical correlates of brain–computer interface performance," *Neuroimage*, vol. 110, pp. 95–100, 2015.

[119] R. Scherer and C. Vidaurre, "Motor imagery based brain–computer interfaces," in *Smart Wheelchairs and Brain-Computer Interfaces*, P. Diez, Ed. Elsevier, 2018, pp. 171–195.

[120] K. Y. Haaland, C. L. Elsinger, A. R. Mayer, S. Durgerian, and S. M. Rao, "Motor sequence complexity and performing hand produce differential patterns of hemispheric lateralization," *Journal of Cognitive Neuroscience*, vol. 16, no. 4, pp. 621–636, 2004.

[121] G. Pfurtscheller, C. Neuper, K. Pichler-Zalaudek, G. Edlinger, and F. H. L. da Silva, "Do brain oscillations of different frequencies indicate interaction between cortical areas in humans?" *Neuroscience letters*, vol. 286, no. 1, pp. 66–68, 2000.

[122] J. Lu, D. McFarland, and J. Wolpaw, "Adaptive laplacian filtering for sensorimotor rhythm-based brain–computer interfaces," *Journal of neural engineering*, vol. 10, no. 1, p. 016002, 2012.

[123] Y. Zhang, C. S. Nam, G. Zhou, J. Jin, X. Wang, and A. Cichocki, "Temporally constrained sparse group spatial patterns for motor imagery bci," *IEEE transactions on cybernetics*, vol. 49, no. 9, pp. 3322–3332, 2018.

[124] C.-F. V. Latchoumane, D. Chung, S. Kim, and J. Jeong, "Segmentation and characterization of eeg during mental tasks using dynamical nonstationarity," *Proc. Computational Intelligence in Medical and Healthcare (CIMED 2007), Plymouth, England*, 2007.

[125] M. Ma, L. Guo, K. Su, and D. Liang, "Classification of motor imagery eeg signals based on wavelet transform and sample entropy," in *2017 IEEE 2nd Advanced Information Technology, Electronic and Automation Control Conference (IAEAC)*, March 2017, pp. 905–910.

[126] M. Ahn, H. n. Cho, S. Ahn, and S. Jun, "High theta and low alpha powers may be indicative of bci-illiteracy in motor imagery," *PloS one*, vol. 8, no. 11, 2013.

[127] D. Collazos-Huertas, J. Caicedo-Acosta, G. A. Castaño-Duque, and C. D. Acosta-Medina, "Enhanced multiple instance representation using time-frequency atoms in motor imagery classification," *Frontiers in neuroscience*, vol. 14, p. 155, 2020.

[128] G. Pfurtscheller, "Eeg event-related desynchronization (erd) and synchronization (ers)," *Electroencephalography and Clinical Neurophysiology*, vol. 1, no. 103, p. 26, 1997.

[129] L. F. Velásquez-Martínez, F. Zapata-Castaño, J. I. Padilla-Buritica, J. M. F. Vicente, and G. Castellanos-Dominguez, "Group differences in time-frequency relevant patterns for user-independent BCI applications," in *International Work-Conference on the Interplay Between Natural and Artificial Computation*, 2019, pp. 138–145.

[130] E. Maris and R. Oostenveld, "Nonparametric statistical testing of eeg-and meg-data," *Journal of neuroscience methods*, vol. 164, no. 1, pp. 177–190, 2007.

[131] R. Giusti and G. E. Batista, "An empirical comparison of dissimilarity measures for time series classification," in *2013 Brazilian Conference on Intelligent Systems*. IEEE, 2013, pp. 82–88.

[132] I. Xygonakis, A. Athanasiou, N. Pandria, D. Kugiumtzis, and P. D. Bamidis, "Decoding motor imagery through common spatial pattern filters at the eeg source space," *Computational intelligence and neuroscience*, vol. 2018, 2018.

[133] M. Matsuo, N. Iso, K. Fujiwara, T. Moriuchi, G. Tanaka, S. Honda, D. Matsuda, and T. Higashi, "Cerebral haemodynamics during motor imagery of self-feeding with chopsticks: differences between dominant and non-dominant hand," *Somatosensory & Motor Research*, vol. 37, no. 1, pp. 6–13, 2020.

[134] Y. Tian, W. Xu, and L. Yang, "Cortical classification with rhythm entropy for error processing in cocktail party environment based on scalp eeg recording," *Scientific reports*, vol. 8, no. 1, pp. 1–13, 2018.

[135] B. Blankertz, R. Tomioka, S. Lemm, M. Kawanabe, and K.-R. Muller, "Optimizing spatial filters for robust eeg single-trial analysis," *IEEE Signal processing magazine*, vol. 25, no. 1, pp. 41–56, 2007.

[136] F. Kaffashi, R. Foglyano, C. G. Wilson, and K. A. Loparo, "The effect of time delay on approximate & sample entropy calculations," *Physica D: Nonlinear Phenomena*, vol. 237, no. 23, pp. 3069–3074, 2008.

[137] M. C. Thompson, "Critiquing the concept of bci illiteracy," *Science and engineering ethics*, vol. 25, no. 4, pp. 1217–1233, 2019.

[138] C. Neuper and G. Pfurtscheller, "Event-related dynamics of cortical rhythms: frequency-specific features and functional correlates," *International journal of psychophysiology*, vol. 43, no. 1, pp. 41–58, 2001.

[139] Y. Zhang, G. Zhou, J. Jin, X. Wang, and A. Cichocki, "Optimizing spatial patterns with sparse filter bands for motor-imagery based brain–computer interface," *Journal of neuroscience methods*, vol. 255, pp. 85–91, 2015.

[140] M. Miao, A. Wang, and F. Liu, "A spatial-frequency-temporal optimized feature sparse representation-based classification method for motor imagery eeg pattern recognition," *Medical & biological engineering & computing*, vol. 55, no. 9, pp. 1589–1603, 2017.

[141] J. Meng and B. He, "Exploring training effect in 42 human subjects using a non-invasive sensorimotor rhythm based online bci," *Frontiers in human neuroscience*, vol. 13, p. 128, 2019.

[142] X. Shu, S. Chen, L. Yao, X. Sheng, D. Zhang, N. Jiang, J. Jia, and X. Zhu, "Fast recognition of bci-inefficient users using physiological features from eeg signals: A screening study of stroke patients," *Frontiers in neuroscience*, vol. 12, p. 93, 2018.